Green Nanoprocessing of Polymer Surfaces with Supercritical Carbon Dioxide

浅田, 光則

https://doi.org/10.15017/1470648

Green Nanoprocessing of Polymer Surfaces with Supercritical Carbon Dioxide

超臨界二酸化炭素による高分子薄膜の表面／界面構造制御に関する研究

Mitsunori Asada

浅田　光則

2014

Contents

Chapter 1 General Introduction

1-1. Overall Goal and Research Objectives

1-1-1. Research Motivation

A one-component fluid at temperatures (T) and pressures (P) above the critical point value shows unique features such as liquid-like density and gas-like diffusion. Fluids in this regime are defined as supercritical fluids (SCFs); the unique features are originated from microscopic thermal fluctuations of molecules (i.e., density fluctuations), which are a counterbalance between an interaction of neighbor molecules and a mobility of molecules. Only small manipulations in T and P values enable one to access a wide range of the physical and thermodynamic properties of SCFs.

In particular, use of supercritical carbon dioxide ($scCO_2$) is advantageous for polymer processing from the viewpoint of facile designs of viscosity, solubility, diffusion and surface tension of $scCO_2$. In addition, the critical point of CO_2 is easily accessible (T_c = 31.3 ºC and P_c = 7.38 MPa) such that a large number of studies on industrial applications including polymer forming, separation, extraction and synthesis have been reported with the use of $scCO_2$ as environmentally friendly green solvent[1].

In general, the solvent quality of $scCO_2$ is poor at accessible conditions of T < 100 ºC and P < 50 MPa for a majority of polymers except for fluorinated polymers and silicone based polymers. However, Koga and co-workers revealed that the anomalous excess swelling of ultrathin polymer films (thickness (t) < 100 nm) takes place in CO_2 at the unique T and P conditions near room temperature along with the "density fluctuation ridge"[2-4] which is a locus of maxima of the density fluctuations at each isothermal condition near the critical point[5] (Fig. 1-1).

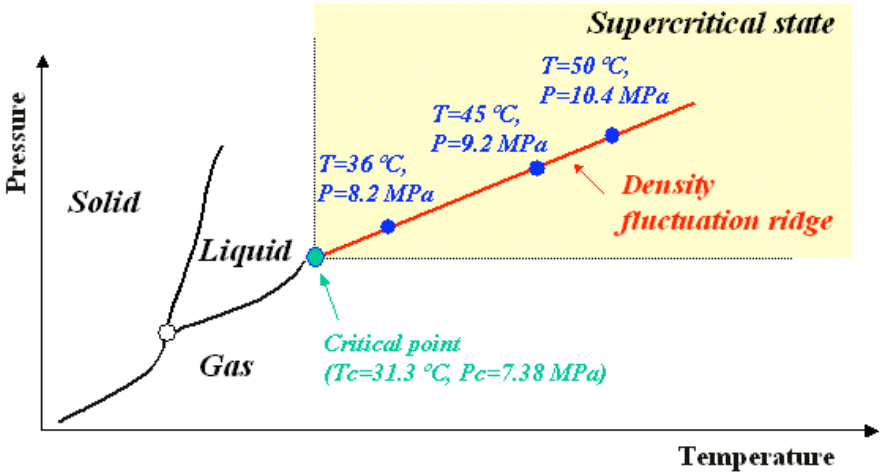

Fig. 1-1 Phase diagram of carbon dioxide. The red line corresponds to the density fluctuation ridge condition where the molecular scale density fluctuation becomes maxima.

The novel features of the anomalous excess swelling are summarized as follows:

i) Linear dilation (S_f) of polymer thin films, which occurs regardless of a choice of polymers, shows a strong dependence on the magnitude of the density fluctuations of $scCO_2$[6], as shown in Fig. 1-2.

ii) Elasticity of polymers influences the swelling ratio (S_f): the Sf value of the rubbery polymer thin films increases up to 0.6 at the ridge condition, while that of glassy polymer thin films is about 0.3 under the same CO_2 conditions[2, 3]. Note that the bulk swelling ratios at the ridge are about 0.1.

iii) The excess penetration of CO_2 molecules into polymers occurs within several tens of nanometers from the topmost polymer/$scCO_2$ interface, resulting in a concentration gradient of CO_2[2, 3, 6]. At the same time, the excess adsorption of CO_2 molecules at the polymer/substrate interface is reported[7, 8].

iv) Vitrification of glassy polymers via rapid pressure quench to atmospheric pressure allows one to preserve the swollen structures of polymer thin films in $scCO_2$[9, 10].

It is hence anticipated that "density fluctuating" $scCO_2$ can be effectively used for manipulations of the structures and properties at the polymer interfaces. Therefore, the overall goal of my thesis is to develop low-temperature $scCO_2$-based green processing for polymer surface/interfaces, i.e. the air/polymer interface and the polymer/solid substrate interface.

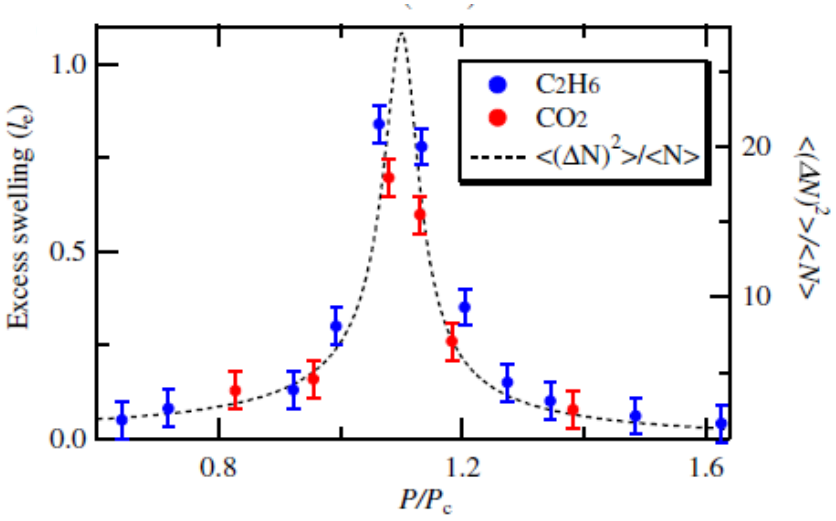

Fig. 1-2 Excess swelling (l_e) of deuterated-polybutadiene thin films in CO_2 and C_2H_6 obtained by *in-situ* neutron reflectivity measurements and the corresponding density fluctuations in both fluids[6]. The excess swelling was calculated by the following equation; $l_e = (L_1 - L_0)/L_0$, where L_1 and L_0 are the measured thickness of the swollen and unswollen polymer thin films, respectively. The density fluctuations were calculated by eq. 1.

1-1-2. Polymer Nanocomposite Thin Films

Polymer nanocomposite thin films are one of fascinating materials, because inclusion of nanoparticles into a polymer matrix opens a new possibility to emerge new functionalities, properties compared to the raw polymers. Depending on applications, a spatial distribution of nanoparticles in the direction normal to the film surface should be precisely controlled. Uniform dispersion of nanosized particles is a key for achieving improved properties throughout the polymer thin films. On the other hand, preferential segregation of nanoparticles has been used to inhibit dewetting of polymer thin films at the polymer/substrate interface[11-14] or to heal crack formation at the polymer/air interface. In a typical hybrid poly (3-hexyl thiophene)/fullerene derivative active layer for an organic solar cell, a topmost layer of a segregated fullerene derivative is crucial in device efficiency[15-17]. Achieving the precise control of these dispersions tailored to one's need is complicated, however, because of a delicate balance of polymer/nanoparticle interactions and constrains placed on configurations of long polymer molecules to accommodate nanoparticles in such a limited space[18-20].

Thus, the first objective of my thesis is to switch spatial distributions of polymer-dissolved nanoparticles by utilizing the unique phenomena of density fluctuating $scCO_2$: 1) excess a*b*sorption of CO_2 molecules into a polymer matrix, as mentioned above, and 2) excess a*d*sorption of CO_2 molecules on the nanoparticle surfaces[21-23] (i.e., critical wetting). I will show that the nanoparticles switch the spatial arrangements between preferential surface segregation at the polymer/air interface and homogenous dispersion within the entire film by "tuning" the CO_2 environmental conditions and film thickness. Interestingly, this $scCO_2$-induced switching occurs regardless of interactions between nanoparticles (with different ligands) and polymer matrices. In Chapter 2, based on comprehensive structure analyses using x-ray reflectivity (XR), neutron reflectivity (NR), atomic force microscope (AFM) and x-ray photoelectron spectroscopy (XPS), I will answer to the following questions:

i) What is the driving force of the surface migration of nanoparticles?
ii) Does the surface migration of nanoparticles occur regardless of a pair of polymers and nanoparticles?
iii) What is the threshold thickness for the effective modification of polymer thin films?

1-1-3. Mechanism of Melt Crystallization Perturbed by Two Interfaces (Surface Effect vs. Substrate Effect)

In the past two decades, fundamental studies on dynamics of amorphous polymer thin films have intensively been performed from an academic interest in a nanoconfinement effect[24-31]. In the earlier stage, the molecular weight dependence on surface T_g of glassy amorphous polymer thin films has been systematically investigated[32, 33]. It is widely accepted that surface T_g is largely decreased due

to an enhancement of a molecular mobility (the surface effect)[34-36]. The depression of T_g persists up to several tens of nanometer from the topmost surface of the films. On the other hand, it is reported that a molecular mobility near the polymer/substrate interface is largely retarded[37] (i.e., the substrate effect). The retarded dynamics associated with a substrate-bound polymer layer with increased T_g and viscosity[38-43] is experimentally evident. The substrate-bound polymer layer forms via a physical adsorption onto a substrate[44] and the retarded dynamics could be propagated into the film interior through chain entanglements[45]. The distance where the retarded dynamics recovers to that in the bulk is estimated to be several tens of nanometer[38] (the so-called "reduced mobility interfacial (RMI) layer"), which is the comparable length scale of the surface effect. Furthermore, it is reported that this irreversibly adsorbed polymer layer forms on a solid substrate regardless of an interaction between a polymer and a substrate[44, 46].

Intensive studies on hierarchical ordered structures of semi-crystalline polymers (i.e., single lamellar crystals stack towards the direction perpendicular to the chain-folded face and resultant repeated stacked lamellar domains propagate into three-dimensional spherocrystals) have been done. Since the space towards film normal is limited, growth of lamellar crystals with an anisotropic shape is influenced. Typically, two lamellar orientations emerge, depending on film thickness and crystallization temperature (T_c). The edge-on lamellar orientation, where the chain-folded face of crystals is perpendicular to the film surface, is frequently observed in films with relatively large thickness. On the other hand, when film thicknesses becomes thinner (typically less than 50 nm), flat-on lamellar crystal where the chain-folded face is parallel to film surface mostly appears. Furthermore, coexistence of both edge-on and flat-on lamellar orientations can also be seen, when T_c is sufficiently low (i.e., the degree of supercooling is large), as well as an isotropic random orientation. Thus the lamellar orientation obviously shows the strong thickness and T_c dependencies. However, the mechanism that explains the rule determining lamellar orientations has not been clarified yet.

Recently, there reported the crystallization model that takes the heterogeneous molecular mobility normal to the film surface into account. Wang et al. presented the three-T_g layer model to explain the lamellar orientation at the surface of polycarbonate thin films with the thickness and T_c dependencies[47]. Fig. 1-3 presents their model depicting a crystallization rate at each layer on the basis of the T_g confinement. In the surface region, the bell-shape profile of the crystallization rate shifts toward lower T due to the enhanced molecular mobility ($T_{g,1} < T_{g,bulk}$). On the contrary, the maximum T of the crystallization rate increases near the substrate due to the bound layer ($T_{g,3} > T_{g,bulk}$). Hence the crystallization takes place from each layer: at high T_c, the crystallization from the adsorbed layer near the substrate overcomes that from the mobile surface layer, while the surface mobile layer becomes dominant at low T_c. With increasing film thickness, nucleation from each interface competes, resulting in heterogeneity in the direction normal to the film surface. Considering the polymer/substrate interaction, the lamellar orientation can be then predicted. The nucleation of polymer chains contacting the substrate wall was predicted by molecular dynamics simulation[48]: it presented either the edge-on or the flat-on lamellar nuclei formed on a substrate wall,

depending on the interaction in order to minimize the excess free energy. A slipping wall (an interaction between the polymer and the substrate is weak) prefers the edge-on lamellar formation, while the flat-on lamellar is formed on the non-slipping wall (a strong interaction between a polymer and substrate). Consequently, the lamellar orientation near the substrate interface persists up to the film interior via the heterogeneous crystal growth, thus resulting in the coexistence with the edge-on lamellar formation at the topmost of the films.

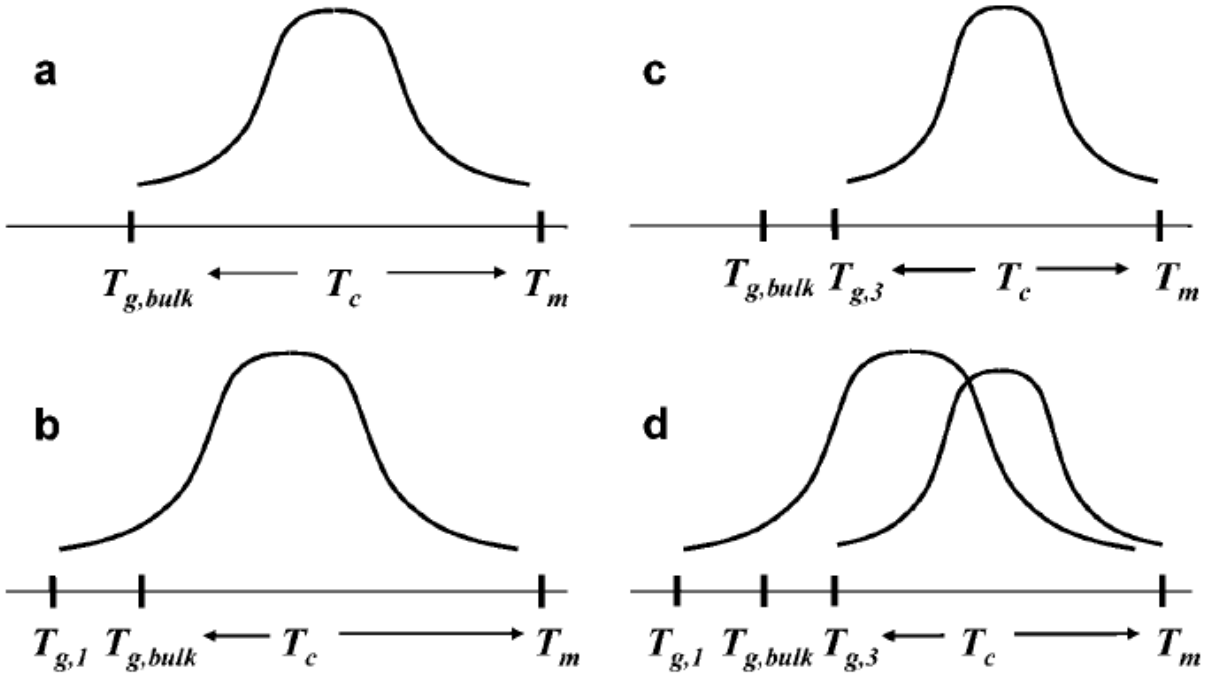

Fig. 1-3 Schematic model of a crystallization rate proposed by Wang et al.[47], based on heterogeneous T_g normal to film surface. (a) A bulk layer, (b) a topmost surface layer, (c) a bottom layer near a substrate and (d) a relation between a crystallization rate and a given crystallization temperature T_c. $T_{g,1}$ and $T_{g,3}$ denote grass transition temperature at surface and near a substrate, respectively.

Although most previous work has revealed the deviations of “average” quantities of entire nanometer films from the bulk, it is expected that the local quantities within the film would be different from the average ones, depending on the interplay between these interfaces. This unanswered question (and the second objective of my thesis) motivated the present study. In Chapter 3, the following points will be clarified:

i) What is the origin of the heterogeneous crystalline structures normal to film surface?
ii) Does the irreversible adsorbed polymer layer form on the slipping wall (an interaction between the polymer and the substrate is weak)?

In addition, the detailed mechanism considering both the CO_2 annealing and nanoconfinement effects on crystalline structures of polymer thin films has yet to be rationalized. In chapter 4, I therefore focus on the excess plasticization effects of CO_2 associated with the anomalous swelling on both the melting/crystallization behavior and the polymer adsorption of semi-crystalline polymer chains. Highlighting the CO_2 annealing effect on the formation of the substrate-bound adsorbed layer, the resultant heterogeneous semi-crystalline structures was compared to conventional thermal annealing (the third objective of my thesis).

1-2. Method of $ScCO_2$-based Polymer Modification

1-2-1. Introduction to Density Fluctuations of SCFs

As aforementioned, SCFs are composed of inhomogeneous regions with liquid-like and gas-like densities at the molecular level. Approaching to the critical point, this microscopic thermal fluctuations become more correlated, thus the long-range density fluctuations in SCFs eventually diverge. The long-range density fluctuations have been experimentally observed by partial molar volume measurements[49] and small angle x-ray scattering measurements[50]. Fig. 1-4 shows the contour plot of the calculated density fluctuations $< (\Delta N)^2> / <N>$ of CF_3H as a function of T and P using the following thermodynamic relation;

$$< (\Delta N)^2> / <N> = (N / V)\ \kappa_T k_B T, \quad (1)$$

where N is the number of molecules in the volume V, k_B is the Boltzman constant , and κ_T is the isothermal compressibility. The values of κ_T are calculated from the PVT data. From the figure we can see the maxima of the density fluctuations under each isothermal condition, and the locus of these maxima is known as “the density fluctuation ridge”. The two dimensional projection of the corresponding contour plot of CO_2 is already shown in Fig. 1-1. The ridge emanates from the critical point where the amplitude of the density fluctuations diverge and separates the more liquid-like and more gas-like regions in the supercritical region[5]. In the region below the critical point, the ridge corresponds to the vapor line. In the supercritical region, there is a memory of the vapor line; that is the ridge. This ridge is not only specific to CO_2. It is a general feature for substances, such as H_2O, CF_3H, Ar and Hg[50]. It is also known that the ridge corresponds to a maximum or minimum of thermal conductivity,[51] sound velocity,[49] and partial molar volumes[52]. In addition, the rate constants or equilibrium constants of various chemical reactions in SCFs show maxima, minima or inflection points at the ridge[53].

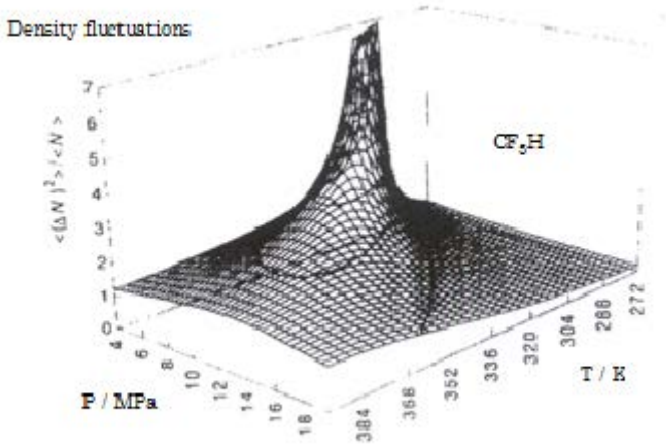

Fig. 1-4 Three-dimensional density fluctuation map for CF_3H[50].

1-2-2. Anomalous Excess Swelling of Polymer Thin Films in $ScCO_2$

Koga and co-workers have systematically studied the swelling behavior of polymer thin films in

scCO$_2$ and found that the anomalous excess swelling occurs regardless of a choice of polymers, although the elasticity of polymer chains influences the degree of the excess swelling. This excess swelling of polymer thin films can be scaled by the degree of the density fluctuation[6]. Fig. 1-5 (a) shows the S_f value of deuterated polystyrene-*b*-polybutadiene rubber thin films (40 nm in thickness) determined by the NR measurements[2]. In the figure the large maximal S_f values of 0.6 are observed in the dilation curves at T = 32 °C and 36 °C and the values of the maxima gradually decrease to approximately 0.3 with increasing up to 50 °C. As the pressure is increased well into the liquid or supercritical region, i.e., P > 15 MPa, the only a small dilation of approximately 0.1, which is the equivalent to the bulk swelling, was observed (red line). Fig. 1-5 (b) presents the theoretical calculations of the density fluctuations in pure CO$_2$. We can see that the magnitude of the excess swelling is strongly correlated to that of the density fluctuations in pure CO$_2$, and the anomalous maxima takes place along the density fluctuation ridge.

This result can be explained by the idea of a solvent clustering and solvation. It is attributed to the increase in the local solvent density around solvophilic polymer chains or the formation of a large correlation hole around solvophobic polymer chains. Within such solvation structures, polymer chains are expanded as a thermodynamically stable state such that additional large changes in solvent-density fluctuations around the polymer chains are induced, lowering the free energy of the entire SCF/polymer system[54, 55]. In this sense the phenomenon could be general for all SCFs.

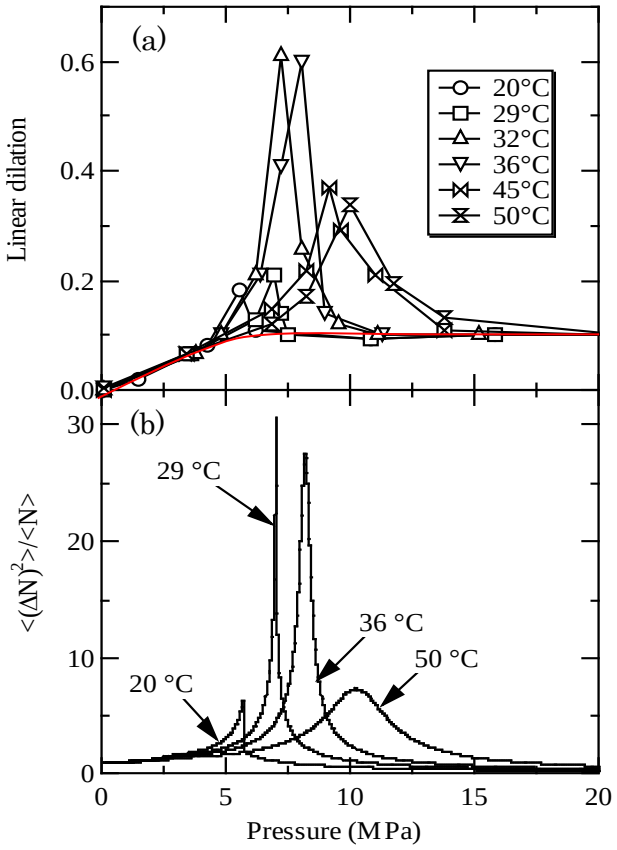

Fig. 1-5 (a) Linear dilation for the d-SBR thin films as a function of pressure at the six different temperatures. The red line corresponds to the swelling behavior of the bulk SBR film (2-μm thick). (b) Calculated density fluctuations of CO$_2$ based on the equation of state of CO$_2$[2].

1-2-3. Preserving the Swollen Structure of Polymer Thin Films

With an aid of vitrification of polymers via rapid quench to ambient pressure, the CO$_2$-swollen polymer chains can be frozen, resulting in the formation of low-density polymer thin films without any formation of macroscopic voids or phase separated structures[9, 10]. Based on the XR

measurements, Koga and co-workers revealed the density gradient within the film in the direction normal to the surface, as shown Fig. 1-6. It should be noted that the length scale of the penetration of CO_2 that induces the excess swelling is ca. 10 R_g from the CO_2/polymer interface, depending on a choice of polymers, although it is much more pronounced at the topmost of polymer films. The schematic illustration of the method for preserving the swollen structure in $scCO_2$[56] is shown in Fig. 1-7.

For glassy polymers such as polystyrene (PS) and poly (methyl methacrylate) (PMMA), the expanded films are stable below the bulk glass transition temperature (T_g), although the topmost surface presents the lowered T_g due to the introduced molecular scale porosity[9]. Thus, the combined features of $scCO_2$ near the critical point (i.e., the anomalous excess swelling and the subsequent vitrification process) are a candidate for creating new structures/properties of polymer thin films. As will be mentioned later, this method can be also utilized for semi-crystalline polymer thin films, allowing one to induce the melting of the crystalline structures in CO_2 even below the bulk melting temperature and preserve the swollen structures via rapid quench for subsequent melt crystallization study in air (the details is described in Chapter 4).

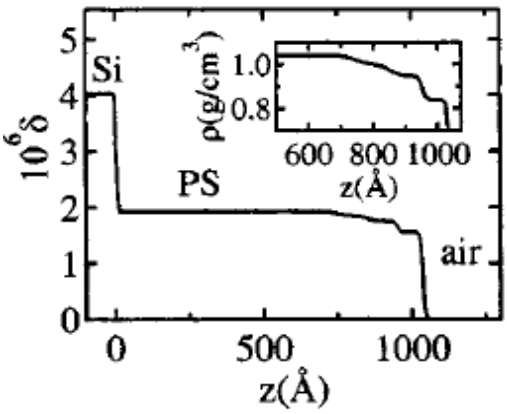

Fig. 1-6 Dispersion profile (δ) of the $scCO_2$ treated polystyrene (PS) thin film against the distance from the Si substrate obtained by the best-fit to the measured x-ray reflectivity curve. In the inset, the calculated density of PS is shown[9].

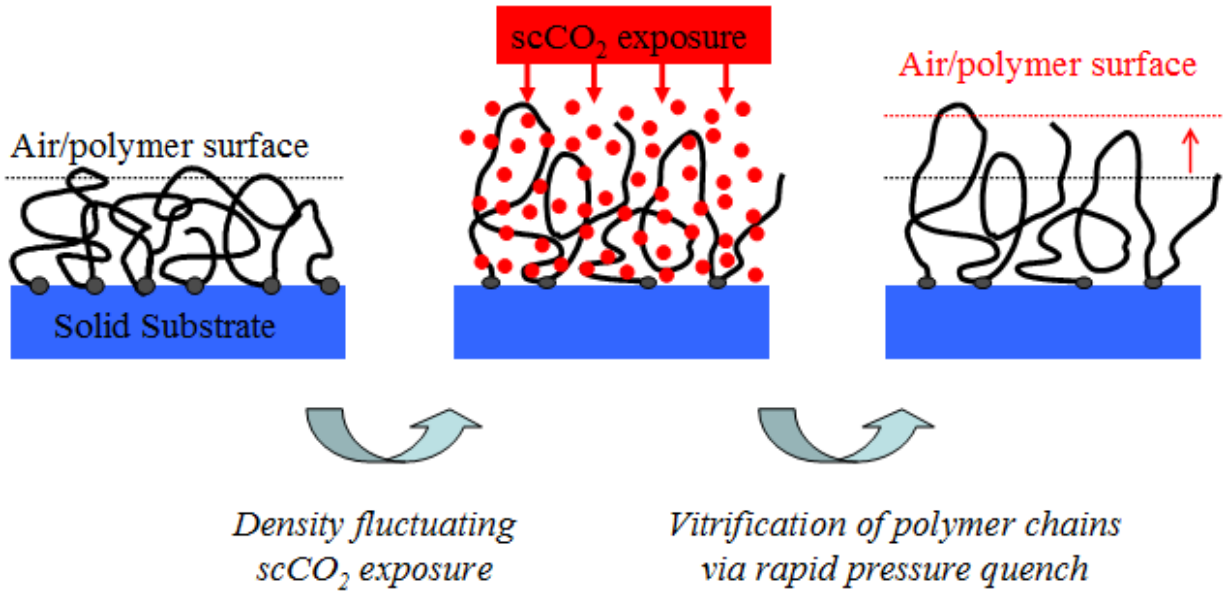

Fig. 1-7 Schematic view of preserving the swollen polymer structures in CO_2 by using rapid quench (within 10 sec) to atmospheric pressure[56].

1-3. Research Approaches

In my doctorial thesis, to develop a novel green nanoprocessing using the density fluctuating $scCO_2$ for modifying structures/properties of polymers at surfaces/interfaces, the following three objectives are addressed:

1. Development of low-temperature, environmentally benign route for making versatile polymer surfaces.
2. Better understanding of the interplay between the free surface and substrate interface that create heterogeneous crystalline structures within single polymer thin films.
3. Investigation of the mechanism of the $scCO_2$-assisted melt crystallization and the role of the substrate-bound adsorbed polymer layer.

Below is the brief summary of how I approached these objectives and what I have found.

1) Development of low-temperature, environmentally benign route for making versatile polymer surfaces (Chapter 2)

In Chapter 2, the density fluctuating $scCO_2$ annealing process was applied to polymer nanocomposite thin films. As mentioned above, the excess swelling takes place at the topmost of the films when polymer nanocomposite thin films are exposed to $scCO_2$ in the highly compressible region near the critical point. At the same time, excess adsorption of CO_2 molecules on nanoparticle surfaces also is induced[21, 22, 57]. Findenegg has firstly reported the excess surface adsorption of ethylene and sulfur hexafluoride molecules on graphite carbon black particles[57]. The similar excess adsorption of CO_2 molecules on various particles including silica and octadecyl-bonded silica have been also reported[21-23]. Furthermore, Lal et al. showed that the excess adsorption also takes place in particles with ligand molecules attached, while the degree of the adsorption depends on the interactions between solvent and ligand molecules[58, 59]. Koga and co-workers found that the excess absorption expands polymer chains homogeneously or heterogeneously, depending on the balance between the penetration length of the fluid molecules into a polymer and the film thickness[2, 3].When the film thickness is larger than the penetration length scale of the fluid molecules, a concentration gradient of the fluid is developed at the topmost surface region within the film. I hypothesize that this concentration gradient provokes instability of the dispersion of the CO_2-wetted nanoparticles and thereby migration of the nanoparticles preferentially to the topmost CO_2-rich region through the concentration gradient[60] (the concept is shown in Fig. 1-8), in order to minimize the entropic penalty of constrained polymer chains by the nanoparticles. By contrast, when the homogenous excess absorption of the fluid molecules into polymer occurs, the resultant anomalous expansion of the polymer chains may reduce the entropic penalty of the chains without expelling the nanoparticles to the free surface, allowing the accommodation of the "CO_2-wetted" nanoparticles within the films. The nanoparticles migrated to the surface would be then coagulated together due to

the attractive interaction among them, resulting in the large nano-aggregate structures at the polymer surface.

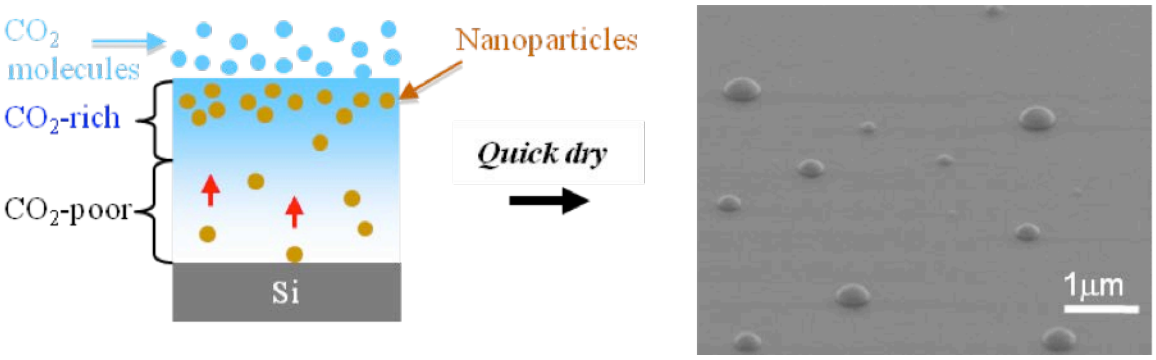

Fig. 1-8 Proposed mechanism of the scCO$_2$-induced surface segregation of nanoparticles[60]. In a polymer matrix, a concentration gradient of fluid molecules is formed due to limited penetration power of fluids in a viscous polymer matrix. Nanoparticles with critical wetting of CO_2 molecules near the ridge condition move to the CO_2-rich phase by taking advantage of a steep concentration gradient of the CO_2 near the surface. The right SEM image corresponds to the treated PS/PCBM nanocomposite thin film at the density fluctuation ridge condition.

To validate my assumption, a variety of nanoparticles including clay, fullerene derivative and polyhedral oligomeric silsesquioxane derivative (POSS) nanoparticles were embedded in PS and PMMA (the weight concentrations of the nanoparticles were less than 5 %). The films with various thicknesses (from 20 to 100 nm) were subject to the CO_2 annealing at both the density fluctuating ridge and the off-ridge to emphasize the effect of the density fluctuations on the phenomenon. I characterized the film structures *in-situ* and *ex-situ* by combining NR, XR, XPS and AFM measurements. Fig. 1-9 shows the schematic view of the high pressure chamber designed for the scCO$_2$ annealing experiments[3] used in my study. In Chapter 2, I will present the switch of the dispersion state of the nanoparticles: the surface migrated and/or the nano-aggregated structures of the nanoparticles which are induced by the density fluctuating scCO$_2$ annealing.

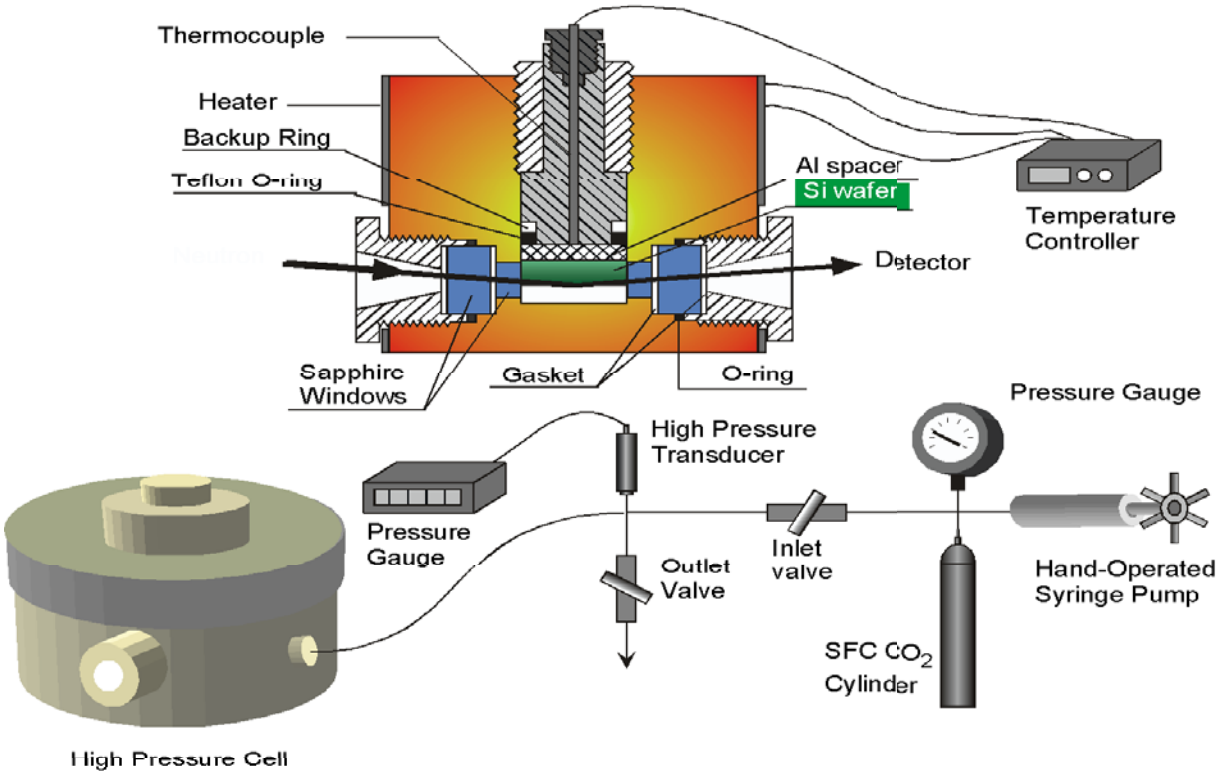

Fig. 1-9 Schematic view of the high pressure chamber designed for the scCO_2 annealing experiments used for the study. The *in-situ* neutron reflectivity measurements were also performed with the chamber[3].

2) Better understanding of the interplay between the free surface and substrate interface to create heterogeneous crystalline structures within polymer thin films (Chapter 3).

In Chapter 3, linear low-density polyethylene (LLDPE, bulk melting temperature (T_m) = 117 °C) films were prepared on Si substrates (25, 50 and 100 nm in thickness) as the model system. The *in-situ* x-ray scattering techniques were utilized for directly observing the melting behavior of the LLDPE thin films with elevating temperature, since the two setup modes (the x-ray incident angle (α_i) is above/below the critical angle (α_c)) allow one to separate the structures at the surface from ones in the film interior. The *in-situ* grazing incidence small angle x-ray scattering (GISAXS) and x-ray diffraction (GID) results revealed the surface order (including the crystallinity, the lamellar stacking and the long periods) are significantly reduced even at $T << T_m$ when the thickness of the LLDPE films is reduced to 25 nm. In addition to this surface disordering, I found that the 25 nm thick film has the heterogeneous interior architectures in the direction normal to the surface: At the polymer/substrate interface, the persistence of a "substrate-bound" edge-on lamellar layer (~ 10 nm in thickness) even at $T >> T_m$; In between the two interfacial layers, the existence of the well ordered edge-on lamellae with the long periods. This intermediate interior region corresponds to the

RMI layer in which the polymer chains are entangled with the bound layer and act as a "transition zone" ensuring continuity in the mobility profile from the substrate to the bulk[61, 62]. To explain the heterogeneous structures with the different local chain mobility, I propose that the crystallization in the transition zone is initiated from the substrate-bound lamellar surface as "seeds", independent of the primary nucleation and growth at the air/polymer interface due to the enhanced chain mobility. Hence, the concurrent crystallization at the air/polymer interface and from the surface of the substrate-bound lamellar layer results in the internal heterogeneous structures. Since the interaction between LLDPE and Si is categorized as a weakly attractive interacting system, the combined effect of the "substrate-bound" lamellar layer and the transition zone would likely be general and hence crucial for manipulating the structures and properties of ultrathin semi-crystalline polymer films.

In the study I also attempted to observe the structure of the substrate-bound lamellar surface, which was prepared by the method shown in Fig. 1-10, as well as the systematic GISAXS/GID measurements with rising temperature for the spin-cast films.

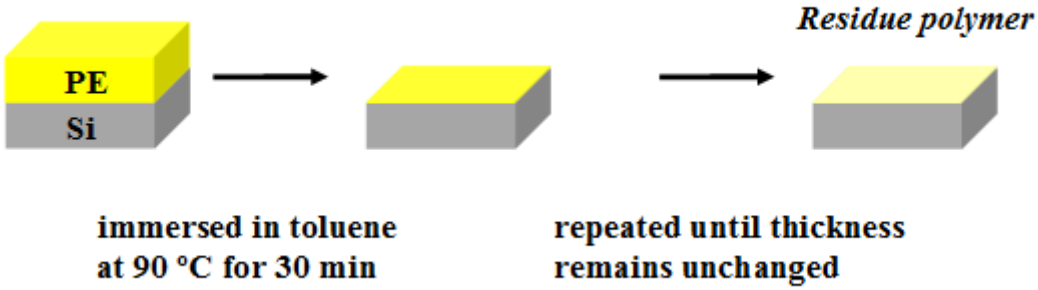

Fig. 1-10 Schematic view of the solvent leaching method used for the study. A polymer thin film was immersed in a good solvent. The cycle is repeated until the thickness of polymer layer remains unchanged.

3) Investigation of the mechanism of the scCO$_2$-assisted melt crystallization and the role of the substrate-bound adsorbed polymer layer (Chapter 4).

In Chapter 4, the scCO$_2$ annelaing was applied to semi-crystalline polymer thin films. In the study poly (ethylene oxide) (PEO) thin films were used as a model, since the melting/crystallization behavior in CO$_2$ has been well characterized in bulk[63, 64] as well as thin film[65]. The key is to illuminate the effect of CO$_2$ annealing on polymer adsorption process and the consequent substrate effect on melt crystallization. Thermal annealing is the most common fabrication process for polymeric materials to relieve the internal stresses introduced during sample preparation and to achieve the semi-equilibrium morphologies and properties. However, thermal annealing is considered to be less effective, especially for polymer melts, because of its prolonging time

requirement. In addition, thermal annealing may not be useful for many advanced polymeric materials used for e.g., electric or biological applications that cannot withstand high-temperature processing.

In this chapter, I therefore focus on CO_2 annealing for semi-crystalline polymer thin films in place of thermal annealing. It is known that sorption of CO_2 molecules into a polymer plays a role as a diluent or plasticizer for many glassy/semi-crystalline polymers, lowering the glass transition temperature and melting temperature significantly and hence enhancing the chain mobility. In addition, my experimental results by using various surface/interface sensitive experimental techniques including XR, GID, polarized optical microscopy (POM), and AFM suggested that the CO_2 annealing induces the formation of an irreversibly adsorbed layer onto the Si substrate. Furthermore, I elucidated the structure of the very thin adsorbed layer (several nm in thickness) and illuminated the effect on the melt crystallization/dewetting processes during CO_2 annealing. Since there is now growing evidence that the presence of the irreversibly adsorbed layer results in long-range structure and property heterogeneities within film interior, a better understanding of the polymer/substrate interface during solvent annealing processes including CO_2 would be the key for the development of new polymer nanostructures and nanoscale devices[49].

1-4. References

1. McHugh, M. A.; Krukonis, V. J., *Supercritical Fluid Extraction: Principles and Practice.* Butterworth-Heinemann: Boston, 1994.
2. Koga, T.; Seo, Y.-S.; Zhang, Y.; Shin, K.; Kusano, K.; Nishikawa, K.; Rafailovich, M. H.; Sokolov, J. C.; Chu, B.; Peiffer, D.; Occhiogrosso, R.; Satija, S. K. *Phys. Rev. Lett.* **2002,** 89, 125506
3. Koga, T.; Seo, Y.-S.; Shin, K.; Zhang, Y.; Rafailovich, M. H.; Sokolov, J. C.; Chu, B.; Satija, S. K. *Macromolecules* **2003,** 36, (14), 5236–5243.
4. Koga, T.; Y. Ji, Y. S. S.; Gordon, C.; Qu, F.; Rafailovich, M. H.; Sokolov, J. C.; Satija, S. K. *J. Polym. Sci. Part B. Polym. Phys.* **2004,** 42, (17), 3282-3289.
5. Nishikawa, K.; Tanaka, I.; Amemiya, Y. *J. Phys. Chem.* **1996,** 100, 418-421.
6. Koga, T.; Gin, P.; Yamaguchi, H.; Endoh, M. K.; Asada, M.; Sendogdular, L.; Kobayashi, M.; Takahara, A.; Akgun, B.; Satija, S. K.; Sumi, T. *Polymer* **2011,** 52, 4331-4336.
7. Li, X.; Vogt, B. *J. Supercrit. Fluids* **2009,** 51, 256.
8. Li, X.; Vogt, B. *Polymer* **2009,** 50, 4182.
9. Koga, T.; Seo, Y. S.; Jerome, J.; Ge, S.; Rafailovich, M. H.; Sokolov, J. C.; Chu, B.; Seeck, O. H.; Tolan, M.; Kolb, R. *Appl. Phys. Lett.* **2003,** 83, 4309.
10. Gin, P.; Asada, M.; Endoh, M. K.; Gelelian, C.; Lu, T.-M.; Koga, T. *Appl. Phys. Lett.* **2009,** 94, 121908.
11. Barnes, K. A.; Karim, A.; Douglas, J. F.; Nakatani, A. I.; Gruell, H.; Amis, E. J. *Macromolecules* **2000,** 33, (11), 4177–4185.
12. Mackay, M. E.; Hong, Y.; Jeong, M.; Hong, S.; Russell, T. P.; Hawker, C. J.; Vestberg, R.; Douglas, J. F. *Langmuir* **2002,** 18, 1877–1882.
13. Krishnan, R. S.; Mackay, M. E.; Hawker, C. J.; Horn, B. V. *Langmuir* **2005,** 21, 5770–5776.
14. Krishnan, R. S.; Mackay, M. E.; Duxbury, P. M.; Pastor, A.; Hawker, C. J.; Horn, B. V.; Asokan, S.; Wong, M. S. *Nano Lett.* **2007,** 7, (2), 484-489.
15. Parnell, A. J.; Dunbar, A. D. F.; Pearon, A. J.; Staniec, P. A.; Dennison, A. J.; Hamamatsu, H.; Lidzey, M. W. A. S. G.; Jones, R. A. L. *Adv. Mater.* **2010,** 22, 2444-2447.
16. Chen, D.; Nakahara, A.; Wei, D.; Nordlund, D.; Russell, T. P. *Nano Lett.* **2011,** 11, 561-567.
17. Treat, N. D.; Brady, M. A.; Smith, G.; Toney, M. F.; Kramer, E. J.; Hawker, C. J.; Chabinyc, M. L. *Adv. Energy Mater.* **2011,** 1, 82-89.
18. Balazs, A. C.; Emrick, T.; Russell, T. P. *Science* **2006,** 314, 1107-1110.
19. Balazs, A. C. *Nat. Mater.* **2007,** 6, 94-95.
20. Stamm, M.; Sommer, J.-U. *Nat. Mater.* **2007,** 6, 260-261.
21. Blümel, S.; Findenegg, G. H. *Phys. Rev. Lett.* **1985,** 54, 447-450.
22. Strubinger, J. R.; Parcher, J. F. *Anal. Chem.* **1989,** 61, 951-955.
23. Strubinger, J. R.; Parcher, H. S. F. *Anal. Chem.* **1991,** 63, 98-103.
24. Hu, H. W.; Granick, S. *Science* **1992,** 258, 1339.

25. Zheng, X.; Rafailovich, M. H.; Sokolov, J.; Strzhemechny, Y.; Schwarz, S. A.; Sauer, B.; Rubinstein, M. *Phys. Rev. Lett.* **1997,** 79, 241.
26. Ellison, C. J.; Torkelson, J. M. *Nature Materials* **2003,** 2, 695-700
27. Fakhraai, Z.; Forrest, J. A. *Phys. Rev. Lett.* **2005,** 95, 025701.
28. Priestley, R. D.; Ellison, C.; Broadbelt, L. J.; Torkelson, J. M. *Science* **2005,** 309, 456.
29. Bodiguel, H.; Fretigny, C. *Phys. Rev. Lett.* **2006,** 97, 266105.
30. Li, C.; Kim, H.; Jiang, J.; Li, C.; Koga, T.; Lurio, L. B.; Schwarz, S.; Narayanan, S.; Lee, H.; Lee, Y.-J.; Jiang, J.; Sinha, S. K.; Rafailovich, M. H.; Sokolov, J. C. *Europhys. Lett.* **2006,** 73, 899.
31. Koga, T.; Jiang, N.; Gin, P.; Endoh, M. K.; Narayanan, S.; Lurio, L. B.; Sinha, S. K. *Phys. Rev. Lett.* **2011,** 107, 225901.
32. Tanaka, K.; Taura, A.; Ge, S. R.; Takahara, A.; Kajiyama, T. *Macromolecules* **1996,** 29, 3040-3042.
33. Satomi, N.; Takahara, A.; Kajiyama, T. *Macromolecules* **1999,** 32, 4474-4476.
34. Fakhraai, Z.; Forrest, J. A. *Science* **2008,** 319, 600.
35. Koga, T.; Li, C.; Endoh, M. K.; Koo, J.; Rafailovich, M. H.; Narayanan, S.; Lee, D. R.; Lurio, L. B.; Sinha, S. K. *Phys. Rev. Lett.* **2010,** 104, 066101.
36. Yang, Z.; Fujii, Y.; Lee, F. K.; Lam, C.-H.; Tsui, O. *Science* **2010,** 328, 1676.
37. Alsten, J. G. V.; Sauer, B. B.; Walsh, D. J. *Macromolecules* **1992,** 25, 4046-4048.
38. Napolitano, S.; Prevosto, D.; Lucchesi, M.; Pingue, P.; D'Acunto, M.; Rolla, P. *Langmuir* **2007,** 23, 2103-2109.
39. Napolitano, S.; Wübbenhorst, M. *J. Phys. Chem. B* **2007,** 111, 9197-9199.
40. Fujii, Y.; Yang, Z.; Leach, J.; Atarashi, H.; Tanaka, K.; Tsui, O. K. C. *Macromolecules* **2009,** 42, 7418-7422.
41. Napolitano, S.; Pilleri, A.; Rolla, P.; Wübbenhorst, M. *ACS Nano* **2010,** 4, (2), 841-848.
42. Lan, Q.; Yu, J.; Zhang, J.; He, J. *Macromolecules* **2011,** 44, 5743-5749.
43. Napolitano, S.; Wübbenhorst, M. *Nature Communications* **2011,** 2, 260.
44. Jiang, N.; Shang, J.; Di, X.; Endoh, M. K.; Koga, T. *Macromolecules* **2014,** 47, 2682-2689.
45. Wu, W. L.; Wallace, W. E.; Zanten, J. H. v.; Bauer, B. J.; Liu, D. W.; Wong, A. *Polymer* **1997,** 38, 2583.
46. Asada, M.; Jiang, N.; Sendogdular, L.; Sokolov, J.; Endoh, M. K.; Koga, T.; Fukuto, M.; Yang, L.; Akgun, B.; Dimitriou, M.; Satija, S. K. *Soft Matter* **2014,** accepter manuscript.
47. Wang, Y.; Chan, C.-M.; Ng, K.-M.; Li, L. *Macromolecules* **2008,** 41, 2548-2553.
48. Ma, Y.; Hu, W.; Reiter, G. *Macromolecules* **2006,** 39, 5159-5164.
49. EF, E. F. C.; Cykowski, C. B.; JF, J. F. h.; Swyt, D. A. *Physica* **1968,** 38, 307.
50. Nishikawa, K.; 2000, T. M. *Chem. Phys. Lett.* **2000,** 316, 238.
51. Chen, Z.; Tozaki, K.; Nishikawa, K. *Jpn. J. Appl. Phys.* **1999,** 38, 6840.
52. Eckert, C. A.; Ziger, D. H.; Johnston, K. P.; Kim, S. *J. Phys. Chem.* **1986,** 90, 2738.
53. Eckert, C. A.; Kuntson, B. L.; Debenedetti, P. G. *Nature Communications* **1996,** 383, 313.

54. Sumi, T.; Sekino, H. *J. Chem. Phys.* **2005,** 122, 194910-194911.
55. T, T. S.; N, N. I.; Sekino, H. *Phys. Rev. E* **2009,** 79, 030801.
56. Koga, T.; Jerome, J.; Rafailovich, M. H.; Chu, B.; Douglas, J.; Satija, S. *Adv. Coll. Int. Sci.* **2006,** 128-130, 217-226.
57. Findenegg, G. H., *In Fundamentals of Adsorption*. Engineering Foundation: 1983.
58. Lal, M.; Plummer, M.; Richmond, N. J.; Smith, W. *J. Phys. Chem. B* **2004,** 108, 6052-6061.
59. Lal, M.; Plummer, M.; Smith, W. *J. Phys. Chem. B* **2006,** 110, 20879-20888.
60. Asada, M.; Gin, P.; Endoh, M. K.; Satija, S. K.; Taniguchi, T.; Koga, T. *Soft Matter* **2011,** 7, 9231-9238.
61. Wallace, W. E.; Zanten, J. H. v.; Wu, W. L. *Phys. Rev. E* **1995,** 52, R3329.
62. Zanten, J. H. v.; Wallace, W. E.; Wu, W. L. *Phys. Rev. E* **1996,** 53, R2053.
63. Weidner, E.; Wiesmet, V. *J. Supercritical Fluids* **1997,** 10, 139-147.
64. Madsen, L. A. *Macromolecules* **2006,** 39, 1483-1487.
65. Li, Y.; Park, E.; Lim, K.; Johnston, K. P.; Green, P. F. *J. Polym. Sci. Part B:Polym. Phys.* **2007,** 45, 1313-1324.

Chapter 2 Development of Low-temperature, Environmentally Benign Route for Making Versatile Polymer Surfaces

2-1. Abstract

In Chapter 2, the density fluctuating $scCO_2$ annealing was applied to polymer nanocomposite thin films. The excess swelling anomalously takes place at the topmost of the films when polymer nanocomposite thin films are exposed to $scCO_2$ in the highly compressible region near the critical point. At the same time, excess adsorption of CO_2 molecules on nanoparticle surfaces also is induced. I report a versatile route for self-assembly of polymer-soluble nanoparticles at the polymer surface. Polystyrene and poly (methyl methacrylate)-based nanocomposite thin films with functionalized polyhedral oligomeric silsesquioxane, phenyl C_{61} butyric acid methyl ester and organoclay nanoparticles were prepared on Si substrates and exposed to $scCO_2$ at different pressures under the isothermal condition of 36 ºC. The resultant structures could be then preserved by the vitrification process of the glassy polymers via quick pressure quench to atmospheric pressure and subsequently characterized by using various surface sensitive experimental techniques in air. It was found that the surface segregation and self-aggregation of these nanoparticles are induced in the close vicinity of P = 8.2 MPa where the excess absorption of the fluid into the polymers maximizes. I addressed the nanoparticle migration to the emergence of a concentration gradient of the fluid at the polymer/CO_2 interface, since the uniform dispersion of the nanoparticles is favorable instead even at the same CO_2 conditions when the film thickness is less than about $4R_g$ thick (where R_g is the radius of polymer gyration). This phase transition is a general phenomenon for different polymer-nanoparticle interactions and utilized for low-temperature, environmentally benign route for making versatile polymer surfaces.

2-2. Introduction

Control of nanoparticle dispersion in a single polymer component is valuable in both scientific and technological aspects. On the one hand, uniform dispersion of inorganic nanoparticles with such larger interfacial areas is crucial for improving mechanical,[1, 2] magnetic,[3] optoelectronic[4, 5] and tribological[6] properties. On the other hand, preferential segregation of nanoparticles to a polymer/substrate interface can be used to inhibit dewetting of polymer thin films upon thermal annealing[7-10]. These assembling processes of nanoparticles are, however, complicated even in a single polymer component due to a delicate balance of both enthalpic and entropic contributions involved[11-13] and requirements of synthetic surface modifications of nanoparticles[14-16].

Here, with the aim of developing an alternative simple strategy to control spatial distributions of nanoparticles embedded in polymers at the nanometre scale, I use supercritical carbon dioxide ($scCO_2$, the critical point is T_c = 31.3 ºC and P_c = 7.38 MPa). The motivation lies in the fact that $scCO_2$ is an effective plasticization agent for many polymers[17] and forms a wetting layer on particle surfaces near the critical point,[18-20] possibly leading to a role as a ‘‘co-solvent’’ for a polymer matrix and nanoparticles embedded. In contrast to this enthalpic contribution, Gupta et al.[21] showed when constraints placed on configurations of polymer chains to accommodate nanoparticles become significant, nanoparticles even compatible with polymers are migrated to the polymer/air surface, the so-called ‘‘entropy-driven’’ segregation[22-24]. This entropic constrain would be more important in ultrathin polymer films/$scCO_2$ systems since polymer chains are anomalously expanded due to excess absorption of CO_2 molecules near the critical point[25].

It is known that supercritical fluids are composed of inhomogeneous regions with high and low densities at the microscopic scale[26]. Near the critical point the microscopic thermal fluctuations, which occur naturally in any fluids, become strongly correlated, leading to large-scale, coherent density fluctuations[27]. The density fluctuations in a supercritical region show a maximum under isothermal/isobaric conditions and the locus of the maxima is the so-called ‘‘density fluctuation ridge’’[28]. Previous results have demonstrated that the large density fluctuations near the ridge induce the anomalous maximum in the swelling of a variety of spin cast polymer thin films (up to about 600 nm thick) including ‘‘CO_2-phobic’’ polymers,[25, 29-32] ‘‘CO2-philic’’ fluorinated polymers,[32, 33] glassy polymers,[25, 29-32] semi-crystalline polymers,[32] and block copolymer films[32, 34, 35]. It should be noted that the anomalous swelling is a surface effect which occurs only within $10R_g$ (R_g is the radius of polymer gyration) thickness of the polymer/CO_2 interface[25]. Recently, Li and Vogt reported that the excess swelling at not only the polymer/CO_2 interface but also the polymer/substrate interface contributes to the anomalous swelling maximum[34, 35]. Theoretical calculations based on the Sanchez–Lacombe equation of state showed that an adsorption layer (3 nm in thickness) of CO_2 molecules on the film surface is responsible for the excess swelling[36]. However, *in situ* neutron reflectivity studies on the swelling behaviour of polystyrene brushes (with approximately $2R_g$ thickness) indicated that the excess swelling is mainly attributed to excess expansion of the individual polymer chains themselves[31] rather than the critical wetting layer. In fact, this is consistent with numerical calculations on the solvation structures of a single polymer

chain in a supercritical fluid (SCF) near the critical point[37, 38]. Sumi et al. predicted that the local solvent density around the polymer is enhanced/reduced depending on the polymer-fluid interactions and the polymer chain in such solvation structures is expanded regardless of the interactions as a thermodynamically stable state. They also explained that this anomalous expansion causes additional large solvent-density fluctuations around the polymer chain, thereby lowering the free energy of the entire SCF/polymer system. Koga and co-workers have shown that this mechanism also is valid for the anomalous swelling of concentrated polymer chains on solid substrates in SCFs[33].

In Chapter 2, I show that highly compressible $scCO_2$ in the proximity of the density fluctuation ridge induces migration of polymer-soluble nanoparticles to the polymer-CO_2 interface. Hereafter I define the aggregates of the nanoparticles at the surface as ‘‘nano-aggregates’’ to distinguish from individual nanoparticles. This $scCO_2$-induced surface segregation of the nanoparticles is rather general for different polymers and nanoparticles with different ligands. Interestingly, there is a critical thickness (about $4R_g$ thick) for the phase behavior below which the uniform dispersion of the nanoparticles is favorable instead. It was found that a concentration gradient of the fluid molecules at the polymer/CO_2 interface is strongly correlated with the phase transition. It is proposed that the nanoparticles coated with a critical wetting layer of CO_2 molecules at the ridge[18-20] are preferentially migrated to the CO_2-rich region through the concentration gradient as the driving force, as predicted in a previous simulation study on the dynamics of particles embedded in a binary mixture in the course of phase separation[39]. Finally, I also discuss that a delicate counterbalance among three relevant surface tensions (polymer/CO_2, polymer/nano-aggregates, and nano-aggregates/CO_2) plays a crucial role in controlling the shapes and thermodynamic stability of the surface segregated structures in $scCO_2$.

2-3. Experimental Section

2-3-1. Materials

The polymers used in this study were polystyrene (PS, Pressure Chemical Co.) and poly(methyl methacrylate) (PMMA, Polymer Source, Inc.) since the *in situ* and *ex situ* swelling behavior of pure PS and PMMA thin films in $scCO_2$ have been well characterized[25, 29-32, 40, 41]. The weight-average molecular weight (M_w) and polydispersity index (M_w / M_n) were 200,000 and 1.06 for PS and 70,000 and 1.07 for PMMA, respectively. The bulk glass transition temperatures (T_g) of both polymers are 100-110 ºC.

The nanoparticles used in the research were as follows. Two kinds of polymer-based polyhedral oligomeric silsesquioxane (POSS) derivatives were purchased from Hybrid Plastics Inc. 3-(3,5,7,9,11,13,15-Heptaisobutylpentacyclo[9.5.13,9.15,15.17,13] octasiloxan-1-yl) propyl methacrylate ($C_{35}H_{74}O_{14}Si_8$) was randomly copolymerized with (i) styrene monomers (POSS–PS, weight fraction of the POSS component was 15%) and (ii) methyl methacrylate monomers (POSS–PMMA, the weight fraction of the POSS component was 25%), respectively. The POSS cage was directly attached to the methyl methacrylate unit via a propylene chain. The number fraction of the POSS unit for the POSS–PS and the POSS–PMMA was 2.3% and 4.2%, respectively. Phenyl C_{61} butyric acid methyl ester (PCBM) was purchased from Sigma-Aldrich Co. The average sizes of the pure POSS cage and fullerene cage moiety were about 1.5 and 1.0 nm, respectively. The natural organoclay particle modified with a surfactant (Cloissite 6A, Southern clay) was also used (μm-sized in lateral direction). All the materials were used without further purification.

2-3-2. Thin Film Preparation

The POSS, PCBM and organoclay nanoparticles were first dissolved in toluene. The concentration of the POSS nanoparticles and the PCBM nanoparticles against the polymers was fixed to be 10 % by weight. The concentration of the organoclay nanoparticle was 1 % by weight. After all the solutions were sonicated for 1 min, PS or PMMA was then added to the solutions. The solutions were heated to 70 ºC for 30 min and further sonicated for 1 min to ensure the good dispersion of the nanoparticles. Polymer nanocomposite thin films were prepared by spin-coating onto HF etched Si substrates and then annealed for 24 h in vacuum of 10^{-3} Torr at T = 160 ºC >> T_g of PS or PMMA in order to remove residual solvents and to relax strains induced in the spinning-process. The thickness of all nanocomposite thin films was fixed to about 120 nm, unless otherwise stated. The nanocomposite thin films were then placed into a high-pressure cell designed for the $scCO_2$ processing[30] and exposed to $scCO_2$ at T = 36 ºC and given pressures up to 25 MPa for 2 h. The system was subsequently depressurized to atmospheric pressure within 10 s, which allowed one to preserve the film structures present in CO_2 via the vitrification process of the polymer matrix[41]. Hereafter I call the nanocomposite films with and without the above $scCO_2$ procedure as ‘‘treated’’ and ‘‘untreated’’ (but annealed at T = 160 ºC in vacuum for 24 h) films, respectively, unless otherwise stated.

2-3-3. Atomic Force Microscope (AFM)

An atomic force microscope (AFM, Dimension 3100, Digital Instruments) was employed to characterize the surface morphologies of the polymer nanocomposite thin films before and after the $scCO_2$ process. For contact mode measurements, a triangular silicon nitride cantilever (NP series, Veeco Instruments) having a nominal spring constant value of 0.06 Nm^{-1} with a gold backside coating was utilized. Topographic and lateral force images were simultaneously obtained at appropriate scanning rates (0.5-1 Hz). All images were flatten-processed using the Nanoscope 5.12 (Digital Instruments) software.

2-3-4. X-ray Photoelectron Spectroscopy (XPS)

X-Ray photoelectron spectroscopy measurements were conducted by a Quantera SXM (ULVAC-PHI, Inc.) equipped with a C_{60}^{+} sputter ion gun. A monochromatic aluminium Ka X-ray source was used at a power of 25 W with a beam diameter of 100 mm. The acceleration voltage and area of raster scanning of the sputter ion beam were 10 kV and 2×2 mm^2, respectively. The depth (from the film surface) of the measured areas was calibrated by the sputter rate (16.2 nm/min). The concentration profile of the POSS nanoparticles for the treated film was determined from quantitative oxygen 1s signals in the XPS spectra.

2-3-5. Scanning Electron Microscope (SEM)

Secondary electron images of the surface morphologies were obtained by a scanning electron microscope (SEM, LEO 1550) without any metal coating on a sample surface. The working distance between the sample surface and the bottom of the objective lens was 2 mm. The acceleration energy of an incident electron beam was 1.5 kV.

2-3-6. Neutron Reflectivity (NR)

NR experiments were performed on the NG7 neutron spectrometer at Center for Neutron Research, National Institute of Standards and Technology. For the NR experiments, deuterated PS (d-PS, M_w = 119,500, M_w / M_m = 1.05, Polymer Source Inc.) was used to illuminate the surface segregation of the nanoparticles due to the contrast enhancement between the d-PS and POSS nanoparticles coated with the PMMA chains. I also confirmed that the effect of the deuterium labeling on the surface structure is ignored. A d-PS thin film containing 10 wt% of the POSS–PMMA nanoparticles was prepared by spin-coating on a 3-inched HF-etched silicon wafer. The original film thickness was approximately 40 nm, which is equivalent to 4.5R_g. The NR profiles for the untreated and treated films were measured at room temperature as a function of the wave vector normal to the surface, q_z

= ($4\pi\sin\theta$)/λ, where λ is the wavelength of the neutron beam (4.7 Å) and q is the incident angle, respectively. The NR data corrected for the background scattering were analyzed by comparing the observed reflectivities with the calculated ones based on model density profiles having three parameters: film thickness, scattering length density (SLD), and interfacial root-mean-square (rms) roughness (s) at the interfaces expressed by an error function[42]. The volume fraction of the nanoparticles in the nanoparticle-rich layer at the topmost surface was obtained by using the following equation:

$$SLD_{mix} = SLD_{POSS}\phi_{POSS} + SLD_{dPS}(1 - \phi_{POSS}), \qquad (1)$$

where SLD_{mix}, SLD_{dPS} and SLD_{POSS} are the *SLD* values for the top layer, pure d-PS (SLD_{dPS} = 6.0×10^{-6} Å^{-2}), and POSS-PMMA nanoparticles (SLD_{POSS} = 1.0×10^{-6} Å^{-2}), respectively, and ϕ_{POSS} is the volume fraction of the POSS-PMMA nanoparticles. In situ NR experiments were also conducted for the same PS/POSS-PMMA film. The details of the in situ experiments have been described elsewhere[30]. It should be noted that due to the strong background scattering (i.e., density fluctuations) from CO_2 at q > 0.1 Å^{-1}, the excess scattering from the surface segregation layer, as described below, could not be detected in the presence of CO_2.

2-3-7. X-ray Reflectivity (XR)

The film thicknesses before and after the scCO_2 processing were determined by using X-ray reflectivity at the X10B beamline of the National Synchrotron Light Source (NSLS), Brookhaven National Laboratory (BNL) with a photon energy of 14.1 keV (i.e., X-ray wavelength (λ) of 0.87 Å). The XR data were fitted by using a standard multilayer fitting routine for a dispersion value (δ) in the X-ray refractive index.

2-4. Results and Discussion

2-4-1. Anomalous Excess Swelling of Nanocomposite Thin Films

Fig. 2-1 shows the linear dilation of the treated PS/POSS-PMMA thin films (about 120 nm thick) with the different CO_2 process pressures. The S_f values was calculated by the following equation, $S_f = (L_1 - L_0)/L_0$ where L_0 and L_1 are the original and swollen film thickness determined by XR, respectively. From the figure we can see the swelling maximum at the density fluctuation ridge condition (i.e., P_{ridge} = 8.2 MPa at T = 36 °C), where the swelling maximum of the pure PS thin films in $scCO_2$ occurs[25, 30]. As shown in the inset of Fig. 2-1, the functional form of the swelling amplitude follows that of the calculated density fluctuations at T = 36 °C based on the empirical equation of state for CO_2 as a function of pressure[43]. In addition, *in-situ* NR for the d-PS/POSS-PMMA thin film proved that the swelling isotherm in CO_2 is in good agreement with Fig. 2-1, except for the fact that the magnitude of the in-situ S_f values is slightly higher (ca. 1.0 nm decrease in the film thickness after the quench, as reported previously for the pure PS films[40, 41]). Moreover, it was found that the surface roughness at the polymer/CO_2 interface remains unchanged before and after the quench. Hence, the experimental results clarify that the similar anomalous swelling of the polymer nanocomposite thin films occurs near the ridge condition ($6.2 \leq P \leq 10.3$MPa) and the swollen structures of the nanocomposite films in CO_2 can be preserved via the pressure quench. Note that all the treated polymer nanocomposite thin films do not have any nanometer-to micron-sized voids even after by the rapid quench confirmed by using small-angle x-ray scattering experiments with reflection geometry[44].

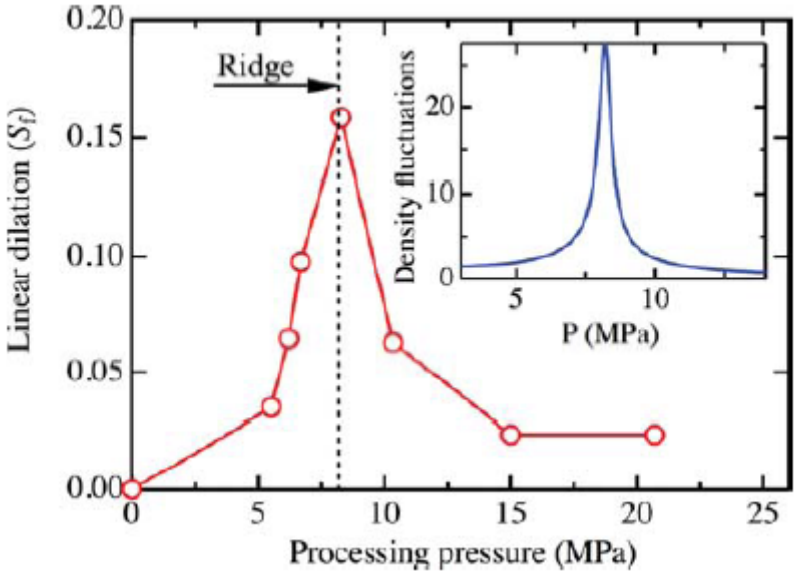

Fig. 2-1 Linear dilation (S_f) of the treated PS/POSS–PMMA films as a function of the CO_2 processing pressures. The dotted line corresponds to the density fluctuation ridge condition at T = 36 ºC. In the inset, the calculated density fluctuations in a pure CO_2 phase are plotted.

2-4-2. Surface Morphology of scCO2-treated PS/POSS-PMMA Thin Film

Fig. 2-2 summarizes the corresponding surface morphologies of the untreated and treated PS/POSS-PMMA thin films measured by AFM.

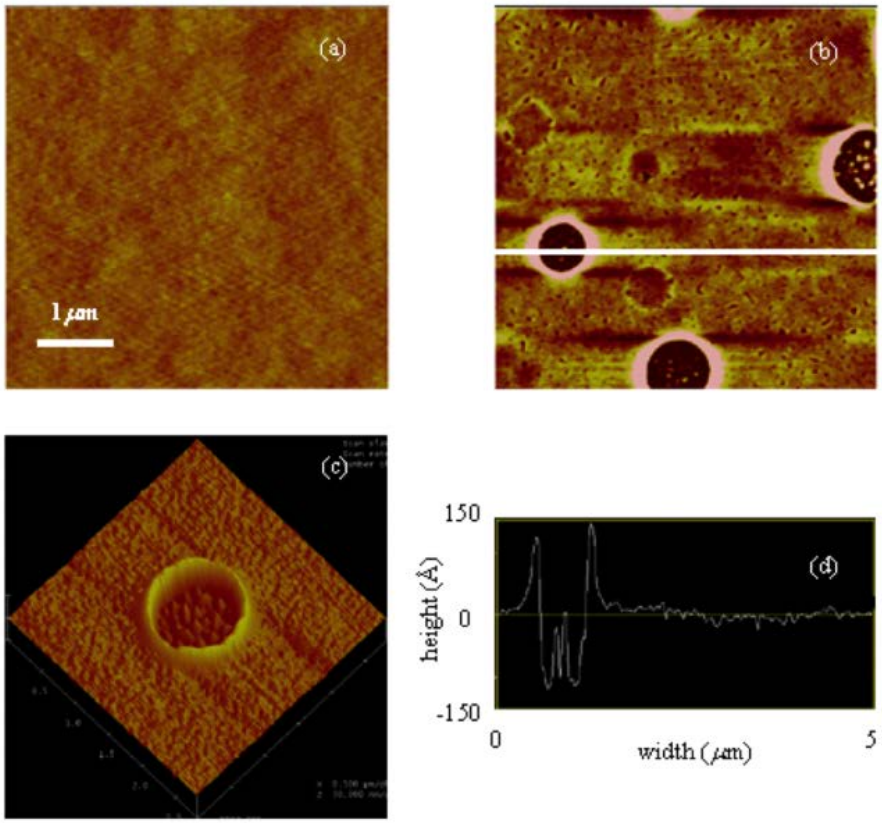

Fig. 2-2 Topographic images for the PS/POSS-PMMA thin films with (a) thermal annealing at T = 160 ºC for 24 h in vacuum and (b) the ridge condition (T = 36 ℃ and P = 8.2MPa) in CO_2. The scan sizes and height scales for the images are 5×5 μm^2 and 0-10 nm, respectively. Fig. 2-2 (c) and 2-2 (d) correspond to the cross-sectional height profile along the white line in (b) and the expanded view of the rim-shaped structure shown in (b), respectively.

We can see that the film annealed at T = 160 ºC in vacuum for 24 h still has the flat and smooth surface (Fig. 2-2 (a)). The featureless surface was also observed in the untreated (but annealed) PS/POSS-PS, PMMA/POSS-PMMA, PMMA/POSS-PS films and PS/PCBM thin films, indicating that these nanoparticles are compatible with the polymers. It is expected that such long PS and PMMA (M_w > 100,000) ligand chains attached to the POSS nanoparticles have unfavorable mixing energies to cause phase separation. However, it is reported that this unfavorable process is offset by an enthalpy gain due to an increase in molecular contacts at dispersed nanoparticle surfaces[45]. On the other hand, when the film was subjected to the $scCO_2$ process at the ridge condition (P_{ridge} = 8.2

MPa), many rim-shaped structures with sub-micron to a few micron sizes were present (Fig. 2-2 (b)). Furthermore, as shown in Fig. 2-2 (c), the rim-shaped structures show many spherical structures of the POSS nanoparticles clustered together (the average diameter of about 120 nm) inside the rim. It was also found that the surface structures do not form any crystals by using a grazing incidence X-ray diffraction technique. These rim-shaped structures remind us of dewetting structures developed in ultrathin polymer bilayer films on solid substrates[46-48]. However, as shown in Fig. 2-2 (d), the cross sectional profile of the surface topographic image of Fig. 2-2 (b) revealed that the rim-shaped structures are formed only near the topmost surface area (~ 10 nm in thickness depth) of the entire film (116.7 nm in thickness). In addition, I confirmed that there is no significant time evolution of the surface segregated structures within the CO_2 exposure times up to 24 h. Thus, this experimental evidence leads to the conclusion that the rim-like structures are not related to the dewetting process. It should be also emphasized that the surface morphologies of the treated films at the slightly off-ridge conditions ($6.2 \leq P \leq 10.3$ MPa), where the anomalous swelling still occurs (Fig. 2-1), remain featureless. This pressure dependence of the surface segregation is not related to the effect of T_g since the CO_2-induced glass-liquid transition pressures for PS and PMMA thin films at almost the same temperature (T = 35 ºC) are much lower (5 MPa[49] for PS and 5.7 MPa[50] for PMMA, respectively) than the ridge condition (P_{ridge} = 8.2 MPa at T = 36 ºC).

Fig. 2-3 presents the time evolution of the surface morphology of the treated PS/POSS-PMMA thin films. I confirmed that the surface morphology did not change with the further treatment for more than 2 h. From these images it is revealed that the growth of the nano-aggregates takes place at the polymer/CO_2 interface with the time evolution. This suggests the incorporation of the surface migrating nanoparticles into the nuclei of the nano-aggregates.

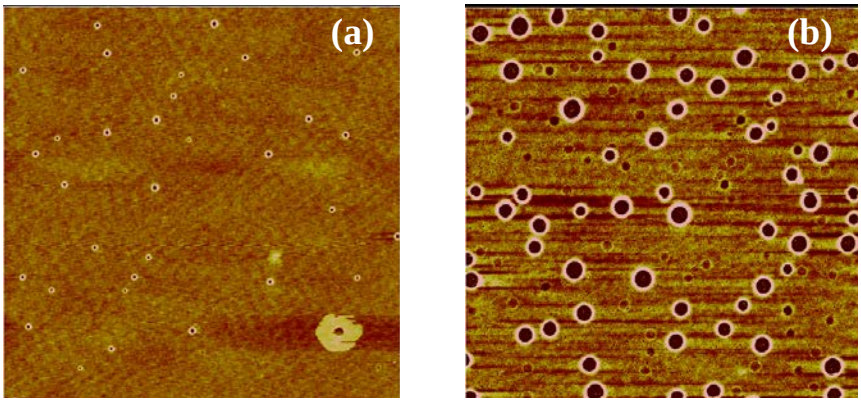

Fig. 2-3 Topographic images for the PS/POSS-PMMA thin films treated at the ridge condition (T = 36 °C and P = 8.2MPa) in CO_2 for (a) 0.5 h and (b) 2 h. The scan sizes and height scales for the images are 20×20 μm^2 and 0-10 nm, respectively.

2-4-3. Depth Analyses for scCO2-treated PS/POSS-PMMA Thin Film

In order to further characterize the surface structures of the treated films, NR experiments were conducted in air. Fig. 2-4 (a) shows the NR profiles for the untreated d-PS/POSS–PMMA films (black circles) and treated d-PS/POSS–PMMA films at the ridge condition (red circles). The black solid line corresponds to the calculated reflectivity for the untreated film based on a three-layer model, i.e., Si, SiO_2, and d-PS/POSS–PMMA layers. As shown in the inset of Fig. 2-4 (a), the best-fit to the data clarifies that the d-PS/POSS–PMMA layer is homogeneous within the entire film. On the other hand, the same three-layer model could not fit the NR profile for the treated film, especially at the high *q*-region where the excess scattering emerges. As shown in the inset of Fig. 2-4 (b), I instead used a four-layer model in which an additional layer was introduced at the topmost of the film, giving us a reasonable fit to the NR data (the red solid line shown in Fig. 2-4 (a)). As a result, the thickness of the additional top layer is estimated to be 3 nm and the concentration of the POSS–PMMA nanoparticles in the top layer is estimated to be approximately 70 wt%, which is much higher than the original one (10 wt%).

Note that the coherent length of the neutron beams is comparable (~ 1 μm) to the average size of the rim structures such that their roughness may contribute to the NR profile. Thus I should use the parameters obtained by NR only for semi-quantitative comparison. The existence of the POSS-rich layer at the surface is further confirmed by XPS, whose data are in agreement with the NR results (Fig. 2-4 (c)). Hence, this consistency between the two independent surface sensitive characterization techniques for the same sample leads to conclude that the POSS nanoparticles are preferentially migrated to the topmost surface after the $scCO_2$ treatment in the close vicinity of the ridge condition.

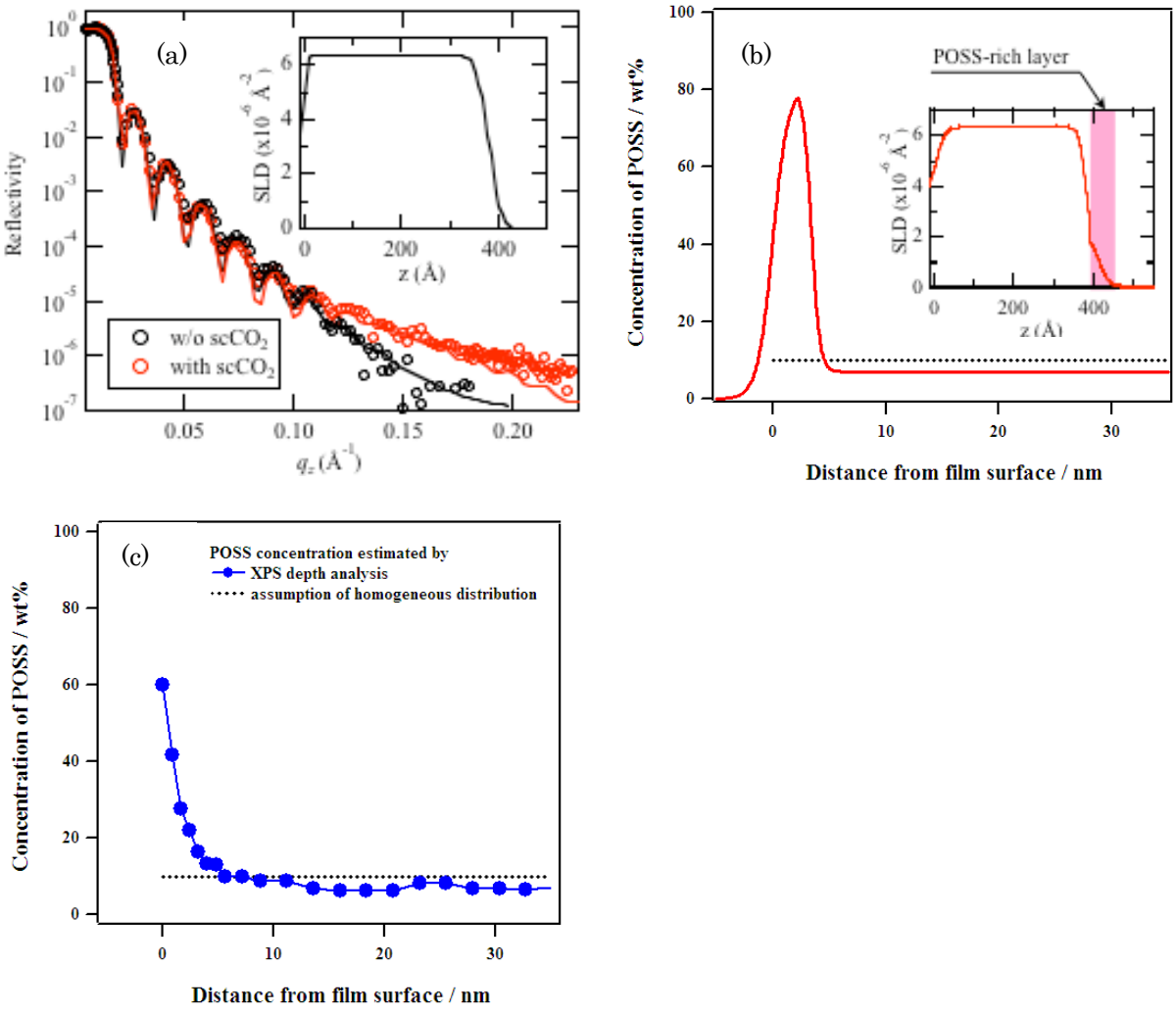

Fig. 2-4 (a) Measured (circles) and calculated (solid lines) NR curves for the d-PS/POSS-PMMA film before (black) and after (red) the $scCO_2$ treatment. The inset shows the obtained *SLD* profiles vs. distance from the substrate for the untreated film. Concentration profiles of the POSS nanoparticles in the direction normal to the surface obtained by (b) NR (red line) and (c) XPS (blue line) for the treated film at the ridge condition. The inset in (b) shows the corresponding *SLD* profile for the treated film that gave us the calculated NR curve indicated by the red solid line shown in (a). The dotted line in (b) and (c) shows concentration profile which assumes the homogeneous distribution.

2-4-4. Generality of Surface Segregation

Next, I show that the surface segregation occurs for different polymer/nanoparticle interactions. As shown in Fig. 2-5 (a) and (b), similar surface segregation structures of the POSS nanoparticles were observed after the $scCO_2$ treatment in the close vicinity of the ridge condition for both the treated PS/POSS–PS and PMMA/ POSS–PMMA thin films where the adverse monomeric enthalpic effects

between the polymer and nanoparticle are minimal. Hence, these results indicate that the enthalpic contributions are not the central driving force for the $scCO_2$-induced surface segregation. Rather, an entropic effect imposed on the polymer chains owing to the presence of the nanoparticles, the so-called ‘‘depletion attraction’’,[51] should be crucial. In fact, as shown in Fig. 2-1, the polymer chains exposed to highly compressible $scCO_2$ are anomalously expanded in the presence of the nanoparticles such that similar expelling of the nanoparticles to the free surface[22-24] would result in an entropic gain. Moreover, as shown in Fig. 2-5 (c) and (d), we can see that surface segregation occurs in the treated PS/PCBM thin films, again, only near the ridge condition, while the PCBM nano-aggregates are formed onto the film surface and are hemispherical with the diameters ranging from 0.1 μm to 1 μm and the heights of 50-200 nm.

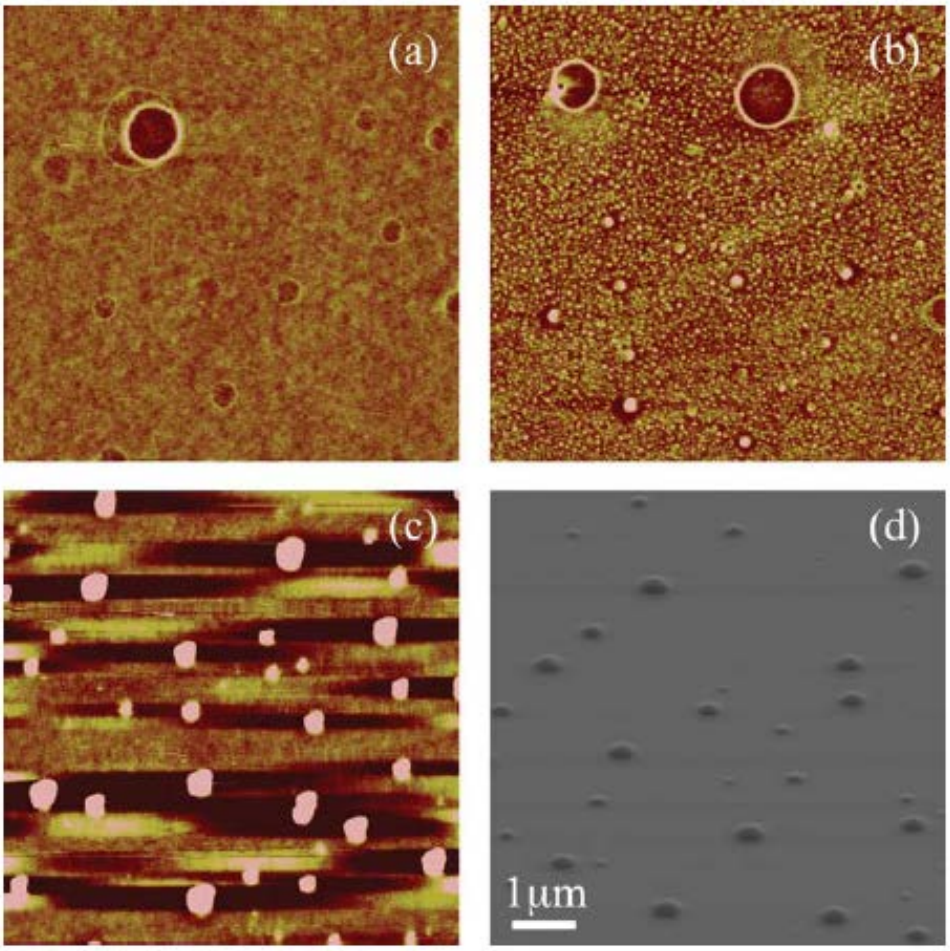

Fig 2-5 Surface morphologies for the treated (a) PS/POSS-PS (b) PMMA/POSS-PMMA and (c) the treated PS/PCBM thin film at the ridge condition and (d) the scanning electron microscope image for the treated PS/PCBM thin film. The scan sizes and height scales for the AFM images are 10×10 μm^2 and 0-10 nm, respectively.

Fig. 2-6 (a) and (b) present the topographic surface morphologies of the as-spun and thermally annealed PS/clay thin films (untreated, 50 nm in thickness) measured by AFM. We can see that the film annealed at T = 170 ºC in vacuum for 2 h has a rough surface, while the surface of the original as-spun film is relatively flat. Fig. 2-6 (d) and (e) correspond to the cross-sectional profiles of Fig. 2-6 (a) and (b), respectively, indicating that the dewetting takes place during the annealing process. From the x-ray reflectivity measurement for the as-spun PS/clay film, it was observed the monolayer formation of the clay particles at the substrate, indicating that the strong affinity of the clays for a native oxide layer and the dewetting is caused by the poor interaction between the clay particle and PS. Fig. 2-6 (c) and (f) are the surface morphologies of the $scCO_2$ treated PS/clay thin film (1 wt%) at the ridge condition and its cross-sectional profile, respectively. Interestingly, no dewetting was observed even after 23 h exposure time in $scCO_2$ and rather the surface became rougher due to the segregation of the clay particle (the bright spots in the AFM images correspond to the clay nanoparticles).

In order to quantitatively characterize the surface segregation structures of the clay nanoparticles, I conducted an image analysis on the lateral force images, which offer a frictional force contrast on a surface. This allows us to quantify the surface exposing clay nanoparticles with relatively large difference in the frictional nature. The calculated areas of the surface exposing clays in the PS/clay thin film (both 50 and 100 nm thickness) are presented in Fig. 2-7. For the as-spun films of both 50 and 100 nm in thick, approximately 7.5 % in topmost area was covered by the clay particles. On the other hand, the surface coverage of the particles after exposing to $scCO_2$ increased up to more than 10 % for both films, which corresponds to an approximately 40 % increase from the unexposed film. Hence, it is obvious that the $scCO_2$ treatment induces the surface segregation of the clay particles. From the figure we see no significant time dependence of the surface exposed clay nanoparticles after 1 h exposure, suggesting the surface segregated structure is an equilibrium state. In addition, it was also found that the observed surface segregation is very sensitive to employed T and P conditions; it can take place only at the ridge condition

Hence, the results suggest that the $scCO_2$-induced surface segregation of polymer soluble nanoparticles is rather general, while the shapes of the nano-aggregates may be altered. I also performed the x-ray reflectivity measurements for the untreated (but annealed) PS/PCBM films as well as the PS/clay thin films and the results revealed the presence of the interfacial segregation layer (about 20 nm) of PCBM nanoparticles at the substrate interface. This suggests that $scCO_2$ would screen the strong interaction between the PCBM nanoparticles and substrate.

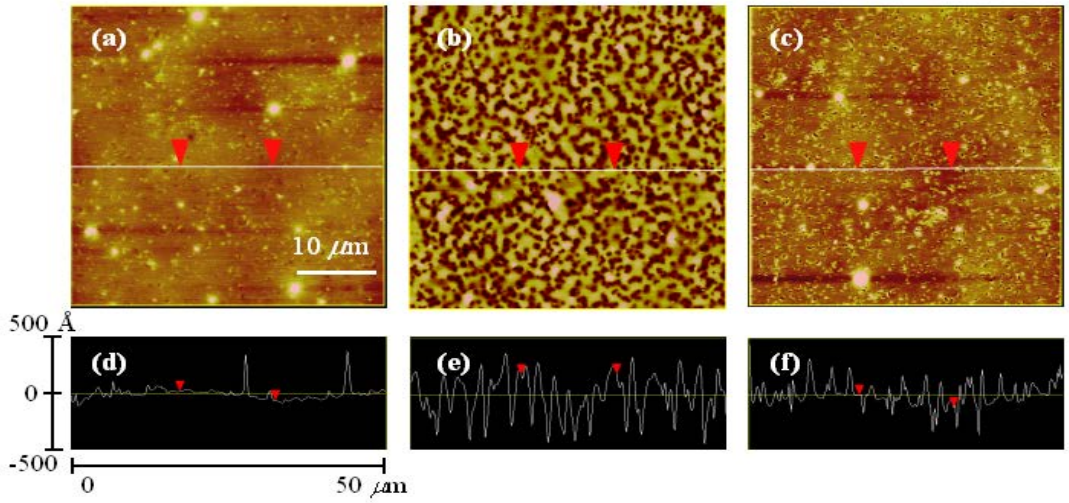

Fig. 2-6 Topographic images for the (a) as-spun, (b) thermally annealed (T = 170 ºC for 24 h in vacuum) and (c) CO_2 treated (P = 8.2 MPa and T = 36 ºC for 1 h) PS/clay thin films. The scan sizes and height scales for the images are 50×50 μm^2 and 0-100 nm, respectively. (d), (e) and (f) show the cross-sectional profiles along the white lines in (a), (b) and (c), respectively. The height scales for these profiles are 0-100 nm.

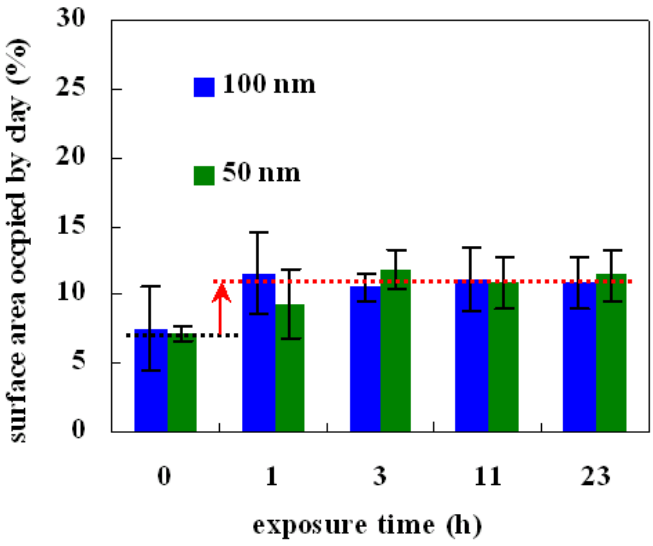

Fig. 2-7 Calculated surface areas occupied by the clay nanoparticles as a function of CO_2 exposure time. The legend in the figure presents the film thickness.

2-4-5. Critical Thickness for Surface Segregation

In order to further elucidate the phenomenon, the thickness dependence of the surface morphologies was imvestigated by using AFM. For this purpose I examined the PS/PCBM thin films with different film thickness. Interestingly, the surface segregation structures of the treated PS/PCBM thin films at the ridge disappear when the film thickness decreases to less than around 45 nm (Fig. 2-8). I confirmed the presence of the same critical threshold of the $scCO_2$-induced surface segregation for the treated PS/POSS-PMMA films. Consequently, the aforementioned entropic penalty imposed on the polymer chains alone is not sufficient to explain the thickness dependence of the nanoparticle dispersion induced by highly compressible $scCO_2$.

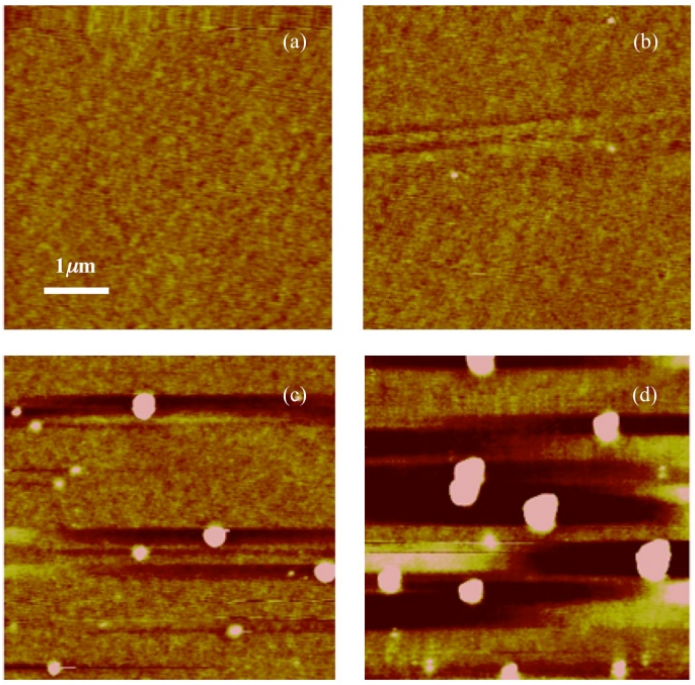

Fig. 2-8 AFM topographic images for the PS/PCBM films with different film thickness: (a) 19 nm; (b) 38 nm; (c) 55 nm; (d) 93 nm. The scan sizes and height scales for all the images are 5×5 μm^2 and 0-10 nm, respectively.

2-4-6. Mechanism

i) Low-density surface layer and concentration gradient of CO_2 at the ridge condition

The question is what is special about the ridge condition for polymer nanocomposite thin films? Koga and co-workers have previously shown that the treated pure PS thin films at the ridge have homogeneous low-density formation below about $4R_g$ thick, while heterogeneous low-density

distributions are developed for the treated PS films above the thickness[41]. This low-density formation is resulted from freezing of the swollen structures in CO_2 by the vitrification process[40]. The heterogeneous distributions are attributed to the limited penetration depth of the excess CO_2 absorption in the polymer matrix[25, 30].

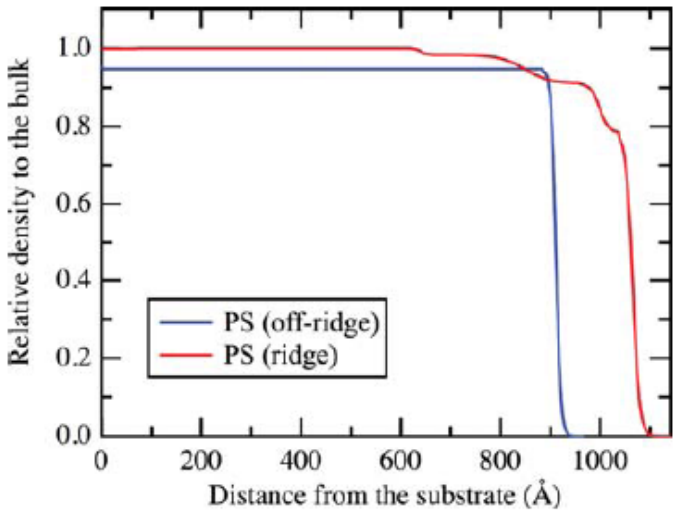

Fig. 2-9 Density profiles of the pure PS thin films (L_0 = 89 nm) treated at the ridge condition (T = 36 ºC and P = 8.2 MPa indicated in red and the off-ridge (T = 36 ºC and P = 6.7 MPa indicated in blue) conditions. The dispersion (δ) values, which are proportional to the density of the film, were converted into the density relative to the bulk by using the measured x-ray dispersion value of the untreated PS film ($\delta = 1.15\times10^{-6}$).

Fig. 2-9 shows a representative density profile of the treated pure PS thin film (L_0 = 89 nm, corresponding to 7.4 R_g thick) obtained by using XR in conjunction with the Fourier Transform (FT) analysis method developed for low-contrast multilayer systems[52]. From the figure we can see that a layer of about 10 nm thick is formed at the PS/air interface with a much reduced density of about ρ = 0.80 gcm^{-1} and a relatively sharp interface of about 2 nm with the layers beneath. The subsequent layers also have reduced density, but these layers are more diffuse and decay over a region of approximately 35 nm towards a uniform layer with the bulk density (ρ = 1.05 gcm^{-1}). Hence, the critical threshold (45 nm thick) for the phase behavior is in good agreement with the penetration length of the excess absorption of CO_2 molecules. The correlation between the surface segregation and the concentration gradient is further verified by the XR experiment for the treated PS film (L_0 = 89 nm) at P = 6.7 MPa and T = 36 ºC where no surface segregation occurs: there is a homogeneous low-density distribution, while a small reduction of density (5%) compared to the

bulk is developed (Fig. 2-9). The larger penetration depth of CO_2 molecules (at least 90 nm) at the slightly off-ridge conditions may be attributed to the difference in the correlation length (or a cluster size, ξ) of the CO_2 molecules in the pure fluid phase (ξ = 0.6 nm) compared to that at the ridge condition (ξ = 1.5 nm)[28]. Detailed studies on the relationship between the cluster size and the penetration depth deserve future work. Thus it is pointed out that a more dominant factor for the phase transition of the nanoparticle dispersion is the formation of the CO_2 concentration gradient in the polymer matrix.

Before turning to detailed discussion of the mechanism driven by the concentration gradient of the fluid, I should introduce an intriguing simulation study on dynamics of particles in the course of phase separation of a binary (A/B) mixture[39]. Makino et al. showed when the system is quenched into the unstable two phase region, the particles which are initially dispersed in the single-phase (but have a preference for the B component) move to the B phase by taking advantage of a concentration gradient of the volume fraction at the two-phase domain boundary. The particles located far from the boundary, on the other hand, hardly move because the concentration gradient as the driving force is too small for the particles. In this study, it is anticipated the formation of a critical wetting layer of CO_2 molecules onto the nanoparticle surfaces, as described in the Introduction. Findenegg has first reported the excess surface adsorption of ethylene and sulfur hexafluoride molecules on graphite carbon black particles[53] and similar excess adsorption of CO_2 molecules on various particles including silica and octadecyl- bonded silica has also been reported[18-20]. Interestingly, it turned out that the temperature and pressure conditions where the degree of the excess adsorption becomes a maximum correspond to the density fluctuation ridge, while it has been never mentioned in the literature. Furthermore, Lal et al. showed that the excess adsorption also takes place in particles with ligand molecules attached, while the degree of the adsorption depends on the interactions between solvent and ligand molecules[54, 55].

ii) Proposed mechanism of surface segregation of nanoparticles

It comes to propose the mechanism of the scCO_2-induced phenomenon. When polymer nanocomposite thin films are exposed to scCO_2 in the highly compressible region near the critical point, the two anomalous phenomena are induced independently: (i) excess absorption of CO_2 molecules into the polymer matrix and (ii) excess adsorption of CO_2 molecules on the nanoparticle surfaces. The excess absorption expands polymer chains homogeneously or heterogeneously, depending on the balance between the penetration length of the compressed CO_2 molecules and film thickness. When the homogeneous excess absorption occurs, the resultant anomalous expansion of the polymer chains may reduce the entropic penalty of the chains without expelling the nanoparticles to the free surface, allowing the accommodation of the ‘‘CO_2-wetted’’ nanoparticles within the films. By contrast, when the film thickness is beyond the penetration length scale of the fluid molecules, a concentration gradient of the fluid is developed at the polymer/CO_2 interface. This concentration gradient provokes instability of the dispersion of the CO_2-wetted nanoparticles and thereby migration of the nanoparticles preferentially to the topmost CO_2-rich region through the

concentration gradient. The nanoparticles migrated to the surface would be then coagulated together[39] due to the attractive interaction among them, resulting in the large aggregate structures at the polymer surface as seen in Figs. A further study on the effect of a particle size relative to the radius of polymer gyration and the key for the entropy-driven segregation of polymer-soluble nanoparticles[22, 23] are worth being clarified. In order to validate the proposed mechanism, a numerical method for computing the dynamics of particles embedded in ‘‘A’’ (polymer) and ‘‘B’’ (solvent) fluids is also utilized. Within this primitive model, the following three effects were taken into account: (i) affinities among a particle, A- and B-fluids, (ii) phase separation dynamics of ‘‘A/B’’ binary fluids, and (iii) a hydrodynamic effect on particles and phase separation dynamics. As a result, it was found that the particles near the interfaces tend to migrate to the solvent-rich regions by taking advantage of the concentration gradient there, while the particles far from the interfaces remain within the film. In addition, the results indicate that some particles migrated are subsequently coagulated together by the attractive interaction mediated through CO_2 wetting layers around the particles. Thus, these numerical results obtained from our primitive model, which does not consider detailed thermodynamic modeling of CO_2 (such as long-range density fluctuations), well describe the experimental findings. The concept of the mentioned mechanism was already shown in Fig. 1-8 in Chapter 1.

iii) Thermodynamic consideration

Finally, it is worth discussing about the surface segregated structures from the thermodynamic point of view. Kim and Shaughnessy predicted similar aggregated structures of nanoparticles bulged into a polymer brush in air and discussed the origin of the baguette shape of the aggregates at the polymer/air interface based on the spreading coefficient and the entry coefficient[56]. I extend their concept to our $scCO_2$ case by introducing the three relevant surface tensions associated with the surface segregation in CO_2: γ_{pc} (polymer/CO_2), γ_{pa} (polymer/nanoaggregate), γ_{ac} (nano-aggregate/CO_2). It is well known that these parameters determine the spreading coefficient $S \equiv \gamma_{pc} - \gamma_{pa} - \gamma_{ac}$ and the entry coefficient $E \equiv \gamma_{pc} + \gamma_{pa} - \gamma_{ac}$[57, 58]. As seen in the previous figures, $S < 0$ (the nano-aggregates do not wet the polymer) is expected for all the nanocomposite thin films. This may be understood by considering the PS/POSS–PMMA system where the long PMMA chains[47] would cover the POSS nanoparticles/ nano-aggregates. According to previous experimental results,[30] the interaction parameters, which are proportional to the γ_{pc} values, between PS and CO_2 and between PMMA and CO_2 are significantly ‘‘diluted’’ and are very close to each other at the ridge condition[29]. Therefore, $\gamma_{pc} - \gamma_{ac}$ ($= \gamma_{PS\text{-}CO2} - \gamma_{PMMA–CO2} \approx 0$ for the PS/POSS–PMMA case) $< \gamma_{pa}$ ($\gamma_{PS–PMMA}$) would be possible, resulting in $S < 0$ at the ridge. Moreover, the crude approximation of $\gamma_{pc} \approx \gamma_{ac}$ for PS/POSS–PMMA at the ridge may also lead to $E \approx \gamma_{ac} > 0$. This suggests that the entry of the POSS nano-aggregates into the PS matrix is thermodynamically feasible, although it is difficult for AFM to quantify the degree of the entry, as seen in Fig. 2-2 (d). Although the above arguments are not quite conclusive because I do not know the exact surface tensions in CO_2 at the

ridge, I believe that a delicate counter balance among the three parameters (γ_{pc} and γ_{ac} are controllable through variations in the excess absorption of CO_2 and γ_{pa} is adjustable through variations in particle coatings) plays crucial roles in determining the final morphology of the nano-aggregates at the polymer surface at equilibrium in the presence of density fluctuating $scCO_2$.

2-5. Conclusion

In Chapter 2, I have shown the unique surface segregation or/and nano-aggregates of functionalized polyhedral oligomeric silsesquioxane (POSS), phenyl C61 butyric acid methyl ester (PCBM), organoclay nanoparticles at the polymer-CO_2 interface induced by highly compressible supercritical CO_2 ($scCO_2$). It was found the formation of nanoparticles-rich layers at the polymer/air interface for different polymers and nanoparticles (with different ligands) after the $scCO_2$ treatment in the close vicinity of the density fluctuation ridge where the anomalous swelling of the polymer chains due to the excess absorption of CO_2 molecules becomes maximum. The mechanism of the CO_2-induced surface segregation can be partially understood by the concept of a ‘‘depletion attraction’’: the polymer chains push the nanoparticles to the polymer/CO_2 interface such that the entropic penalty imposed on the polymer chains is recovered. However, this alone is not sufficient to explain the phase behavior of not only the $scCO_2$ treated films at the slightly off-ridge conditions, where the anomalous swelling of the polymer chains still occurs, but the much thinner (less than about $4R_g$) films treated at the ridge: the uniform dispersion of the nanoparticles is favored instead. I have revealed that the surface segregation is related to the formation of a concentration gradient of the fluid at the polymer/CO_2 interface during the course of the $scCO_2$ process. I propose that this concentration gradient as a consequence of the limited penetration power of the highly compressible fluid provokes the instability of the system and the nanoparticles ‘‘coated’’ with a critical wetting layer of CO_2 molecules near the critical point[18-20] are preferentially migrated to the CO_2-rich region through the concentration gradient. Hence, the experimental findings would provide a robust, environmentally green, low-temperature pathway to create a self-organized surface segregation layer for various organic-inorganic hybrid devices such as solar cells, thin film transistors, and light-emitting diode or homogeneous low density polymer nanocomposite thin films to be used for ultra low-k insulators or catalytic materials. Further experiments on the local structures of the nano-aggregates using different methodologies such as a three-dimensional transmission electron microscopy tomography are needed to provide a better understanding of how the shapes of the nano-aggregates are determined as a thermodynamically stable state.

2-6. References

1. W.Zheng; X.Lu; S.-C.Wong. *J.Appl.Polym.Sci.* **2004,** 91, 2781.
2. D.Cho; S.Lee; G.Yang; H.Fukushima; L.T.Drzal. *Macromol. Mater. Eng.* **2005,** 290, 179.
3. Garca, I.; Tercjak, A.; Rueda, L.; Mondragon, I. *Macromolecules* **2008,** 41, 9295.
4. Steckel, J. S.; Coe-Sullivan, S.; Bulovi, V.; Bawendi, M. G. *Adv. Mater.* **2003,** 15, (21), 1862-1866.
5. McDonald, S. A.; Konstantatos, G.; Zhang, S.; Cyr, P. W.; Klem, E. J. D.; Levina, L.; Sargent, E. H. *Nat. Mater.* **2005,** 4, 138-142.
6. McElwain; S., T. B.; Schadler, L. S.; Sawyer, W. G. *Tribology Transactions* **2008,** 51, (3), 247‐253.
7. Barnes, K. A.; Karim, A.; Douglas, J. F.; Nakatani, A. I.; Gruell, H.; Amis, E. J. *Macromolecules* **2000,** 33, (11), 4177–4185.
8. Mackay, M. E.; Hong, Y.; Jeong, M.; Hong, S.; Russell, T. P.; Hawker, C. J.; Vestberg, R.; Douglas, J. F. *Langmuir* **2002,** 18, 1877–1882.
9. Krishnan, R. S.; Mackay, M. E.; Hawker, C. J.; Horn, B. V. *Langmuir* **2005,** 21, 5770–5776.
10. Krishnan, R. S.; Mackay, M. E.; Duxbury, P. M.; Pastor, A.; Hawker, C. J.; Horn, B. V.; Asokan, S.; Wong, M. S. *Nano Lett.* **2007,** 7, (2), 484-489.
11. Balazs, A. C.; Emrick, T.; Russell, T. P. *Science* **2006,** 314, 1107.
12. Balazs, A. C. *Nat. Mater.* **2007,** 6, 94.
13. Stamm, M.; Sommer, J.-U. *Nat. Mater.* **2007,** 6, 260.
14. Glogowski, E.; Tangirala, R.; Russell, T. P.; Emrick, T. *J. Polym. Sci. A, Polym. Chem.* **2006,** 44, (17), 5076-5086.
15. Owen, J. S.; Park, J.; Trudeau, P.-E.; Alivisatos, A. P. *J. Am. Chem. Soc.* **2008,** 130, (37), 12279–12281.
16. Zhao, Y.; Thorkelsson, K.; Mastroianni, A. J.; Schilling, T.; Luther, J. M.; Rancatore, B. J.; Matsunaga, K.; Jinnai, H.; Wu, Y.; Poulsen, D.; Fréchet, J. M. J.; Alivisatos, A. P.; Xu, T. *Nat. Mater.* **2009,** 8, (12), 979-985.
17. McHugh, M. A.; Krukonis, V. J., *Supercritical Fluid Extraction: Principles and Practice.* Butterworth-Heinemann: Boston, 1994.
18. Blümel, S.; Findenegg, G. H. *Phys. Rev. Lett.* **1985,** 54, 447-450.
19. Strubinger, J. R.; Parcher, J. F. *Anal. Chem.* **1989,** 61, (9), 951-955.
20. Strubinger, J. R.; Song, H.; Parcher, J. F. *Anal. Chem.* **1991,** 63, (2), 98-103.
21. Gupta, S.; Zhang, Q.; Emrick, T.; Balazs, A. C.; Russell, T. P. *Nat. Mater.* **2006,** 5, 229.
22. Lee, J. Y.; Buxton, G. A.; Balaza, A. C. *J. Chem. Phys.* **2004,** 121, 5531.
23. S.Tyagi; D.R.Lee; G.A.Buxton; A.C.Balaza. *Macromolecules* **2004,** 38, 9160.
24. Lee, J.-Y.; Zhang, Q.; Emrick, T.; Crosby, A. J. *Macromolecules* **2006,** 39, 7392.
25. Koga, T.; Seo, Y.-S.; Zhang, Y.; Shin, K.; Kusano, K.; Nishikawa, K.; Rafailovich, M. H.; Sokolov, J. C.; Chu, B.; Peiffer, D.; Occhiogrosso, R.; Satija, S. K. *Phys. Rev. Lett.* **2002,** 89, 125506

26. Tucker, S. C. *Chem. Rev.* **1999,** 99, 391.
27. Stanley, H. E., *Introduction to Phase Transition and Critical Phenomena*. Oxford University Press: Oxford, 1971.
28. K.Nishikawa; I.Tanaka; Y.Amemiya. *J. Phys. Chem.* **1996,** 100, 418.
29. Sirard, S. M.; Ziegler, K. J.; Sanchez, I. C.; Green, P. F.; Johnston, K. P. *Macromolecules* **2002,** 35, 1928–1935.
30. Koga, T.; Seo, Y.-S.; Shin, K.; Zhang, Y.; Rafailovich, M. H.; Sokolov, J. C.; Chu, B.; Satija, S. K. *Macromolecules* **2003,** 36, (14), 5236–5243.
31. Koga, T.; Y. Ji, Y. S. S.; Gordon, C.; Qu, F.; Rafailovich, M. H.; Sokolov, J. C.; Satija, S. K. *J. Polym. Sci. Part B. Polym. Phys.* **2004,** 42, (17), 3282-3289.
32. Li, Y.; Park, E. J.; Lim, K. T.; Johnston, K. P.; Green, P. F. *J. Polym. Sci. Part B. Polym. Phys.* **2007,** 45, (11), 1313-1324.
33. Koga, T.; Gin, P.; Endoh, H. Y. M.; Asada, M.; Sendogdular, L.; Kobayashi, M.; Takahara, A.; Akgun, B.; Satija, S. K.; Sumi, T. *Polymer* **2011,** 52, 4331.
34. Li, X.; Vogt, B. *Polymer* **2009,** 50, 4182.
35. Li, X.; Vogt, B. D. *J. Supercrit. Fluids* **2009,** 52, (2), 256-263.
36. Wang, X.; Sanchez, I. C. *Langmuir* **2006,** 22, 9251.
37. Sumi, T.; Sekino, H. *J. Chem. Phys.* **2005,** 122, 194910.
38. Sumi, T.; Imazaki, N.; Sekino, H. *Phys. Rev. E: Stat., Nonlinear, Soft Matter Phys.* **2009,** 79, 030801.
39. Makino, M.; Taniguchi, T.; Doi, M. *Proc. Int. Conf. Adv. Polym.* **2001**, 171.
40. Koga, T.; Seo, Y.-S.; Hu, X.; Shin, K.; Zhang, Y.; Rafailovich, M. H.; Sokolov, J. C.; Chu, B.; Satija, S. K. *Europhys. Lett.* **2002,** 60, (4), 559.
41. Koga, T.; Seo, Y. S.; Jerome, J.; Ge, S.; Rafailovich, M. H.; Sokolov, J. C.; Chu, B.; Seeck, O. H.; Tolan, M.; Kolb, R. *Appl. Phys. Lett.* **2003,** 83, 4309.
42. Russell, T. P. *Mater. Sci. Rep.* **1990,** 5, 171.
43. Huang, F. H.; Li, M. H.; Starling, K. E.; Chung, F. T. H. *J. Chem. Eng. Jpn.* **1985,** 18, 490-496.
44. Gin, P.; Asada, M.; Endoh, M. K.; Gedelian, C.; Lu, T.-M.; Koga, T. *Appl. Phys. Lett.* **2009,** 94, 121908.
45. Mackay, M. E.; Tuteja, A.; Duxbury, P. M.; Hawker, C. J.; Van Horn, B.; Guan, Z.; Chen, G.; Krishnan, R. S. *Science* **2006,** 311, 174-1743.
46. Segalman, R. A.; Green, P. F. *Macromolecules* **1999,** 32, (3), 801-807.
47. Zhang, W.; Bruce X. Fu, Y. S.; Eric Schrag, B. H.; Mather, P. T.; Yang, N.-L.; Xu, D.; Ade, H.; Rafailovich, M.; Sokolov, J. *Macromolecules* **2002,** 35, (21), 8029–8038.
48. Xavier, J. H.; Sharma, S.; Seo, Y. S.; Isseroff, R.; Koga, T.; White, H.; Ulman, A.; Shin, K.; Satija, S. K.; Sokolov, J.; Rafailovich, M. H. *Macromolecules* **2006,** 39, (8), 2972–2980.
49. Pham, J. Q.; Johnston, K. P.; Green, P. F. *J. Phys. Chem. B* **2004,** 108, (11), 3457–3461.
50. Pham, J. Q.; Sirard, S. M.; Johnston, K. P.; Green, P. F. *Phys. Rev. Lett.* **2003,** 91, 175503

51. Lee, J. Y.; Shou, Z.; Balaza, A. C. *Phys. Rev. Lett.* **2003,** 91, 136103.
52. Seeck, O. H.; Kaendler, I. D.; Tolan, M.; Shin, K.; Rafailovich, M. H.; Sokolov, J.; Kolb, R. *Appl. Phys. Lett.* **2000,** 76, 2713.
53. Findenegg, G. H., *In Fundamentals of Adsorption*. Engineering Foundation: New York, 1983.
54. Lal, M.; Plummer, M.; Richmond, N. J.; Smith, W. *J. Phys. Chem. B* **2004,** 108, (19), 6052–6061.
55. Lal, M.; Plummer, M.; Smith, W. *J. Phys. Chem. B* **2006,** 110, (42), 20879–20888.
56. Kim, J. U.; O'Shaughnessy, B. *Phys.Rev. Lett.* **2002,** 89, 238301.
57. Langmuir, I. *J. Chem. Phys.* **1933,** 1, 756.
58. P.R.Pujado; L.E.Scriven. *J. Colloid Interface Sci.* **1972,** 40, 82.

Chapter 3 Better Understanding of Interplay between Free Surface and Substrate Interface to Create Heterogeneous Crystalline Structures within Polymer Thin Films

3-1. Abstract

Order structures (single lamellar crystals stack towards the direction perpendicular to the chain-folded face and resultant repeated stacked lamellar domains propagate into three-dimensional spherocrystals) of semi-crystalline polymer thin films have large deviations from bulk. It is also predicted that local quantities within polymer thin films would be different from average ones, depending on the interplay between the air/polymer surface and the polymer/substrate interface. In Chapter 3, structures of semi-crystalline polymer thin films were separately evaluated in the direction to film normal in order to understand the interplay between both the interfaces, in particular, the role of the substrate-bound adsorbed polymer layer.

As a model system, the structural heterogeneity of melt crystallized linear low-density polyethylene (LLDPE) thin films (25, 50, and 100 nm in thickness (t)) in the direction normal to surface was systematically characterized by the comprehensive analyses using *in-situ* grazing incidence small angle x-ray scattering (GISAXS), x-ray diffraction (GID) and atomic force microscope (AFM) measurements. In this study I evaluated the melting behavior of the LLDPE thin films and focused on the origin of the heterogeneity of the structures.

The AFM and GID results have clarified the presence of the edge-on lamellae at the surfaces and in the interior of the LLDPE films prepared on Si substrates as thin as 25 nm in thickness. However, the degree of the crystallinity for the 25 nm thick film was almost half of those for the 50 and 100 nm thick films, while the melting temperature (T_m) for all the films remained unchanged relative to the bulk (T_m =117 °C). Moreover, the GISAXS results for the 25 nm thick film indicate the structural heterogeneity in the direction normal to the surface: (i) At the polymer/air interface, the presence of the disordered edge-on lamellae which lack well-defined long periods even at $T << T_m$; (ii) At the polymer/substrate interface, the persistence of a substrate-bound edge-on lamellar layer even at $T >> T_m$; (iii) In between the two interfacial layers, the existence of the well ordered edge-on lamellae with the long periods. The key for the structural heterogeneity is the emergence of the substrate-bound unmelted lamellar layer, which is observed regardless of film thickness. The heterogeneous structures in the 25 nm thick film can be rationalize as a consequence of the nucleation initiated at surface of the substrate-bound lamellar layer and the persistence of the heterogeneous crystal growth, while the nucleation takes place also at the topmost air/polymer surface in the films with $t > 50$ nm.

3-2. Introduction

Polymer thin films on solid substrates have been explored in a variety of industrial fields owing to their advantages including inexpensiveness, light-weight, flexibility, and facile fabrication of desired molecular architectures[1]. At the same time, the unusual properties of polymer thin films due to the effects of confinement, such as viscoelastic property, [2, 3] glass transition temperature (T_g), [4, 5] interdiffusion, [6, 7] and physical aging, [8] have been acknowledged from an academic point of view. There is growing evidence that the interplay between the polymer/air and polymer/substrate interfaces is crucial to understand the mechanism of the confinement effects[8, 9]. At the polymer/air interface, there exists a surface mobile layer[10-12] which enhances the chain dynamics. Previous studies showed that the rate of crystallization, crystal orientation, and density of nucleation sites for polymer thin films are quite different from the bulk[13-19]. In addition, grazing incidence x-ray diffraction experiments clarified that the lattice constants, crystallinity, the degree of paracrystalline lattice distortion, [20] and the crystallization kinetics[21] at the surface are quite different from those of the rest of the film. On the other hand, the substrate interface is known to reduce the dynamics because of an immobile polymer adsorbed layer[22-27] including semi-crystalline polymers[25, 26]. However, little is known about the effect of the substrate interface on local structures or properties within semi-crystalline polymer thin films. In addition, most previous work has revealed the deviations of "average" quantities of entire nanometer films from the bulks, the better understating of the local quantities within the film, which depends on the interplay between these interfaces, is necessary.

In this Chapter, I utilize a combination of *in-situ* grazing incidence small angle x-ray scattering (GISAXS) and x-ray diffraction (GID) with two different incident angles of x-ray beams to provide a better understanding of the local structures of melt crystallized polymer thin films. Spin-cast linear low-density polyethylene (LLDPE) thin films（25, 50, and 100 nm in thickness) prepared on cleaned hydrogen-passivated silicon (H-Si) substrates were used as the model system, because the crystalline structures and melting behavior in the bulk LLDPE have been well characterized. Furthermore, the combined use of transmission small-angle x-ray scattering (SAXS), transmission wide-angle x-ray scattering (WAXS), and differential scanning calorimetry (DSC) experiments for the bulk LLDPE resin enabled us to highlight the deviations of the melt crystallized structures of the ultrathin films and its melting behavior from the bulk. As a result, I found the presence of heterogeneous architectures within the 25 nm thick film in the direction normal to the surface: (i) At the polymer/air interface, there exist the disordered edge-on lamellae which lack a well-defined interlamellar spacing, so-called "long period", even at temperatures far below the bulk melting temperature (T_m); (ii) At the polymer/substrate interface, the polymer chains adsorb onto the substrate and the substrate-bound edge-on lamellar structures remain even at $T >> T_m$; (iii) In between the two interfacial layers, the polymer chains form the well-ordered edge-on lamellae and the melting behavior is governed by the sequential melting as seen in the bulk[28-30]. According to the previous results where polymer chains were quenched from the melt to a low crystallization temperature,[19] the nucleation was found to be triggered at the polymer/air interface due to the

surface mobile layer. However, it is not conclusive whether the surface mobile layer is present within a few tens of nanometer thick supported films[9]. Therefore, it is postulated that the melt crystallization is initiated from the substrate-bound lamellar layer as seeds, independently of the primary nucleation at the polymer/air interface. Furthermore, it is revealed that this substrate effect associated with the substrate-bound lamellar layer is limited to the region within 50 nm from the substrate interface for the present system.

3-3. Experimental Section

3-3-1. Sample Preparation

Linear low density polyethylene (LLDPE) was provided by ExxonMobil Corporation. Molecular weight (M_w) and polydispersity were 50,000 and 2, respectively. The melting temperature (T_m) was estimated to be 117 ºC by a differential scanning calorimeter. Si substrates were cleaned by immersion in a hot piranha solution (i.e., a mixture of H_2SO_4 and H_2O_2, *caution*: the piranha solution is highly *corrosive* upon contact with the skin or eyes and is an explosion hazard when mixed with organic chemicals/materials; Extreme care should be taken when handing it.) for 15 min, subsequently rinsed with purified water thoroughly, and followed by submersion in an aqueous solution of hydrogen fluoride to remove native oxide. Three different thin films with average thicknesses of 25 nm, 50 nm, and 100 nm were prepared by spin coating LLDPE/toluene solutions onto hydrogen-passivated Si substrates above 100 ºC. The details of the film preparation has been described elsewhere[17]. All samples were dried under vacuum at 150 ºC for 24 h to erase the memory of the sample preparation and then rapidly quenched to room temperature within 1 min in order to melt crystallize the films. The surface tension of the LLDPE is 30 mJ/m^2 [31]. The interfacial energy (γ) between the polymer and the substrate is then estimated to be $\gamma_{PE/Si}$= 6.2 mJ/m^2 based on the Owens-Wendt-Kaelble equation[32] with the dispersion part (48.71 mJ/m^2) and polar part (3.98 mJ/m^2) of the surface tension of Si[18]. Compared with $\gamma_{PS/Si}$=1.4 mJ/m^2 for the polystyrene/Si system or $\gamma_{PB/Si}$= 4.0 mJ/m^2 for the polybutadiene/Si system, the LLDPE film prepared on a Si substrate is categorized as a weakly attractive interacting system.

3-3-2. Ellipsometry

The average thickness of the melt crystallized LLDPE films was measured by the ellipsometer (AutoEL-II ellipsometry, Rudolf Research) equipped with a He-Ne laser (632 nm) by setting the index of refraction for LLDPE as 1.53.

3-3-3. Atomic Force Microscope (AFM)

Surface crystalline morphologies of the LLDPE thin films were observed by an atomic force microscope (AFM) (Seiko Instruments Inc., E-sweep). Dynamic force microscopic mode measurements were carried out under vacuum as to avoid the surface oxidation and a capillary force effect induced by surface-adsorbed water. As will be discussed later, the surface morphology of the substrate-bound adsorbed (residual) layer after an intensive washing process with toluene (a good solvent for LLDPE) was measured by a contact mode AFM (Dimension 3100, Digital Instruments).

3-3-4. Differential Scanning Calorimetry (DSC)

Melting behavior of the bulk LLDPE was characterized by a differential scanning calorimetry

(DSC, Perkin Elmer DSC 7) in a nitrogen atmosphere. Fig. 3-1 shows the DSC curve obtained at the heating rate of 5 ºC /min. From the figure, we can see that the melting starts at around 90 ºC and ends at 117 ºC. We also confirmed that the DSC curves obtained with different heating rates remain unchanged. The enthalpy of melting (ΔH_m) was calculated to be 80 J/g from the area of the DSC peak between 90 ºC and 117 ºC after the base line (indicated as the dotted line) subtraction. The degree of crystallinity (ϕ_b) in the bulk was then estimated to be 0.27 by using the following equation:

$$\phi_b = \frac{\Delta H_m}{\Delta H_{100}} \qquad (1)$$

where ΔH_{100} is the value of heat fusion for the 100% crystalline polymer. For this study, $\Delta H_{100} = 293 J/g$ was used[33]. We confirmed that the crystallinity is in good agreement with the one determined by WAXS experiments.

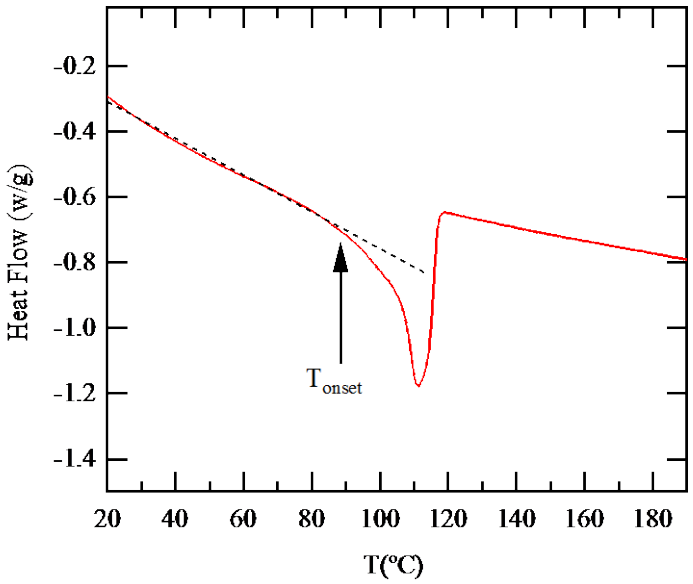

Fig. 3-1 Heat flow chart of the LLDPE resin at a heating rate of 5 °C/min.

3-3-5. Glazing Incidence Small Angle X-ray Scattering (GISAXS)

In-situ glazing incidence small angle x-ray scattering (GISAXS) study was conducted at the sector 8-ID beamline, Advanced Photon Source (APS, Argonne). The details have been described elsewhere[34]. The scattering from each sample was collected by a 2D MAR-CCD camera for an accumulation time of 10 s. Two-dimensional (2d) GISAXS profiles were obtained with successive heating and cooling temperature runs from room temperature (20 ºC) to 150 ºC after 30 min stabilization at each temperature. GISAXS measurements are advantageous for quantitatively

characterizing edge-on lamellae oriented in the direction perpendicular to the substrate surface (as schematically shown in Fig. 3-4(a)), while flat-on lamellae where the lamellar layers run parallel to the surface cannot be detected with this scattering geometry. In order to see the differences in the crystalline structures between the topmost surface and the rest of the film, the two different incident angles (α) were utilized: (i) α = 0.13 º, which is just below the critical angle (α_c) of the total external reflection for LLDPE (α_c = 0.16 º with an x-ray energy of 7.4 keV used in this study) such that the electric field intensity decays exponentially into the film and thereby scattering intensity is dominated by the surface area of about 9 nm depth; (ii) α =0.18 °, above α_c, where the x-ray penetration depth (~3 μm) exceeds the film thickness such that we can obtain information on average structures over the entire film. I denote the first experimental configuration as the "*surface-mode*" and the second one as the "*film-mode*" hereafter. Note that, as shown in Fig. 3-2, the surfaces of the LLDPE films at low temperatures may not be a "mirror" (the root-mean-square roughness values are approximately 4 nm for the 50 and 100 nm thick films and 2 nm for the 25 nm thick film, respectively) so that the x-ray beams may penetrate into the film interior more than 9 nm in depth. Nevertheless, as will be discussed later, the GISAXS profiles for the 25 nm thick film are quite different between the surface-mode and the film-mode. In addition, as the temperature increases, the degree of the crystallinity for all the films decreases and the resultant surfaces become more flattened. For these reasons, I conclude that the two modes are still able to differentiate the structures at the topmost surface and over the entire film. To prevent possible errors associated with the rough surface, analysis for the GISAXS and GID data was performed only at high temperatures (i.e., $T \geq 60$ °C).

3-3-6. Glazing Incidence X-ray Diffraction (GID)

In-situ glazing incidence x-ray diffraction (GID) measurements with the aforementioned two modes were performed at the beamline x22B at the National Synchrotron Light Source (NSLS, Upton) for acquiring 2d images with a CCD camera (Princeton Instruments). X-ray energy of 8.17 keV was used. High temperature GID experiments, up to 100 ºC, were performed by using a custom-built vacuum furnace with Be windows. In addition, one-dimensional (1d) profiles near the 110 Bragg reflections were measured as a function of temperature (up to 140 ºC) by using a scintillation counter (Oxford), scanning in the direction parallel to the sample surface (i.e., an in-plane configuration) at the sector 15-B beamline (APS).

3-3-7. Transmission SAXS and WAXS

The transmission wide angle x-ray scattering (WAXS) and small angle x-ray scattering (SAXS) experiments for the bulk resin were performed at the beamline x27C at the NSLS. A MAR CCD detector (Rayonix, L.L.C.) was used to obtain 2d images. The details of the experimental set-up have been described elsewhere[35]. Since both SAXS and WAXS scattering patterns were isotropic,

the scattering profiles were integrated over the azimuthal angle after corrections for air scattering and incident beam intensity fluctuations and converted into 1d profiles to further analyze the data. The degree of crystallinity (X_c) in the irradiated area of the LLDPE films was then estimated from the 1d WAXS profiles as follows:

$$X_c = \frac{\sum I_c(q)}{\sum I_c(q) + \sum I_a(q)} \tag{2}$$

where I_c and I_a are intensities from the crystalline and amorphous components at the scattering vector q ($= 4\pi \sin\theta / \lambda$, θ being half the scattering angle and λ the wavelength of x-rays) respectively. The values of these peaks were determined by the best-fits of the experimental profiles with the predicted profiles constructed by a weighted average of Lorentzian and Gaussian functions for the broad amorphous and sharp crystalline components, respectively.

3-4. Results and Discussion

3-4-1. Surface Structures

Before the LLDPE thin films were subject to the *in situ* x-ray scattering experiments, I first utilized AFM to characterize the surface structures. Fig. 3-2 (a) shows the AFM height image of the 100 nm thick film at room temperature (T = 25 ºC) where the bright and dark areas correspond to higher and lower heights at the surface, respectively. The sheaf-like morphology has been assigned to a crystalline lamellar structure oriented edge-on with respect to the film surface[17]. At around T = 80 ºC, the sheaf-like aggregates become more flattened (Fig. 3-2 (b)) and I could not capture the phase images at T > 90 ºC due to surface softening, which occurs near the bulk melting temperature (see Fig. 3-1). The surface morphologies of the 50 nm thick film are quite similar to those of the 100 nm thick film. As shown in Fig. 3-2 (c), similar sheaf-like aggregates can also be seen in the 25 nm thick film at room temperature, however, the stacked lamellar structures are less dense than those in the 50 and 100 nm thick films. In addition, the surface softening of the 25 nm thick film occurred at substantially lower temperatures, around 40 ºC (Fig. 3-2 (d)), and this prevented the phase imaging at higher temperatures. These AFM results suggest a significant decrease in the crystallinity and a change in the lamellar structures of the 25 nm thick film compared to those of the thicker films.

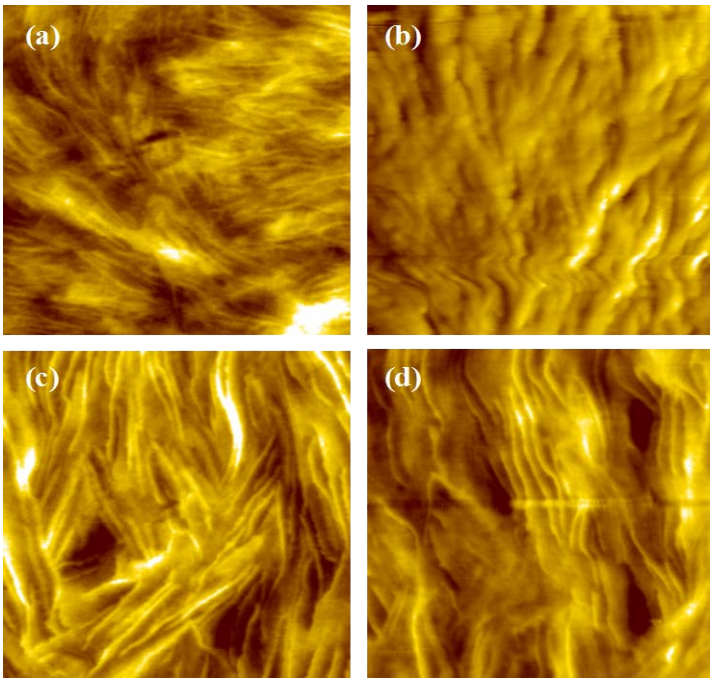

Fig. 3-2 Surface topographic crystalline morphology obtained by AFM measurements: (a) the 100 nm thick film at room temperature (T = 25 °C); (b) the 100 nm thick film at T = 80 °C; (c) the 25 nm thick film at room temperature; (d) the 25 nm thick film at T = 40 °C, respectively. The scan sizes and height scales for all the images are 1 μm × 1 μm and 0-20 nm, respectively.

Below, I show that the combined use of *in situ* GISAXS and GID techniques enabled us to quantitatively characterize the interior structures of the thin films and melting behavior at the surface and in the entire film independently. Note that the obtained surface structures would correspond to those characterized by the GISAXS and GID measurements (the surface-mode).

3-4-2. Assignment of Crystal Orientation

Before I show the *in situ* GID results of the melting, the crystal orientation in the thin films were determined based on the diffraction patterns. Fig. 3-3 shows representative GID results for the 25 nm thick films at room temperature. The 2d GID patterns are nearly identical between the surface-mode (Fig. 3-3 (a)) and the film-mode (Fig. 3-3 (b)). It was also confirmed that the same is true for the 50 and 100 nm thick films. I can index the two Bragg reflections at q =15.1 nm^{-1} and 16.3 nm^{-1} as 110 and 200, respectively, based on the known LLDPE orthorhombic crystal structure with the unit cell parameters: a = 7.4 Å, b = 4.93 Å, c = 2.53 Å[36]. In addition, the 200 reflection is located along the surface normal, while the 110 reflection is found at the off-axis position. This indicates that the LLDPE crystal structures are preferentially oriented with respect to the substrate. In order to determine the orientation (either edge-on or flat-on) of the crystal structures, the reflection patterns were simulated by assuming that the polymer chain axis was identical to the crystallographic *a*, *b* or *c*-axis, as schematically shown in Fig. 3-4 (a). The details of the simulations have been described elsewhere[37]. Comparisons between simulated patterns (Fig. 3-4 (b)) and the observed GID patterns led to the conclusion that the LLDPE chains form the edge-on lamellae with its crystallographic *c*-axis pointing along the direction parallel to the surface, as schematically shown in Fig. 3-4 (c). This is consistent with the AFM results (Fig. 3-2) where the surfaces of the films are mainly covered with the edge-on lamellar structures.

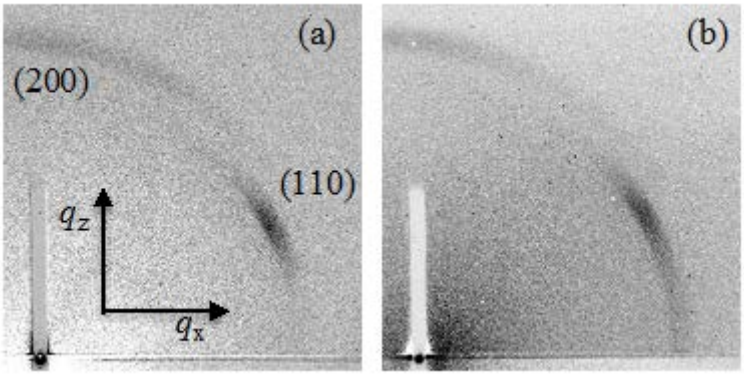

Fig. 3-3 Representative two-dimensional GID images for the 25 nm thick film at room temperature. (a) the surface-mode; (b) the film-mode. The specular reflection is shielded by a beam stop seen as the rectangular shape.

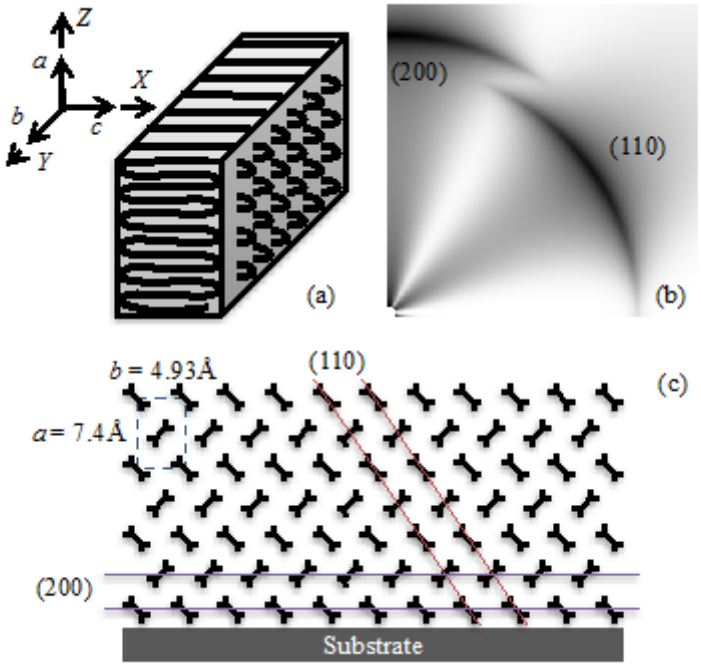

Fig. 3-4 (a) Crystal geometry (edge-on) in the film plane used for simulated diffraction pattern, (b) the resultant simulated diffraction pattern, and (c) the schematic crystal model viewed along the chain axis (the *c*-axis). Each symbol corresponds to the monomeric unit.

3-4-3. Melting Observation -GID measurements-

Fig. 3-5 shows the temperature dependences of the intensity (the film-mode) integrated near the 110 reflection peak position and normalized by the film thickness for the 25 and 50 nm thick films. The results for the 100 nm thick films are nearly identical to that for the 50 nm thick film. From the figure we can see that the thickness-normalized intensity for the 25 nm film is about half of the 50 nm thick film regardless of temperature. It is also important to point out that the intensities for the 25 and 50 nm thick films suddenly drop off at around T = 90 ºC and completely disappeared at the bulk T_m (=117 ºC) obtained from the DSC (Fig. 3-1) and WAXS experiments. Fig. 3-5 also shows that the temperature dependence of the bulk crystallinity determined by WAXS (indicated by the crosses) has the same trend as the intensity changes for the thick films. These observations demonstrate that the integrated intensity represent a direct measure of the crystallinity within the thin films. Thus, the GID results provide evidence that the onset of melting occurs at around 90 ºC for the thin films and that the crystallinity of the 25 nm thick film is considerably suppressed

relative to the 50 and 100 nm thick films. A series of the GID experiments also led to the conclusion that the melting temperatures at the topmost surface and of the entire film, as measured by the disappearance of the 110 and 200 peaks, remain essentially the same as the bulk T_m regardless of the film thicknesses. It should be noted that, as will be discussed later, there exists a very thin substrate-bound lamellar layer even at $T >> T_m$. I presume that the degree of crystallinity in the substrate-bound lamellar layer is very low so that the present GID experiments in the film-mode may not be sensitive enough to identify the layer.

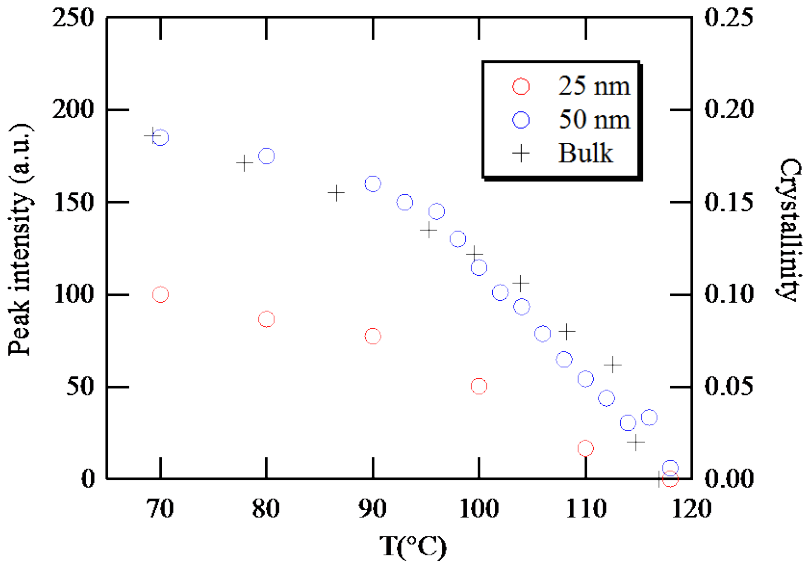

Fig. 3-5 Integrated intensity near the 100 Bragg reflection peak as a function of temperature for the 25 nm (red) and 50 nm (blue) thick films obtained by the GID results. The crystallinity of the bulk determined by WAXS is indicated as the black crosses.

3-4-4. Melting Observation -GISAXS measurements-

Next, I show the GISAXS results of the melting of the LLDPE thin films. Fig. 3-6 shows the temperature dependences of the GISAXS profiles for the 100 nm thick film in the surface-mode (Fig. 3-6 (a)) and the film-mode (Fig. 3-6 (b)) during the heating process. The 2d profiles were used to extract the 1d profiles of the intensity along the q_{xy}-direction at around $q_z = 0.1$ nm^{-1}, since the edge-on lamellar structures are the majority in the film interior. From these figures we can see the broad scattering maximum at around the in-plane scattering vector ($q_{//}$) of 0.4 nm^{-1} at $T < T_m$ in both the surface-mode and film-mode. The peak is attributed to the lamellar long period (L_p) of the edge-on lamellae. As the temperature increases, the peak position shifts to the lower q-region at $T \leq T_m$. At the same time, the weak broad shoulder (indicated by the arrow) is observed in the film-mode even at $T > T_m$, whereas the broad peak in the surface-mode disappears at the same

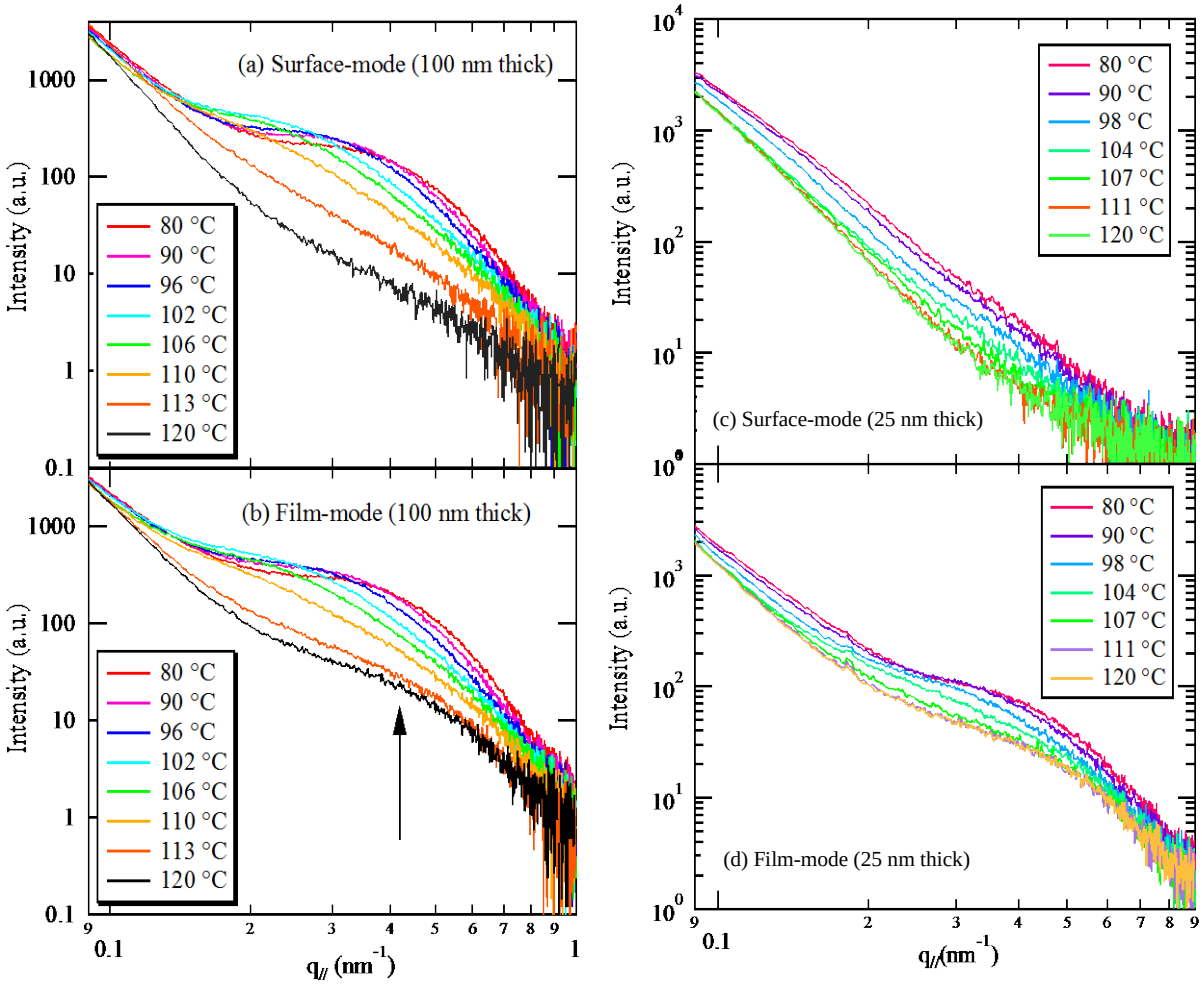

Fig. 3-6 GISAXS profiles for the LLDPE thin films with elevating temperature up to 120 °C. (a) the 100 nm thick film in thick in the surface-mode; (b) the 100 nm thick film in the film-mode; (c) the 25 nm thick film in the surface-mode; (d) the 25 nm thick film in the film-mode. The arrow indicates the presence of the weak broad shoulder even at $T > T_m$.

temperature range. This broad shoulder implies the persistence of an edge-on lamellar layer within the film even at $T > T_m$. It should be noted that the GISAXS profiles in the film-mode and surface-mode at 120 ºC < $T \leq$ 150 ºC are almost identical to the ones at T = 120 ºC. Further discussion about the substrate-bound lamellar layer will be presented later.

In order to calculate the long periods, the GISAXS data was analyzed in terms of a 1d model of stacked lamellar crystals separated by amorphous layers[38]. The normalized 1d correlation function can be obtained by the following equation:

$$\gamma(r) = \frac{\int_0^\infty I(s)s^2 \cos(2\pi rs)\,ds}{\int_0^\infty I(s)s^2\,ds} \qquad (4)$$

where s corresponds to the magnitude of $2\pi / q_{//}$ and r represents the distance in a real space. Before calculations of the correlation functions, several corrections including smoothing using spline functions to reduce the effect of noise and extrapolations to both low and high s values to extend the limited experimental s values were made[39]. Extrapolation to $s \to 0$ can be performed by the Debye-Bueche model[40]:

$$I(s) = \frac{C}{\left(1 + 4\pi^2 \xi^2 s^2\right)^2} \quad , \qquad (5)$$

where C is a constant and ξ is an inhomogeneity length. On the other hand, extensions of intensity to large s values could be achieved according to the Porod-Ruland model[41]:

$$\lim_{s \to 0} I(s) = P \frac{e^{-4\pi^2 \sigma^2 s^2}}{s^4} \qquad (6)$$

where P is the Porod constant and σ is the interfacial width between the crystalline and amorphous regions in lamellar stacks. Fig. 3-7 shows the temperature dependence of the long periods $L_p(T)$ for the 100 nm thick film in the film-mode obtained by the position of the first maximum of $\gamma(r)$. The temperature dependence of the long period in the surface-mode for the 100 nm thick film (data not shown) is exactly identical to that in the film-mode at $T \leq T_m$. From the figure we can see a slight increase in $L_p(T)$ up to $T \cong 80$ ºC from the original value (L_p^0) of 11.5 nm at room temperature (T = 25 ºC). A rapid increase in L_p is then observed above T = 90 ºC, which corresponds to the onset of the melting temperature. As shown in the inset, the values of $L_p(T)/L_p^0$ for the 100 nm thick film (indicated by triangles) are in good agreement with those for the bulk (indicated by crosses) obtained by SAXS. This strong increase in the long periods at $T \geq$ 90 ºC has been reported previously in bulk LLDPE and high density PE[39, 42, 43] and can be explained by the sequential melting (i.e., the melting of some randomly placed crystals within stacks, resulting in an increase in the average amorphous thickness[28-30]). Since the temperature dependence of L_p for the 50 nm thick film is consistent with that for the 100 nm thick film, it is conclude that the melting processes for the 50 nm and 100 nm thick films are governed by the sequential melting as for the bulk.

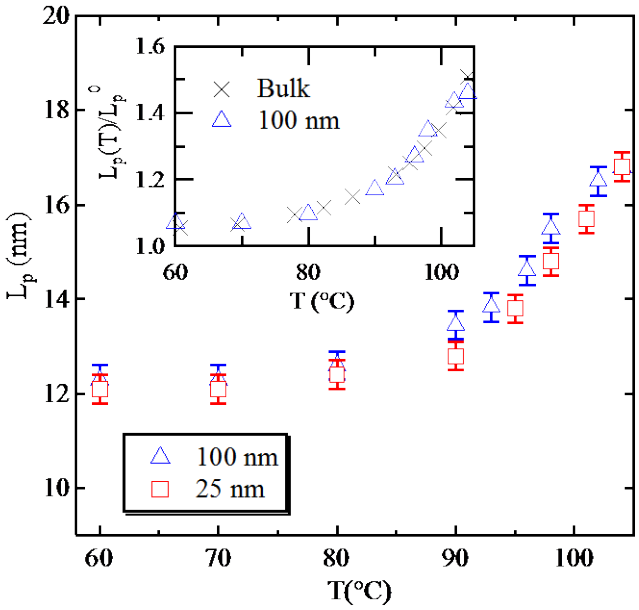

Fig. 3-7 Long periods (L_p) of the lamellar structure vs. temperature for the 25 and 100 nm thick films determined in the film-mode. The temperature dependence of L_P for the bulk resin is also plotted in the inset of the figure.

I now turn to the melting process for the 25 nm thick film where the significant decrease in the degree of the crystallinity is identified by GID. The GISAXS profiles in the surface-mode and film-mode are also shown in Fig. 3-6. The GISAXS profiles in the film-mode clearly show the broad scattering maximum corresponding to the long period of the edge-on lamellae at around $q_{//}$ = 0.4 nm^{-1} (Fig. 3-6 (d)). In addition, as indicated in Fig. 3-6 (b) for the 100 nm thick films, the broad shoulder persists even at $T \geq T_m$, demonstrating the presence of the substrate-bound lamellar layer in the 25 nm thick film as well. In contrast, as shown in Fig. 3-6 (c), there is no scattering peak in the surface-mode for the 25 nm thick film. In conjunction with the GID data and AFM images, the GISAXS data is consistent with the absence of the well-defined long periods at the surface of the 25 nm thick film. In order to provide further insight into the disordered edge-on lamellar structures at the surface, I used the Debye-Bueche (DB) analysis[40] (Eq. 5) with the assumption of a random two-phase system composed of a crystal region and amorphous region in the lamellar stack. Fig. 3-8 (a) shows representative $I(q_{//})^{-0.5}$ vs. $q_{//}^2$ plots at T = 90 ºC and 104 ºC for the 25 nm thick (surface-mode) film. From the slope (c_1) and intercept (c_2) at $q_{//}$= 0 in these plots, the correlation distances ($\xi = \sqrt{c_1 / c_2}$) were calculated. Fig. 3-8 (b) plots the temperature dependence of ξ obtained from the fits with the $q_{//}$-range of 0.27 < $q_{//}$ < 0.42 nm^{-1}.

From the figure we can see the similar trend of ξ to the long periods: at around T = 90 ºC, ξ starts to increase on raising temperature toward T_m. Judging from this behavior, I assume that ξcorresponds to the thickness of the amorphous region in the lamellar stack, even though the magnitude is smaller than that formed in the bulk film (10~15 nm in thickness estimated from the product of L_p and (1-X_c)). I also stress the deviation from the linear relationship of $I(q_{//})^{-0.5}$ vs. $q_{//}^2$ at the lower $q_{//}$ range ($q_{//}^2$ < 0.06 nm^{-2}), indicative of another larger heterogeneous structure with $\xi \sim 25$ nm based on the DB analysis. Since T_m at the surface of the 25 nm thick film remains unchanged relative to the bulk T_m, the thickness of the crystalline region in the lamellar stack, which is related to T_m (the Thomson-Gibbs equation[44, 45]), should be equivalent to that for the bulk film. Therefore, I assume that this larger ξ value also corresponds to the thickness of the amorphous region in the lamellar stack, indicating the presence of the in-plane heterogeneities in L_p at the surface of the 25 nm thick film.

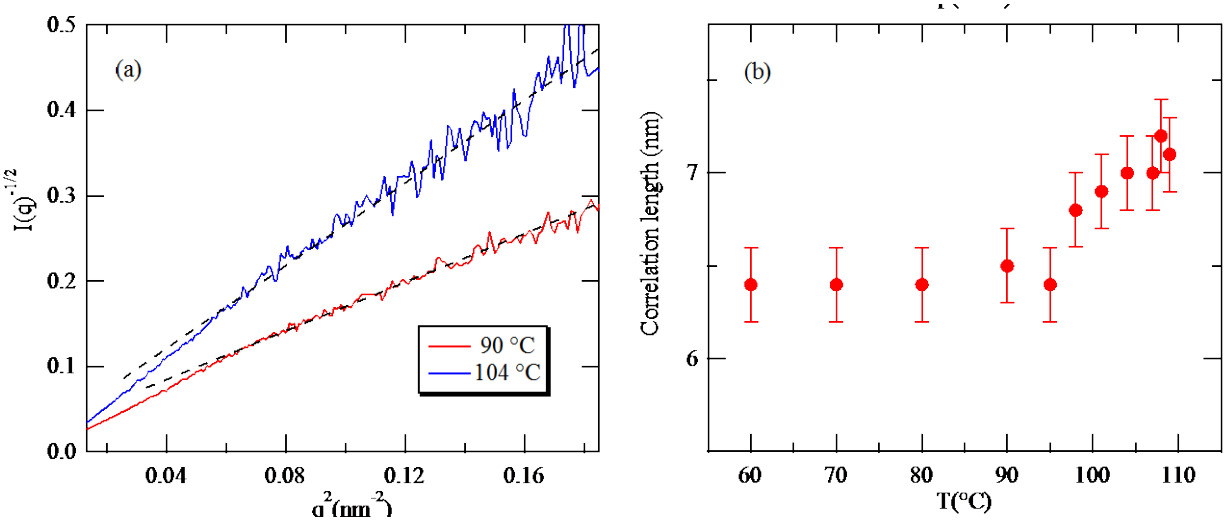

Fig. 3-8 (a) Representative DB plots for the 25 nm thick film (surface-mode) at T = 90 ºC and 107 ºC. (b) Temperature dependence of the correlation distances existing in the lamellar stack.

3-4-5. Structure of Substrate-Bound Edge-on Lamellar

From the GISAXS measurements it was indicated that the unmelted edge-on lamellar structure exist near the substrate interface. Furthermore, the key question is why the surface order including the crystallinity, the lamellar stacking, and the long periods are significantly reduced/or distorted

when the thickness of the LLDPE films is reduced to 25 nm. Below I address the question by clarifying the interior architecture of the 25 nm thick film in more detail.

Firstly, I focus on the buried structure near the substrate interface. For this purpose, the LLDPE films used for GISAXS experiments were washed at least 10 times (each washing was for approximately 30 min) in baths of fresh toluene at T = 90 °C, as shown in Fig. 1-10. After the washing process, the film was annealed the remaining layers at T = 150 ºC for 2 h to remove any excess solvent trapped in the layers and measured the thickness by using ellipsometry. As a result, I found the presence of a residual substrate-bound adsorbed layer of approximately 8 nm in thickness regardless of the original film thickness. Fig. 3-9 shows the surface height and phase lug images of the residual LLDPE layer obtained by using SFM. From the figure, we can see the string-like structures which resemble typical edge-on lamellar structures formed in ultrathin polymer films[19]. Hence, it is concluded that the adsorbed layer, which was not dissolved during the intensive washing process, is associated with the substrate-bound lamellar layer observed in the GISAXS profiles. However, the GISAXS measurements on the adsorbed layer (performed at the beamline BL03XU, SPring-8, Japan; the detail of the beamline has been described elsewhere[46]) do not show any broad shoulder, though the used undulator-based beam is brilliant. This suggests that the long-range order in the residual film is destroyed during the solvent washing, preventing quantitative characterization of the substrate-bound lamellar layer formed in the original spin-cast thin films. Hence, no further measurements on the substrate-bound lamellar layer were performed in the present study.

Although this preferential edge-on orientation of the lamellae at the Si substrate can be explained by the concept of minimization of the free energy during the primary nucleation step, [17, 47] its formation mechanism has not been clarified. I propose that the substrate-bound lamellae are formed during the spin-coating of the hot polymer/toluene solutions onto heated Si substrates at around 150 °C. This high temperature spin-coating was necessary to prevent the films from immediate crystallization on the substrates, which often causes dewetting[17]. The spin-cast films were then rapidly quenched to room temperature, inducing crystallization of the polymer chains within the entire film. Although I pre-annealed the films at 150 °C for 24 h to erase the memory of the sample preparation before melt crystallization, the GISAXS results prove that this is not sufficient to completely melt the lamellae formed near the substrate interface. Instead, the long high temperature pre-annealing may accelerate the growth of the adsorbed layer[23] and induce reorganization of the chain conformations deformed during the spin-coating process[48]. Since the structural relaxation of the polymer chains adsorbed onto solid substrates is typically very slow[49, 50], the structures/properties of the adsorbed layer are considered as “metastable” states with extremely long lifetime[23]. Hence, it is supposed that the substrate-bound lamellar structure is also attributed to the metastable conformations associated with the reduced chain mobility.

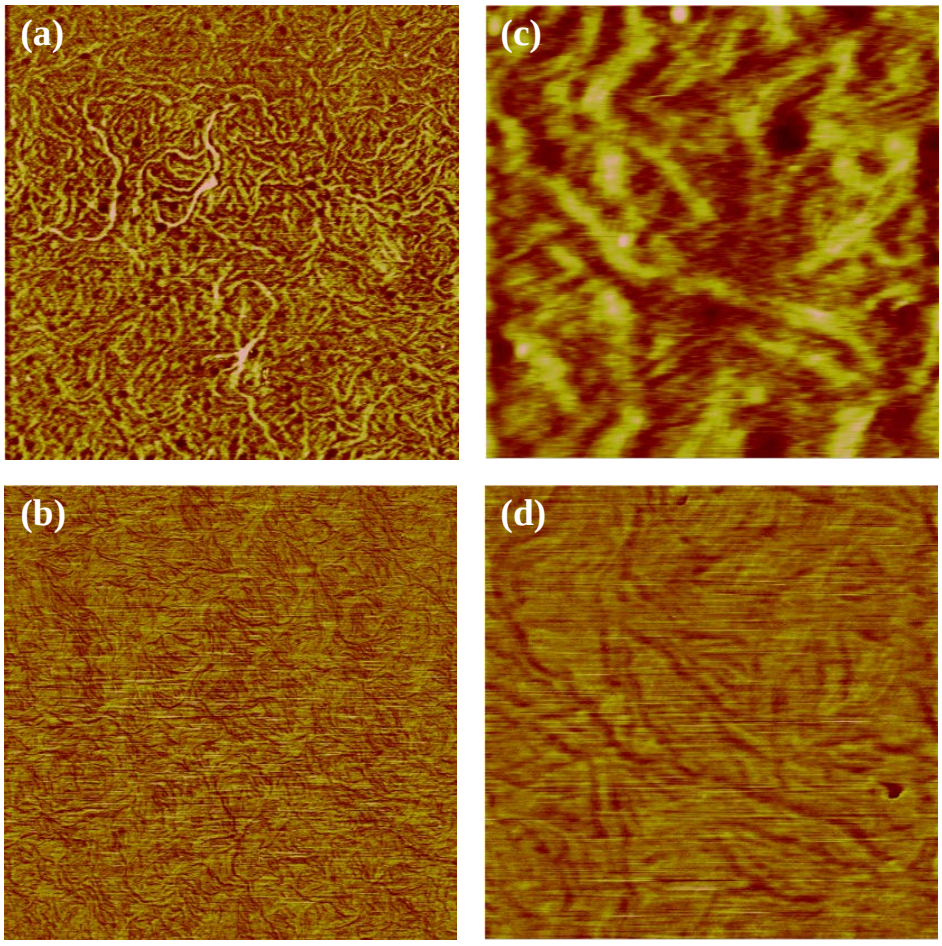

Fig. 3-9 AFM results of the residual LLDPE film at room temperature. (a) and (c) are the height images and (b) and (d) are the phase lug images. The image size is 5 μm × 5 μm for (a) and (b), and 1 μm × 1 μm for (c) and (d). The height scale for (a) and (c) is 0-20 nm.

3-4-6. Origin of Heterogeneous Structures in 25-nm Thick Film

By combining the obtained experimental findings, now I explore the interior architecture of the 25 nm thick film. Assuming that the scattering profile from the substrate-bound lamellar layer remains unchanged with changing temperature during the GISAXS experiments, the scattering profile at T =150 °C as additional background was subtracted from the observed GISAXS profiles in the film-mode. Fig. 3-10 shows the film-mode GISAXS profiles after this subtraction. From the figure it is clear that the shoulder-like scattering feature, which originates from the interior region between the two interfacial regions, shifts to the lower q-region upon approaching T_m. Interestingly, the long periods at $T \geq 60$ °C obtained by using eq. 4 are in good agreement with those of the 50 nm and 100 nm thick, as plotted together in Fig. 3-7. This implies that the 25 nm thick film's interior region still shows the bulk-like (sequential) melting behavior, in sharp contrast to the behavior of

the substrate-bound lamellar layer. Hence, the GISAXS results elucidate that the structures of the 25 nm thick film are quite heterogeneous in the direction normal to the surface.

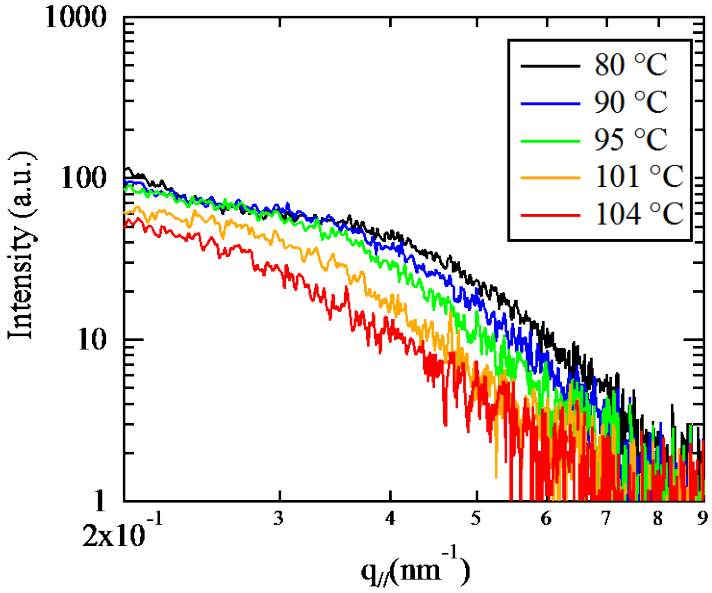

Fig. 3-10 GISAXS profiles in the film-mode for the 25 nm thick film after subtraction of the scattering intensity at T = 150 ºC.

These results provide insight into the formation process of the heterogeneous structures within the 25 nm thick film. According to the previous results where polymer chains were quenched from the melt to a low crystallization temperature, [19] the nucleation was found to be triggered at the polymer/air interface due to the surface mobile layer. However, it is not conclusive yet whether the surface mobile layer is present within a few tens of nanometer thick films prepared on solid substrates[9]. Instead, the present results indicate that the polymer/substrate interface plays a vital role in inducing the heterogeneous structures. It is known that there exists the so-called “reduced mobility interface (RMI) layer”[51, 52] in which the polymer chains are entangled with the adsorbed layer and act as a “transition zone” ensuring continuity in the mobility profile from the substrate to the bulk through chain entanglements[35]. Napolitano et al. reported that the RMI layer of poly(ethylene terephthalate) thin films prepared on aluminum substrates is about 20 nm in thickness[25]. Noting that the extent of the RMI layer should depend on the strength of the substrate interaction and the flexibility of polymer chains, it is reasonable to suppose that the part or whole of the interior region of the 25 nm thick LLDPE film corresponds to the transition zone. It is therefore postulated that the melt crystallization is initiated from the substrate-bound lamellar layer as seeds, independently of the primary nucleation at the polymer/air interface. The polymer chains in the

transition zone would then form the edge-on lamellae with the same orientation as for the substrate-bound lamellar layer in order to maximize the contacts, thereby stabilizing the interface[53]. Consequently, the surface disordering is attributed to the substrate effect induced by the substrate-bound lamellar layer. In fact, it is found that the melt crystallized structures and melting behavior at the surfaces of the 50 nm and 100 nm thick films recover to bulk (thick film)-like due to the effect of the surface mobile layer,[19] while the substrate-bound lamellar layer is found to be formed regardless of the film thickness. Hence, I conclude that this substrate effect is limited to the region within 50 nm from the substrate interface. Investigating to find the critical thickness, above which the bulk behavior is recovered, for different polymer/substrate systems should be conducted, in order to elucidate the correlation between the critical thickness and the strength of the interactions, the flexibility of the polymer chains, or the size of polymer chains. In Chapter 4, I will present the case of poly (ethylene oxide)/Si system where the interaction between the polymer and the substrate is strong. It is also worth studying a reorganization process of polymer chains in the crystalline state that occurs even after growth of crystalline structures[54, 55] so as to answer the question of why such constrained polymer chains in the transition zone form the well-ordered lamellae during the rapid melt crystallization process.

The present results differ from the previous reports[17, 18] which showed the presence of the flat-on lamellae at the surface of the 25 nm LLDPE thick film with the melting temperature of approximately 30 ºC lower than the bulk T_m. I believe that these apparent inconsistencies are mainly due to the difference in the melt crystallization process. It was reported that when the thickness of semi-crystalline polymer thin films is less than 30 nm, the formation of edge-on lamellae is preferred at lower crystallization temperature close to T_g of the polymer, while flat-on lamellae become dominant at higher crystallization temperatures closer to bulk T_m[47]. In the present study, the LLDPE films were quenched from 150 °C to room temperature within 1 min, while Wang and co-workers crystallized their LLDPE thin films by slowly quenching from 140 °C to room temperature over a period of 12 h[17] such that their crystallization temperature should be closer to the bulk T_m. In addition, the annealing times at the high temperature before melt crystallization, which are crucial for the formation of the adsorbed layer at the substrate interface,[23] are also quite different: 24 h for the present case and 0.5 h for the Wang and co-worker's experiments. As described above, since the adsorption process is typically very slow (several hours) for long polymer chains,[23] the resultant structure of the adsorbed LLDPE layer formed in Wang and co-workers' work may be quite different from that found in the present study. This may cause different substrate effects on the melt crystallized structures for very thin (a few tens of nanometers or less in thickness) semi-crystalline polymer films. Further systematic studies are necessary to clarify this point.

3-5. Conclusion

In this chapter, I reported the heterogeneous structures of polyethylene thin films and its thickness dependence. The focused point was that the local quantities within the thin films normal to film surface against the average ones, associated with the interplay between the polymer/air surface and the polymer/substrate interface. In particular, the role of the substrate-bound adsorbed polymer layer was highlighted.

By using comprehensive analyses such as the AFM measurements and the *in situ* GISAXS/GID techniques, I have investigated the melt crystallized structures of the LLDPE films with the three different thicknesses (25, 50 and 100 nm) prepared on clean hydrogen-passivated silicon substrates. The melting behavior was observed to deduce the interior structures of the films. In order to elucidate the heterogeneity of the melt crystallized structures in the direction normal to the surface, the two modes (the surface-mode and film-mode) with the different incident angles of x-ray beams were used for both GID and GISAXS. The GID results have revealed the presence of the edge-on lamellae at the surfaces and in the interior of the LLDPE films as thin as 25 nm in thickness. It was also found that the degree of the crystallinity for the 25 nm thick film is almost half of those for the 50 and 100 nm thick films. The GISAXS results support that the melting process at the surfaces and in the interior of the LLDPE films as thin as 25 nm in thickness is governed by the sequential melting as seen in the bulk[28-30]. At the same time, the GISAXS results indicate the presence of the substrate-bound edge-on lamellar layer which persists at least up to T = 150 °C >> T_m (= 117 °C), regardless of the film thickness. Intensive washing of the films with toluene uncovered the presence of the very thin (about 10 nm in thickness) residual edge-on lamellar layer, which is likely the origin of the substrate-bound lamellar layer. Moreover, the GISAXS results indicate the loss of the long periods at the topmost surface of the 25 nm thick film at T << T_m, while the intermediate region (i.e., the transition zone) between the topmost surface and substrate-bound lamellar layer shows the well-ordered lamellar structures. These heterogeneous structures of the 25 nm thick film can be explained as a consequence of the nucleation initiated from the substrate-bound lamellar surface, independently of the primary nucleation at the polymer/air interface[19]. The systematic GID and GISAXS results have clarified that the heterogeneous structures induced by the substrate-bound lamellar layer exist within the region of 50 nm in thickness from the substrate interface. Since the formation of both the adsorbed layer and the transition zone near the substrate interface occurs irrespective of polymer/substrate interactions and flexibility of polymer chains,[9, 22-27] the heterogeneous structures discovered in the present study (i.e., for the weakly interacting system) would be likely general and hence crucial for manipulating the properties of ultrathin semi-crystalline polymer films.

3-6. References

1. Hamley, I. W. *Prog. Polym. Sci.* **2009,** 34, (11), 1161-1210.
2. Hu, H. W.; Granick, S. *Science* **1992,** 258, 1339-1342.
3. Bodiguel, H.; Fretigny, C. *Phys. Rev. Lett.* **2006,** 97, 266105.
4. Ellison, C. J.; Torkelson, J. M. *Nature Mater.* **2003,** 2, 695-700.
5. Fakhraai, Z.; Forrest, J. A. *Phys. Rev. Lett.* **2005,** 95, 025701.
6. Zheng, X.; Rafailovich, M. H.; Sokolov, J.; Strzhemechny, Y.; Schwarz, S. A.; Sauer, B., B.; Rubinstein, M. *Phys. Rev. Lett.* **1997,** 79, 241-244.
7. Li, C.; Kim, H.; Jiang, J.; Li, C.; Koga, T.; Lurio, L. B.; Schwarz, S.; Narayanan, S.; Lee, H.; Lee, Y.-J.; Jiang, J.; Sinha, S. K.; Rafailovich, M. H.; Sokolov, J. C. *Europhys. Lett.* **2006,** 73, 899-905.
8. Priestley, R. D.; Ellison, C.; Broadbelt, L. J.; Torkelson, J. M. *Science* **2005,** 309, 456-459.
9. Koga, T.; Jiang, N.; Gin, P.; Endoh, M. K.; Narayanan, S.; Lurio, L. B.; Sinha, S. K. *Phys. Rev. Lett.* **2011,** 107, (22), 225901.
10. Fakhraai, Z.; Forrest, J. A. *Science* **2008,** 319, 600-604.
11. Yang, Z.; Fujii, Y.; Lee, F. K.; Lam, C.-H.; Tsui, O. *Science* **2010,** 328, 1676-1679.
12. Koga, T.; Li, C.; Endoh, M.; Koo, J.; Rafailovich, M. H.; Narayanan, S.; Lee, D. R.; Lurio, L.; Sinha, S. K. *Phys. Rev. Lett.* **2010,** 104, 066101.
13. Frank, C. W.; Despotopoulou, M. M.; Pease, R. F. W.; Hinsberg, W. D.; Miller, R. D.; Rabolt, J. F. *Science* **1996,** 273, 912.
14. Reiter, G.; Sommer, J. U. *J. Chem. Phys.* **2000,** 112, 4376.
15. Cho, K.; Kim, D.; Yoon, S. *Macromolecules* **2003,** 36, 7652.
16. Schönherr, H.; Frank, C. W. *Macromolecules* **2003,** 36, 1199-1208.
17. Wang, Y.; Ge, S.; Rafailovich, M.; Sokolov, J.; Zou, Y.; Ade, H.; ning, J. L.; Lustiger, A.; Maron, G. *Macromolecules* **2004,** 37, 3319-3327.
18. Wang, Y.; Rafailovich, M.; Sokolov, J.; Gersappe, D.; Araki, T.; Zou, Y.; Kilcoyne, A. D. L.; Ade, H.; Marom, G.; Lustiger, A. *Phys. Rev. Lett.* **2006,** 96, 028303.
19. Wang, Y.; Chan, C.-M.; Ng, K.-M.; Li, L. *Macromolecules* **2008,** 41, 2548-2553.
20. Yakabe, H.; Sasaki, S.; Sakata, O.; Takahara, A.; Kajiyama, T. *macromolecules* **2003,** 36, 5905–5907.
21. Jukes, P. C.; Das, A.; Durell, M.; Trolley, D.; Higgins, A. M.; Geoghegan, M.; Macdonald, J. E.; Jones, R. A. L.; Brown, S.; Thompson, P. *Macromolecules* **2005,** 38, 2315-2320.
22. Napolitano, S.; Pilleri, A.; Rolla, P.; Wubbenhorst, M. *ACS Nano* **2010,** 4, 841-848.
23. Napolitano, S.; Wubbenhorst, M. *Nature Commun.* **2011,** 2, 260-266.
24. Napolitano, S.; Wübbenhorst, M. *J. Phys. Chem. B* **2007,** 111, 9197-9199.
25. Napolitano, S.; Prevosto, D.; Lucchesi, M.; Pingue, P.; D'Acunto, M.; Rolla, P. *Langmuir* **2007,** 23, 2103-2109.
26. Lan, Q.; Yu, J.; Zhang, J.; He, J. *Macromolecules* **2011,** 44, 5743-5749.
27. Fujii, Y.; Yang, Z. H.; Leach, J.; Atarashi, H.; Tanaka, K.; Tsui, O. K. C. *Macromolecules*

2009, 42, (19), 7418-7422.
28. Belbeoch, B.; Guinier, A. *Makromol. Chem.* **1959,** 31, 1.
29. Crist, B. *Macromolecules* **2003,** 36, 4880-4890.
30. Crist, B. *J. Polym. Sci. B: Polym. Phys.* **2001,** 39, 2454-2460.
31. Wu, S. *J. Macromol. Sci. Part C* **1974,** 10, 1.
32. Kwok, D. Y.; Neumann, A. W. *Adv. Colloid Interac.* **1999,** 81, 167-249.
33. Hamada, F.; Wunderlich, B.; Sumida, T.; Hayashi, S.; Nakajima, A. *J. Phys. Chem.* **1968,** 72, (1), 178-185.
34. Khanna, V.; Cochran, E. W.; Hexemer, A.; Stein, G. E.; Fredrickson, G. H.; Kramer, E. J.; Li, X.; Wang, J.; Hahn, S. F. *Macromolecules* **2006,** 39, 9346-9356.
35. Wu, W. L.; Wallace, W. E.; van Zanten, J. H.; Bauer, B. J.; Liu, D. W.; Wong, A. *Polymer* **1997,** 38, 2583.
36. Tashiro, K.; Ishino, K.; Ohta, T. *Polymer* **1999,** 40, 3469-3478.
37. Chen, X.; Christian, C.; Ruan, D.; Zhang, L.; Hsiao, B. S.; Chu, B. *Polymer* **2006,** 47, 2839-2848.
38. Vonk, C. G.; Kortleve, G. *Kolloid-Z. Z. Polym.* **1967,** 220, 19.
39. Slusarczyk, C. *J. Alloys & Compounds* **2004,** 382, 68-74.
40. Debye, P.; Bueche, A. M. *J. Appl. Phys.* **1949,** 20, 518-525.
41. Ruland, W. *J. Pppl. Cryst.* **1971,** 4, (1), 70-73.
42. Nam, J. Y.; Kadomatsu, S.; Saito, H.; Inoue, T. *Polymer* **2002,** 43, 2101-2107.
43. Albrecht, T.; Strobl, G. *Macromolecules* **1995,** 28, 5827-5833.
44. Wunderlich, B., *Macromolecular Physics*. Academic Press:: New York, 1973.
45. Mandelkern, L., *Crystallization of Polymers*. McGraw-Hill: New York, 1984.
46. Masunaga, H.; Ogawa, H.; Takano, T.; Sasaki, S.; Goto, S.; Tanaka, T.; Seike, T.; Takahashi, S.; Takeshita, K.; Nariyama, N.; Ohashi, H.; Ohata, T.; Furukawa, Y.; Matsushita, T.; Ishizawa, Y.; Yagi, N.; Takata, M.; Kitamura, H.; Sakurai, K.; Tashiro, K.; Takahara, A.; Amamiya, Y.; Horie, K.; Takenaka, M.; Kanaya, T.; Jinnai, H.; Okuda, H.; Akiba, I.; Takahashi, I.; Yamamoto, K.; Hikosaka, M.; Sakurai, S.; Shinohara, Y.; Okada, A.; Sugihara, Y. *Polym. J.* **2011,** 43, 471-477.
47. Yang, J. P.; Liao, Q.; Zhou, J. J.; Jiang, X.; Wang, X. H.; Zhang, Y.; Jiang, S. D.; Yan, S. K.; Li, L. *Macromolecules* **2011,** 44, (9), 3511-3516.
48. Thomas, K. R.; Chenneviere, A.; Reiter, G.; Steiner, U. *Phys. Rev. E* **2011,** 83, 021804.
49. Barbero, D. R.; Steiner, U. *Phys. Rev. Lett.* **2009,** 102, 248303.
50. Metin, B.; Blum, F. D. *J. Chem. Phys.* **2006,** 125, 054707.
51. Wallace, W. E.; van Zanten, J. H.; Wu, W. L. *Phys. Rev. E* **1995,** 52, R3329-3332.
52. van Zanten, J. H.; Wallace, W. E.; Wu, W. L. *Phys. Rev. E* **1996,** 53, R2053-2056.
53. Zhang, F.; Baralia, G. G.; Nysten, B.; Jonas, A. M. *Macromolecules* **2011,** 44, 7752-7757.
54. Reiter, G. *J. Polym. Sci. Part B. Polym. Phys.* **2003,** 41, 1869-1877.
55. Sommer, J.-U.; Reiter, G. *Europhys. Lett.* **2001,** 56, 755-761.

Chapter 4 Investigation of Mechanism of $ScCO_2$-assisted Melt Crystallization and Role of Substrate-bound Adsorbed Polymer Layer

4-1. Abstract

In this chapter, the $scCO_2$-assisted melt crystallization was applied to poly (ethylene oxide) (PEO) thin films and the effect of CO_2 annealing on the melting and the crystallization behavior were investigated. The spin cast PEO thin films with different thickness were prepared on Si substrate as a model. The *In-situ* NR measurements showed that the PEO thin films were melted at 2.9 MPa and 48 ºC. The films were then subject to quick depressurization to atmospheric pressure. The resultant non-equilibrium swollen PEO melt/CO_2 films were quickly transferred to a temperature-controlled chamber to crystallize at given crystallization temperature (T_c). All the melt crystallize PEO thin films were then characterized by the glazing incidence x-ray diffraction (GID), atomic force microscope (AFM) and polarized optical microscope (POM) measurements.

The obtained GID and AFM results revealed the flat-on lamellar structures (molecular chains stand normal to the film surface) in all the PEO thin films, regardless of the original film thickness and T_c. Compared with the control PEO films prepared via the isothermal melt crystallization, the flat-on lamellar growth, which can heterogeneously initiate from an attractive interface, is much more enhanced. Furthermore, the dewetting kinetics for the 20 nm thick film is much slower than that of the thicker films. The key of these phenomena is that the limited CO_2 sorption at the substrate interface rather promotes the formation of the substrate-bound adsorbed layer on the substrate wall than the melting of the crystalline structures, due to the hindered chain mobility.

It is suggested that the flat-on lamellar growth from the adsorbed PEO layer persists up to film interior via the chain entanglements, while that from the topmost CO_2/polymer surface of the films is strongly retarded due to the strong plasticization effect. The $scCO_2$-assisted melt crystallization hence enables one to manipulate the heterogeneous structures of the semi-crystalline polymer thin films, in particular, illuminating the vital role of the substrate-bound adsorbed polymer layer.

4-2. Introduction

It is known that hierarchical morphologies of semi-crystalline polymers at different length-scales (i.e., a well-ordered crystalline state, a long-range-correlated repeated lamellar stacking grain, and a subsequent two or three dimensionally propagated spherocrystal) play crucial roles in mechanical properties, transport characteristics, and optical features of the bulks[1]. Owing to emerging advanced technologies, such as organic photovoltaics,[2] organic transistors,[3] and organic lightemitting diodes,[4] a challenge is to manipulate such crystalline morphologies within spatially confined polymer films where the rate of crystallization, crystal orientation, and density of nucleation sites are quite different from the bulks[5-12]. The main reason for these deviations is the interplay between two interfaces: the polymer/air interface and polymer/substrate interface[13]. For instance, the crystallization kinetics at the topmost polymer surface is quite faster than that of the rest of the film[14]. This is mainly attributed to the presence of the "surface mobile layer"[15-17] or the "surface reduced viscosity layer"[18, 19] where the glass transition temperature (T_g) or viscosity is much lower than the bulks or film interior. On the other hand, the chain dynamics near the substrate/polymer interface is retarded by the formation of semi-crystalline polymer adsorbed layers[20-23] at the polymer melt-substrate interface. It is proposed that these opposing effects then propagate into the film interior through chain entanglements,[24] resulting in heterogeneities in the crystalline structures within polymer thin films[12, 22]. However, the comprehensive understanding of the crystallization process in nanoconfined geometries is still lacking.

In Chapter 4, by using compressed CO_2 gas (T_c = 31.3 °C and P_c = 7.38 MPa), I aim to explore the melt crystallization and dewetting processes from the non-equilibrium swollen amorphous state under nanoconfinement. It is known that sorption of CO_2 molecules into polymers plays a role as a diluent or plasticizer for glassy/semi-crystalline polymers, lowering T_g and melting temperature (T_m) significantly and hence enhancing the chain mobility[25-28]. Especially, it was previously reported that the excess sorption of CO_2 molecules near the critical point of CO_2 takes place at the free surface as well as the substrate interface, resulting in the excess swelling of supported polymer thin films regardless of a choice of polymers[29-37]. So far, the detailed mechanism considering both the CO_2 sorption and nanoconfinement effects has yet to be rationalized. To achieve our objective, I choose poly (ethylene oxide) (PEO) ultrathin films spun cast on Si substrates as a model since the melting/crystallization behavior in CO_2 has been well characterized in bulk[38, 39] as well as thin films[34]. Firstly, high-pressure neutron reflectivity experiments were performed to investigate the plasticization effect of CO_2 on the PEO ultrathin films. The results indicate that the CO_2 induced the transition from the crystalline state to the amorphous state at a pressure as low as P = 2.9 MPa and at T = 48 °C which is below the bulk T_m. Subsequent rapid quench to atmospheric pressure allows us to create the non-equilibrium swollen state of the exposed PEO films. The polymer films were then transferred to a temperature-controlled stage (set temperatures ranging from 10 °C to 60 °C), permitting us to study the melt crystallization or dewetting process toward equilibrium at the given temperatures. The structural developments were characterized by using various surface sensitive experimental techniques including x-ray reflectivity, grazing incidence X-ray diffraction, polarized

optical microscopy, and atomic force microscopy. At last, I will discuss the formation of the adsorbed layer on the substrate via the CO_2 annealing, which plays crucial roles in the observed melt crystallization and dewetting processes.

4-3. Experimental Section

4-3-1. Sample Preparation

Poly (ethylene oxide) (PEO, average M_n = 20,000) was purchased from Sigma-Aldrich and used without any further purification. The bulk melting temperature (T_m) of PEO was determined to be 64 °C by differential scanning calorimetry (DSC) (Perkin Elmer DSC 7). Si substrates were cleaned by immersion in a hot piranha solution (i.e., a mixture of H_2SO_4 and H_2O_2, *caution*: the *piranha solution* is highly *corrosive* upon contact with the skin or eyes and is an explosion hazard when mixed with organic chemicals/materials; Extreme care should be taken when handing it.) for 15 min, subsequently rinsed with purified water thoroughly, and followed by submersion in an aqueous solution of hydrogen fluoride to remove native oxide. As will be discussed later, the SiO_2 layer of about 1 nm in thickness was reproduced even after hydrofluoric acid etching due to atmospheric oxygen and moisture, as reported previously[40]. PEO thin films with average thicknesses of 20, 50, and 100 nm were prepared by spin coating PEO/toluene solutions onto H-Si substrates with a rotation speed of 2500 rpm. The thickness of the spin-cast PEO thin films was measured by an ellipsometer (Rudolf Auto EL-II) with the fixed refractive index of 1.455. The surface tension of PEO is 42.9 mJ/m^2 (the dispersion part is 30.9 mJ/m^2 and the polar part is 12.0 mJ/m^2). The interfacial energy (γ) between the polymer and the substrate is then estimated to be 2.7 mJ/m^2 based on the Owens-Wendt-Kaelble equation[41], with the dispersion part (48.71 mJ/m^2) and polar part (3.98 mJ/m^2) of the surface tension of bare Si[11], assuming that the effect of the very thin SiO_2 layer is negligible. The PEO/Si system is thus categorized as an attractive interacting system. All the spin-cast films were dried under vacuum at 25 °C for 2 h before the CO_2 processing and directly placed into the high-pressure cell, preventing the prepared PEO thin films from swelling water in air. Note that this drying condition is not long enough to equilibrate the adsorption process (i.e., the time of the adsorption defined for PEO at 25 °C is at least 2 months).

4-3-2. *In-situ* Neutron Reflectivity

With a large penetration depth, neutron reflectivity (NR) is an ideal tool to determine the *in situ* thickness, composition, and interfacial structure of polymer thin films immersed in fluids or gases, under high pressure in thick walled vessels[32, 42]. The *in-situ* swelling behavior of the PEO thin films in CO_2 was measured by using neutron reflectivity (NR). Deuterated PEO (d-PEO, M_w = 21,400, M_w/M_n = 1.09, Polymer Source Inc.) was used to enhance the scattering contrast. The d-PEO thin films with the average thickness of 16, 28 and 78 nm were prepared on 3-inch H-Si wafers. The specular NR measurements were performed at the NG-7 reflectometry, the National Institute of Standards and Technology Center for Neutron Research. The wavelength (λ_N) of the neutron beams was 0.47 nm with $\Delta\lambda_N/\lambda_N$ = 2.5 %. The details of the high-pressure NR experiments and high-pressure cell have been described elsewhere[32]. The NR experiments were conducted under the isothermal condition (T = 48 °C) with elevated pressures up to P = 17.5 MPa. Temperature and pressure stabilities during the NR measurements were within an accuracy of ± 0.1°C and ± 0.2 %,

respectively. The d-PEO thin films were exposed to CO_2 for up to 4 h prior to data acquisition to ensure the equilibrium swelling. The scattering length density (SLD) values of CO_2, which vary from 0.0004×10^{-4} to 2.5×10^{-4} nm^{-2} in the pressure range of $0.1 < P < 17.5$ MPa at $T = 48$ °C, were calculated based on the density of CO_2 obtained by the equation of state[43]. The NR data was obtained by successively increasing the pressure and then slowly decreasing the pressure. Since the background scattering from a pure CO_2 phase increases dramatically near the critical point[30, 32], I measured the scattering from the pure fluid phase (i.e., the long-range density fluctuations) for each pressure condition. The NR data corrected for the background scattering was analyzed by comparing the observed reflectivity curves with the calculated ones based on model SLD profiles having three fitting parameters for each layer: film thickness, SLD, and roughness between the CO_2 and polymer layers represented as a Gaussian function[44]. The SLD profiles were subsequently converted into the corresponding polymer volume fraction profiles. Assuming that the concentration of the mixture is homogenous through the entire film, the SLD value of the polymer/CO_2 system is defined by

$$SLD_{mix}(z) = SLD_{polymer} \times \phi(z) + SLD_{SCF} \times (1-\phi(z)), \quad (1)$$

where SLD_{mix} is the *SLD* value of the mixture at a distance z from the substrate, SLD_{polymer} and SLD_{SCF} are the pure component *SLDs* of the polymer thin films and CO_2, respectively, and $\phi(z)$ is the volume fraction of the polymer at a distance z from the substrate. In order to calculate the SLD_{SCF} of the CO_2 dissolved in the polymer, the reported density of 0.956 g/cm^3 for CO_2 gas dissolved in a polymer was used[45]. To ensure conservation of mass, the volume fraction profiles were calculated such that the same amount of the polymer chains remained at all solvent concentrations including in the dry state. It was confirmed that the repeated pressurization and depressurization processes exhibit the same swelling behavior after the first pressurization process. Hence, it is reasonable to conclude that the polymer does not dissolve in the pure CO_2 phase during the NR experiments, which is consistent with the bulk PEO solubility with CO_2[46]. To ensure conservation of the mass of the polymer for the NR data fitting, the volume fraction profiles were calculated such that the amount of the polymer chains remained the same at all solvent concentrations including in the dry state (i.e., before CO_2 exposure).

4-3-3. Method of Melt Crystallization via the CO_2 Annealing

Based on the NR experiments to be discussed later, we turned out that the CO_2 exposure at P =9.7 MPa and T =4 8 °C for 1 h is satisfactory to achieve the amorphous melt state. After the CO_2 exposure, the chamber was rapidly quenched to atmospheric pressure within 10 s. As will be discussed later, the PEO films still contain the CO_2 molecules even after the quench process, resulting in the non-equilibrium melting state of the saturating polymer with CO_2. The saturating polymer was then transferred quickly to a temperature-controlled stage (10-60 °C). The kinetics of the recrystallization/dewetting was monitored at the given crystallization temperature (T_{cr}). Goel

and Beckman used a similar CO_2 process to establish a foaming method in which the bulk polymer is saturated with supercritical CO_2 ($scCO_2$, T_c = 31.3 °C and P_c = 7.38 MPa) followed by rapid depressurization[47, 48]. However, it was confirmed, by using small angle x-ray scattering experiments with a reflection geometry,[49] that the CO_2 process used in the present study generates only molecular scale porosity (the average size of 0.8 nm) with a relatively broad size distribution, which is consistent with a previous result on semi-crystalline poly (phenylene vinylene) films treated with the same CO_2 process. The lack of large voids in the PEO films after the CO_2 process may be due to the short diffusion path for residual CO_2, the high diffusivity of CO_2 in the rubbery PEO matrix, and the low storage modulus of PEO[50]. It should also be noted that, as we previously reported for another semi-crystalline polymer,[51] a slow depressurization process (with a quenching rate of ca. 0.15 MPa/min) from the same CO_2 conditions provokes more highly ordered crystalline structures with larger grain sizes. However, due to experimental difficulties in characterizing/visualizing the structural changes via the slow quench in the high-pressure cell, I here focus on only rapid quench that allows me partly preserve the swollen structures and then perform a suite of *ex-situ* structural characterization during the melt crystallization/dewetting processes from the non-equilibrium swollen state. At the same time, as controls, we treated the PEO thin films via a conventional high temperature annealing at 85 °C (> T_m) for 2 h, followed by rapid quench to the temperatures (between 10 and 60 °C) by transferring to the temperature-controlled sample stage.

4-3-4. Atomic Force Microscope (AFM)

The crystalline morphologies of the PEO thin films were observed by atomic force microscope (AFM) (Digital Nanoscope III). Both contact mode and standard tapping mode were conducted in air using a cantilever with a spring constant of 0.06 N/m and 40 N/m, respectively. The scan rate was 0.5 or 1.0 Hz with the scanning density of 256 or 512 lines per frame.

4-3-5. Polarized Optical Microscope (POM)

Polarized optical microscope (POM) measurements were conducted by using reflective light under an Olympus BHT Microscope equipped with differential interference contrast attachment for incident light after Nomarski (NIC Model). POM images were captured by a digital camera under polarized light at room temperature.

4-3-6. Glazing Incidence X-ray Diffraction (GID)

The grazing incidence x-ray diffraction (GID) measurements for the CO_2-treated and thermally annealed PEO thin films were carried out at the X22B beamline at National Synchrotron Light Source (NSLS) in Brookhaven National Laboratory (BNL). Two dimensional diffraction patterns were measured with a CCD camera (Princeton Instruments) with an incident x-ray angle of 0.2 °,

which is above the critical angle of PEO, hence illuminating the entire PEO films. The x-ray wavelength was 0.15 nm and the exposure time for all the measurements was 400 sec. As will be discussed later, the adsorbed layers on the substrates after a solvent-leaching process were measured at two undulator beamlines (the X9 beamline (NSLS) and the BL03XU at SPring-8), since the diffraction peaks were too weak to be detected at the bending magnet beamline.

4-3-7. X-ray Reflectivity (XR)

The x-ray reflectivity (XR) measurements were conducted at the X10B beamline (NSLS, BNL) to study the structures of the adsorbed polymer layers on Si substrates after the solvent-leaching process. The specular reflectivity was measured as a function of the scattering vector in the perpendicular direction to the film surface, $q_z = (4\pi\sin\theta)/\lambda$, where θ is the incident angle and λ is the x-ray wavelength (0.087 nm). The XR data was fit by using a standard multilayer fitting routine for a dispersion value (δ in the x-ray refractive index) in conjunction with a Fourier method, a powerful tool to obtain detailed structures for low x-ray contrast polymer multilayers[52, 53]. Note that δ is proportional to the density of a film and the δ value of the bulk PEO is $\delta_{bulk} = 1.14\times10^{-6}$ with the density of 1.2 g/cm^3.

4-4. Results and Discussion

4-4-1. Melting of PEO Thin Films in CO_2

Fig. 4-1 (a) shows the representative NR profiles for the 16 nm thick d-PEO film at the four different pressures and T = 48 °C. The solid lines correspond to the best-fits to the data based on the volume fraction profiles of the polymer, $\phi(z)$, shown in Fig. 1 (b). The thickness of the layer, which was initially 16 nm thick, increased to 20 nm at P = 2.9 MPa and further increased to 23 nm upon compression up to P = 9.6 MPa. It should be noted that the contribution from the density fluctuations of the pure CO_2 phase become significant near the ridge condition (P = 9.6 MPa at T = 48 °C) and overwhelms the observed intensity at $q_z > 0.1$ A^{-1} [30, 32]. This situation makes quantitative discussion about the presence of the adsorbed layer within the swollen PEO thin films or a CO_2 concentration gradient within polymer films[35, 54] difficult.

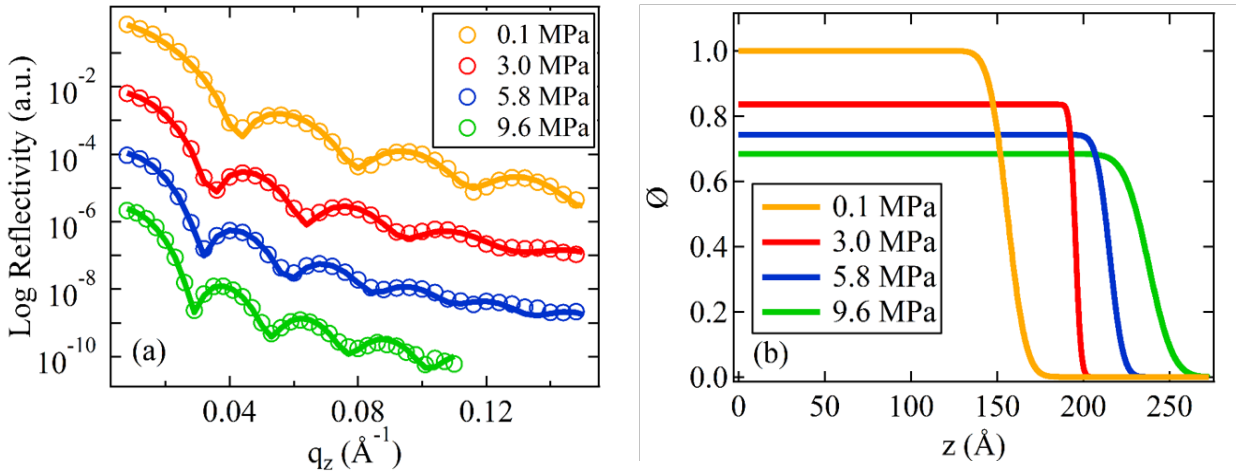

Fig. 4-1 (a) Representative NR profiles for the 16 nm thick d-PEO film at the four different pressures and T = 48 °C. The solid lines correspond to the best-fits to the data based on the corresponding concentration profiles shown in (b).

Fig. 4-2 shows the linear dilation (S_f) of the 16 nm thick film during the pressurization and depressurization processes at T = 48 °C. The S_f values were calculated by the equation, $S_f = (L - L_0) / L_0$, where L_1 and L_0 are the measured thicknesses of the swollen and unswollen film, respectively. In the pressurization process, there are the two distinctive features: (i) the large jump in S_f from 0.05 to 0.25 at P = 2.9 MPa, implying that the transition from the crystalline state to the amorphous state even at T = 48 °C ($< T_m$); (ii) the anomalous peak in S_f near P = 10 MPa that corresponds to the excess sorption of CO_2 molecules at the "density fluctuation ridge"[29-37] where the density inhomogeneity of CO_2 molecules in the supercritical state becomes maximum[55]. In the inset, I also plot the pressure dependence of the surface roughness obtained from the best-fits. From the figure,

it is clear that the roughness becomes minimum at P = 2.9 MPa, which is smaller than that at 0.1 MPa, and then increases with increasing pressure up to the ridge condition. This confirms that the melting occurs at P = 2.9 MPa, resulting in the much smoother surface, and the increase in the roughness at P > 2.9 MPa is attributed to the improvement of the solvent quality of CO_2 for the amorphous PEO. It should be emphasized that this melting pressure of 2.9 MPa is lower than those of bulk PEO films (4.8-10.7 MPa)[38, 39] under the same isothermal condition. Intriguingly, the gap disappeared in the depressurization process, and the S_f value decreased gradually to 0.15 at P = 0.1 MPa. Since this S_f value is much larger than that at the transition point (P = 2.9 MPa), the saturating polymer with residual CO_2 molecules creates the non-equilibrium amorphous state at T < T_m. Namely, this saturating CO_2/polymer mixture melt crystallizes during the continuous evaporation process at the given crystallization temperature T_{cr} (10-60 °C) until all thermodynamic forces driving mass transport vanishes. It was also confirmed that the repeated pressurization and depressurization processes displayed the same swelling behavior as that of the first depressurization process. Hence, I conclude that the swelling isotherms after the first pressurization are in equilibrium as sole functions of temperature and pressure.

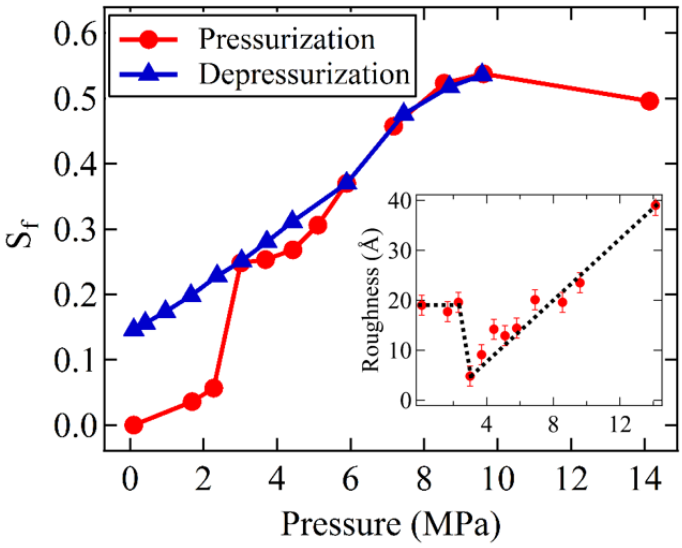

Fig. 4-2 Pressure dependence of the linear dilation (S_f) for the 16 nm thick d-PEO film at 48 °C during the pressurization and depressurization processes. In the inset, the pressure dependence of the surface roughness (the pressurization process) is plotted.

4-4-2. Crystalline Structures via Melt Crystallization

Fig. 4-3 shows typical AFM and POM images of the CO_2 treated PEO thin films evolved after the CO_2 process as functions of the film thickness and T_{cr}. It should be noted that the surface structures

of the 50 nm and 100 nm thick films grew so largely that AFM images could not capture the entire structural features. The surface morphologies are strongly dependent on the film thickness, as previously reported in CO_2 treated polycarbonate thin films[21]: (i) For the 50 and 100 nm thick films, the main folded-chain crystals grow into quasi-two dimensional spherulites with an averaged radius of a few hundred micrometers; (ii) For the 20 nm thick film, the polymer melt crystallized into finger-like seaweed patterns with an averaged width of a few micrometers, grown via the so-called "diffusion limited aggregation" (DLA) process[7, 56, 57].

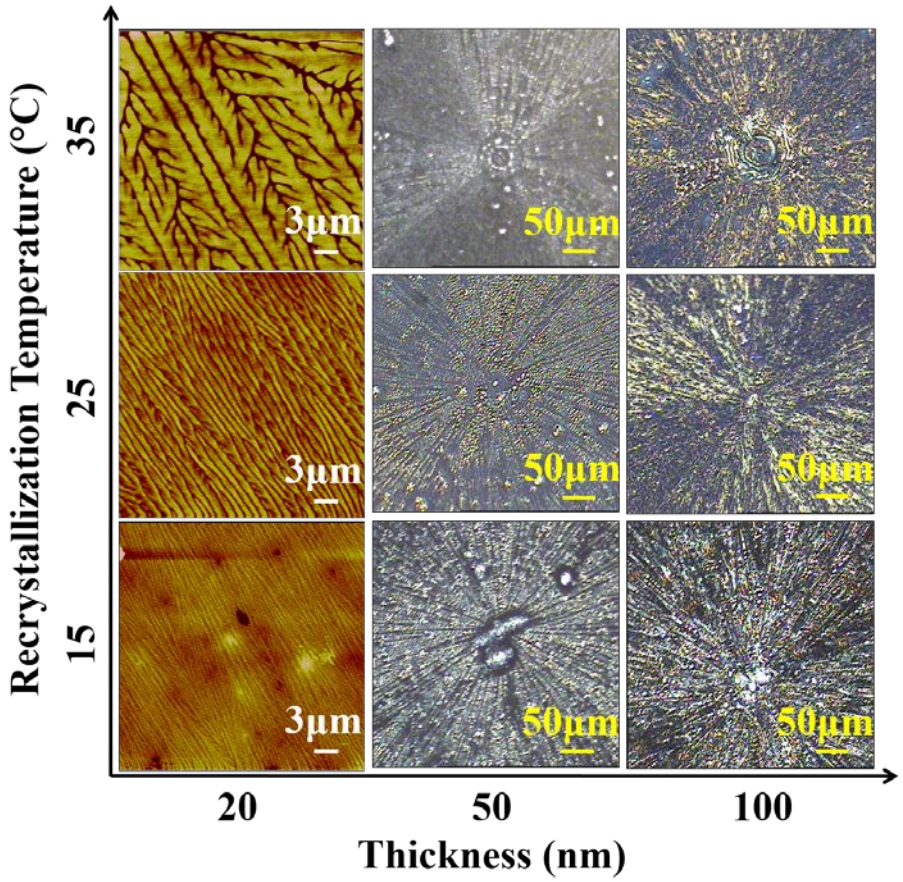

Fig. 4-3 AFM topographic and POM images of the CO_2-treated PEO thin films recrystallized as functions of the film thickness and T_{cr}.

Fig. 4-4 (a)-(b) display representative GID patterns of the CO_2-treated PEO thin films melt crystallized at T_{cr} = 25 °C. All the GID patterns show discrete diffraction peaks, indicating the formation of the highly ordered crystalline structures, in contrast to broad ring patterns for the thermally annealed PEO thin films (Fig. 4-5). To clarify the lamellar orientation, I simulated diffraction patterns for different lamellar geometries with crystallographic *a*, *b*, or *c* axis stands in the direction normal to the film surface. The details of the simulation have been described

elsewhere[22]. Note that the orientation along the standing axis with the Herman-Stein's orientation factor[58] was fixed to be 0.99, and only strong diffraction peaks were considered for the analysis. The key for the identification process was the position of the 120 diffraction peak at q = 13.6 nm^{-1} that locates along the q_{xy} axis for all the CO_2-treated PEO films.

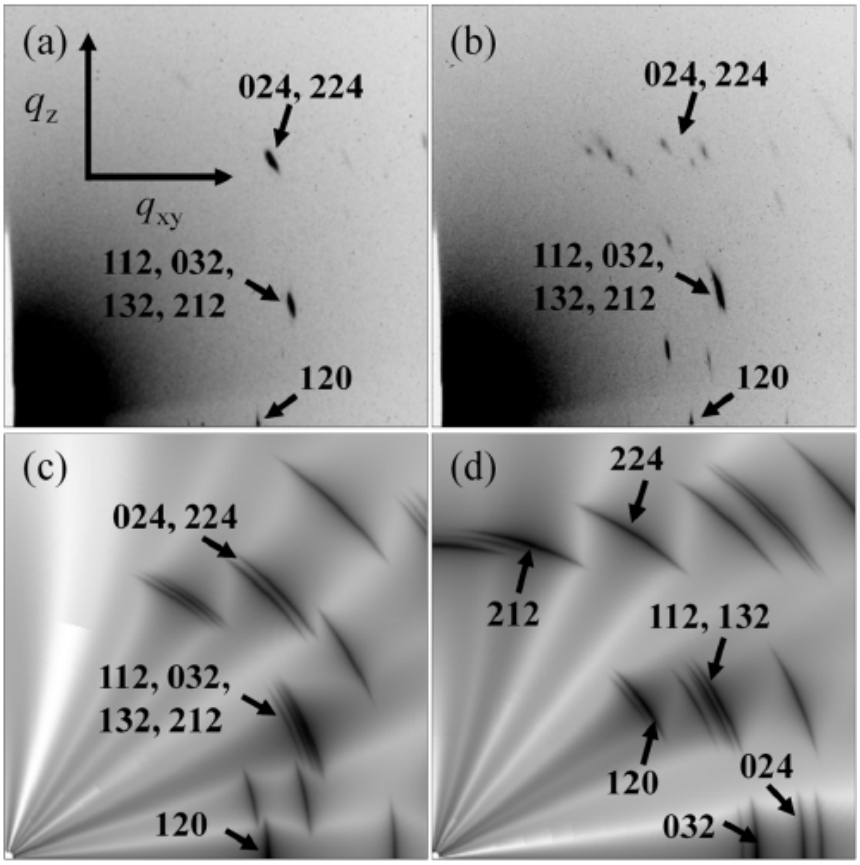

Fig. 4-4 Two-dimensional GID images of the CO_2-treated PEO thin films melt crystallized at T_{cr} = 25 °C: (a) 20 nm; (b) 50 nm thick films. The simulated diffraction patterns described in the main text are shown; (c) for crystallographic *c*-axis standing (a flat-on lamellar orientation); (d) for crystallographic *a*-axis standing (an edge-on lamellar orientation).

The comparisons the between the simulated (Fig. 4-4(c) for a flat-on lamellar and (d) for an edge-on lamellar) and experimental results elucidated that the lamellar orientation is assigned to be the geometry with *c* axis standing (i.e., a flat-on lamellar orientation where the lamellar layers run parallel to the surface). Consequently, I lead to the conclusion that the flat-on lamellar structure is preferably formed in the PEO films after the CO_2 process regardless of T_{cr} and the film thickness. It was also used the different CO_2 pressures ranging from 2.9 to 15 MPa at T = 48 °C, where the polymer is still in the melting state, to see the effect of the excess sorption on the resultant crystal

morphologies. The GID results revealed that the flat-on lamellar orientation occurs regardless of the CO_2 pressures, while the size of the crystal grain is the largest at 9.7 MPa (i.e., the density fluctuation ridge). This can be explained by the fact that the amount of the residue CO_2 molecules after the rapid depressurization is the most at the ridge condition so that the melt crystallization proceeds at the slowest rate. Hence, the anomalous plasticization effect near the density fluctuation ridge[30, 49, 51] is not crucial for the resultant crystal orientation.

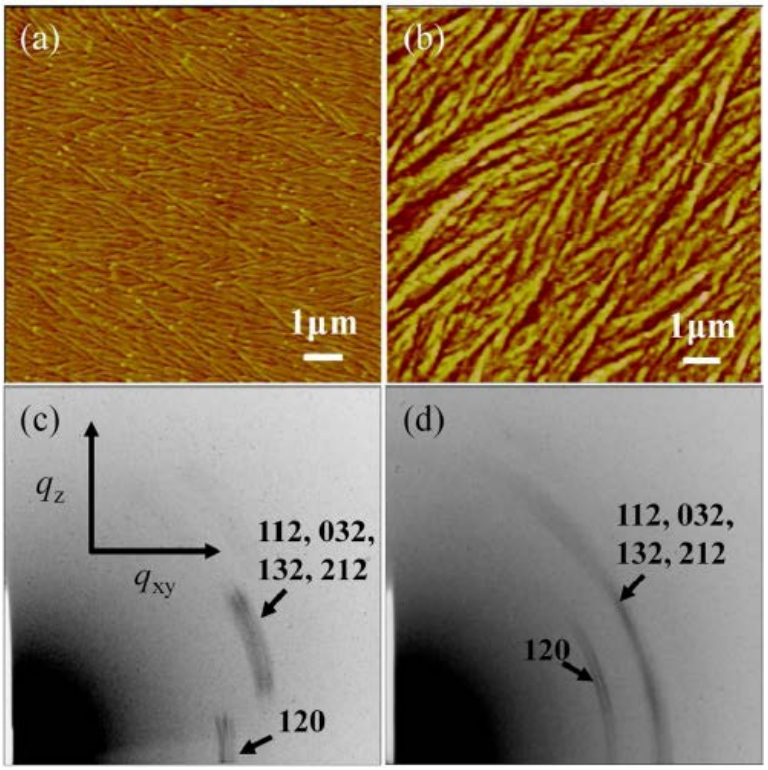

Fig. 4-5 AFM topographic images of the thermally annealed PEO thin films recrystallized at T_{cr} = 25°C: (a) 20 nm; (b) 50 nm thick film. The corresponding two-dimensional GID results are shown in (c) for the 20 nm thick and (d) for the 50 nm thick, respectively.

To highlight the uniqueness of the CO_2-induced melt crystallized structures, I also studied the structures melt crystallized via the conventional thermal annealing process. Fig. 4-5 (a) and (b) show representative AFM height images of the thermally annealed PEO thin films (20 and 50 nm thick) melt crystallized at T_{cr} = 25 °C. As previously reported,[59, 60] flat-on lamellar structures characterized as screw dislocation nucleation site or terrace structure is seen in the 20 nm thick film. In contrast, for the 50 nm thick film, the sheaf-like morphology, which is an indication of the edge-on lamellar orientation, is observed. The detailed structures were further examined by GID. Figs. 4-5 (c) and (d) show the GID patterns for the 20 and 50 nm thick films, respectively. The 120

diffraction peak for the 20 nm thick still locates along the q_{xy} axis, indicating the flat-on lamellar orientation. On the other hand, the 120 diffraction peak for the 50 nm thick film shifts to the off-axis position. Based on the aforementioned simulation result, I found that the orientation corresponds to edge-on where the lamellar layers run perpendicular to the film surface. In addition, the 120 diffraction peak for the 50 nm thick film is rather azimuthally smeared, implying that the two lamellar geometries (i.e., the flat-on and edge-on) coexist within the film. Table 4-1 summarizes the orientations of the lamellar structures for the melt crystallized PEO thin films via the thermal annealing processing. From the table, we can see the following evidences: (i) the flat-on lamellar orientation is preferable for all the thermally annealed PEO thin films melt crystallized at and above T_{cr} = 35 °C; (ii) Below T_{cr} = 35 °C, the random orientation of the edge-on lamellar is formed in the 50 and 100 nm thick films, while only the flat-on lamellar orientation is found in the 20 nm thick thermally annealed films; (iii) the dewetting process occurs in all the thermally treated films at T_{cr} = 60 °C, which is very close to the bulk T_m. I will discuss the dewetting in detail in the next section. Hence, the thermally annealed films clearly show the thickness dependence of the orientation, in contrast to the CO_2-treated PEO thin films.

Table 4-1 Lamellar orientation and instability of the PEO thin films prepared via the thermal annealing and CO_2 processing as functions of the film thickness and T_{cr}.

	Thermal annealing			CO_2 processing		
T_{cr} (ºC)	20 nm	50 nm	100 nm	20 nm	50 nm	100 nm
60	Dewet	Dewet	Dewet	Dewet	Dewet	Dewet
55	Flat-on[a]	Flat-on	Flat-on	Dewet	Dewet	Dewet
40	Flat-on	Flat-on	Flat-on	Dewet	Dewet	Dewet
35	Flat-on	Flat-on	Flat-on	Flat-on	Flat-on	Flat-on
30	Flat-on	Edge-on[b]	Edge-on[b]	Flat-on	Flat-on	Flat-on
15	Flat-on	Edge-on[b]	Edge-on[b]	Flat-on	Flat-on	Flat-on
10	Flat-on	Edge-on[b]	Edge-on[b]	Flat-on	Flat-on	Flat-on

[a]: Flat-on orientation

[b]: Coexistence of the flat-on and edge-on orientations

Wang et al.[12] reported the effects of quench depth and film thickness on lamellar orientations

formed in semi-crystalline polymer thin films at atmospheric pressure. They introduced the three-T_g layered model (i.e., the surface mobile layer ($T_g < T_{g, bulk}$), the middle bulk-like layer ($T_g = T_{g, bulk}$) and the substrate bound layer ($T_g > T_{g, bulk}$)). It is postulated that each region has the different bell-shaped overall crystallization rate curve as a function of crystallization temperature in the range between T_g and T_m, as presented in Fig. 1-3. Depending on the crystallization rate at a given temperature, they proposed that the crystallization initiates either at the free-surface (in case of a higher crystallization temperature), where the chains are highly mobile exhibiting lower T_g[15, 61, 62] and reduced viscosity[18, 19] compared to the bulks, or the substrate interface (in case of a lower crystallization temperature), where the chains are barely mobile even at $T >> T_g$[63] due to the adsorption. Hence, my experimental results for the thermally annealed 50 and 100 nm thick films can be in principle explained by their model, but not for the 20 nm thick film. It is postulated that the persistence of the flat-on lamellae in the 20 nm thick films even at the higher T_{cr} is attributed to the effect of an irreversibly adsorbed layer. This point will be discussed later.

4-4-3. Dewetting Structures

In this section I focus on the dewetting behavior induced by the CO_2 annealing at high T_{cr}. It is known that dewetting is a phenomenon resulted from a breakup of thin films into droplets on substrate surfaces due to high mobility of polymer chains[64]. Fig. 4-6 shows representative POM images for the CO_2 treated 50 nm-thick PEO films at different T_{cr}. Typical hole-shaped breakup structures[65-67] were observed in the films at and above T_{cr}= 40 °C, while the thermally annealed 50 nm thick PEO film dewetted at $T_{cr} \geq 60$ °C. Hence, the lower limit temperature of the dewetting shifts to lower temperature side (by about 15 °C) for the CO_2 treated PEO film relative to that of the annealed PEO films. This is due to the plasticization effect of CO_2 associated with the residual CO_2 molecules. We found that the dewetting is most severe at T_{cr} = 40 °C (Fig. 4-6(c)), which may correspond to the transition temperature between the crystallization and dewetting, as Okerberg et al. pointed out[68]. The average height and the width of the rims (i.e., the hole boundary colored in light blue in Fig. 4-6(a)) are about 50-70 nm and 5-10 μm, respectively. Based on the AFM image shown in Fig. 4-6 (d), I found that the polymer chains inside of the rims still crystallize into large needle-like (flat-on) patterns. Further AFM examination near the rims demonstrated that the needlelike structures are initiated from the rim and propagate into the inner region of the holes, as reported by Reiter and Sommer[56]. In addition, It was also confirmed that polymer chains in the matrix (non-dewetting) region crystallize as well, forming a flat-on lamellar orientation.

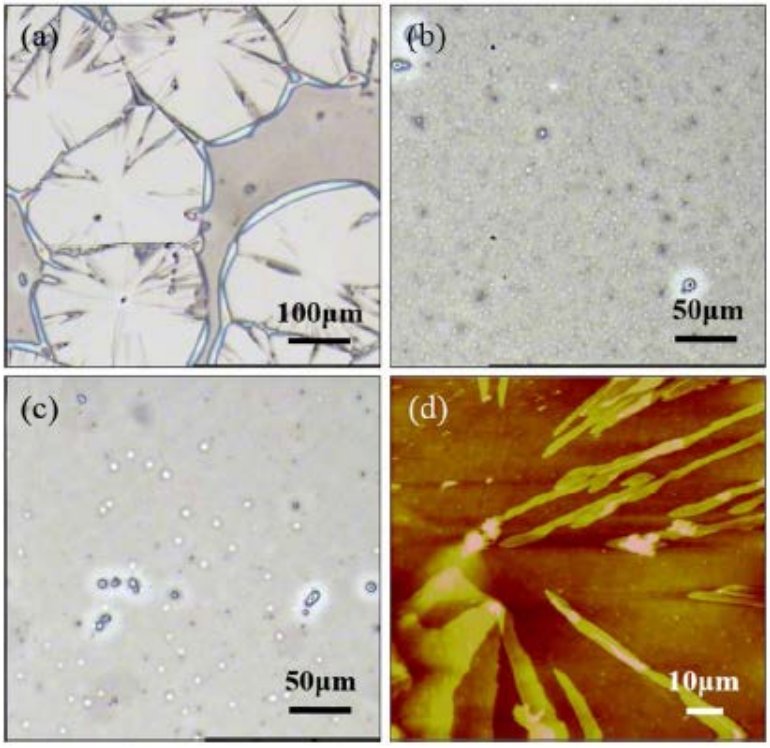

Fig. 4-6 Representative POM images of the CO_2-treated 50 nm thick PEO thin films dried after 1 h at the given T_{cr}s: (a) 40 °C; (b) 45 °C; (c) 50 °C. The AFM topographic image inside of the rim in (a) is shown in (d). The height scale for the AFM image is 0-50 nm.

In order to shed light on the process, I further studied the time evolution of the dewetting structures. Figure 4-7 shows the dewetting structures of the CO_2 treated PEO thin films (20 and 50 nm in thickness) induced at T_{cr} = 40 °C. The results clearly show that the sizes of the dewetting structures are quite different between the 20 and 50 nm-thick films during the same time period. For the 20 nm thick film, the kinetics is rather slow and micron-scale dewetting structures become noteworthy after 12 h. On the other hand, typical ring-like dewetting holes with a few hundred microns in diameter were observed in the 50 nm (and 100 nm) thick films even after 1 h, and no further growth of these holes was observed in the thicker films during the course of up to 12 h. These results suggest that the dewetting kinetics for the CO_2 treated PEO thin films is significantly perturbed when the thickness is down to 20 nm. In order to investigate the effect of the CO_2 process on this retarded dewetting kinetics, I also induced dewetting of the thermally annealed films at T_{cr} = 60 °C, which is close to the bulk T_m. As a result, the same trend was indicated: the slowing down of the dewetting kinetics of the 20 nm thick film compared to the 50 and 100 nm thick films. It is known that the dewetting velocity is independent of film thickness for “nonslipping” (sticking) films[69], while, in case of slipping films, thinner films dewet faster than thicker ones[70-72]. Since the

interfacial energy of the PEO/H-Si system is very low (i.e., an attractively interacting system), the dewetting velocity would remain constant regardless of the film thickness. This is at least true for the 50 nm and 100 nm thick thermally annealed PEO films. Below we show that this thickness dependence of the dewetting kinetics is as a consequence of the interplay between the polymer/air interface, where the dewetting is initiated, and polymer/substrate interface, where the adsorbed polymer layer is formed.

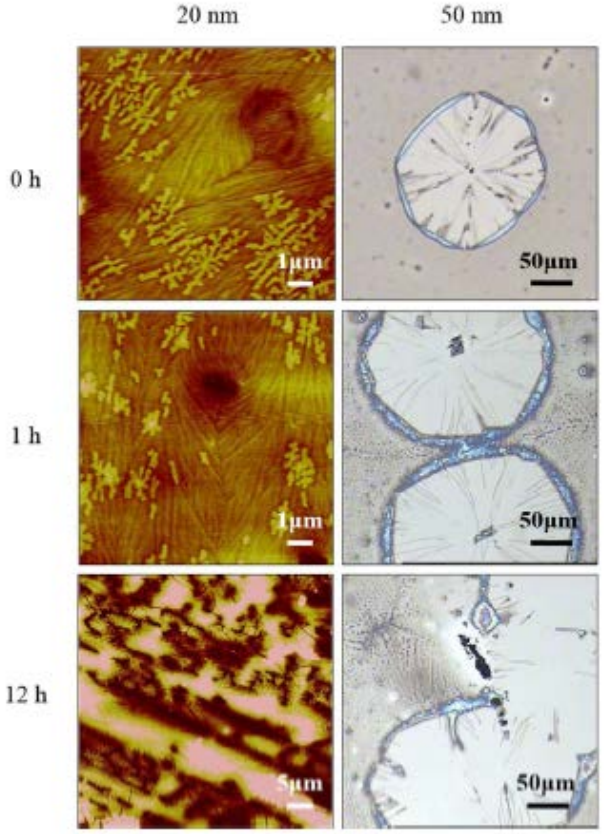

Fig. 4-7 Time evolution of the surface morphologies of the CO_2-treated PEO thin films dried at T_{cr} = 40°C and the given times depicted with AFM for the 20 nm film (left column) and POM for the 50 nm film (right column). The height scale for the AFM images is 0-20 nm.

4-4-4. Crystallinity of Adsorbed Layers Formed by Thermal Annealing

Before moving into the main discussion, I would like to briefly explain about substrate-bound irreversibly adsorbed polymer layers. The adsorbed polymer layers at the solid-polymer melt interface have recently been the subject of extensive study due to their strong influence on the physical and mechanical properties of polymeric materials confined at the nanometer scale[20, 63, 73-79]. Several research groups utilized the approach proposed by Guiselin,[80] which combines prolonged

high-temperature annealing and subsequent solvent leaching,[63, 73, 75, 76] and demonstrated the formation of adsorbed monolayers with the thickness of less than *R*g against planar walls (substrates). The formation of the adsorbed layer has also been reported for semi-crystalline polymers prepared on planar substrates[20-23].

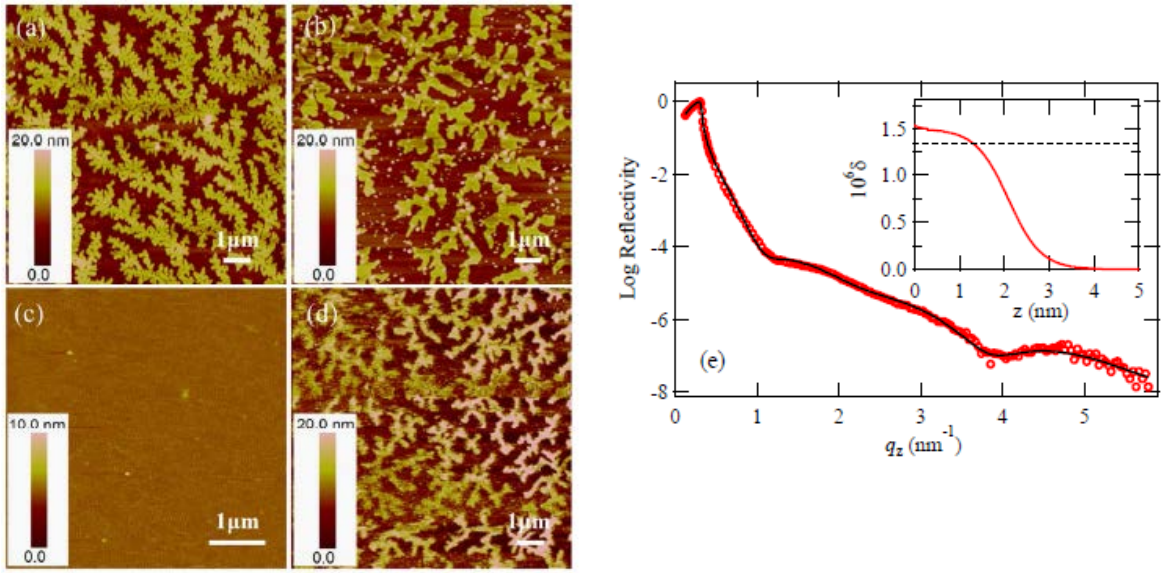

Fig. 4-8 AFM topographic images of the PEO adsorbed layer; (a) 8.5 nm; (b) 6.5 nm; (c) 2.5 nm. The CO_2-treated adsorbed layer (6.5 nm in thickness) is shown in (d). The XR profile (red circles) of the 2.5 nm adsorbed layer is shown in (e). The solid line corresponds to the best-fit to the data based on the three-layer model (i.e., PEO, SiO_2, and Si layers). The thickness of the SiO_2 layer was determined to be about 1.3 nm from an independent XR measurement on a bare H-Si substrate. In the inset, the dispersion profile (δ in the X-ray refractive index) obtained by the best-fit is shown. The surface roughness is estimated to be 0.7 ± 0.1 nm. The dotted line in the inset corresponds to the δ value of the bulk. The formation of the high-density adsorbed layer next to a Si substrate is consistent with previous reports using different polymers.

At first, the crystalline structures of the adsorbed layer which was formed in the thermally annealed PEO films (50 nm thick) were investigated. The PEO films annealed at 85 °C for 2 h were solvent leached in baths of fresh chlorobenzene at room temperature repeatedly. The details of the leaching process have been described elsewhere[79]. After each leaching process, the residue layers were annealed at 85 °C for 1 h to remove any excess solvent trapped in the films. The thickness of the residual layer was measured by using the ellipsometer and XR. A series of the leaching

experiments gave rise to the residue (adsorbed) layers on H-Si substrates with different thicknesses ranging from 2.5 nm to 8.5 nm. It was found that the residual layer of 2.5 nm in thickness (Fig. 4-8(e)) is the final adsorbed layer of which thickness remains unchanged with any further aggressive leaching. As shown in Fig. 4-8, the AFM experiments for these adsorbed layers clearly showed the finger-like seaweed flat-on lamellar structures, except for the 2.5 nm thick adsorbed layer.

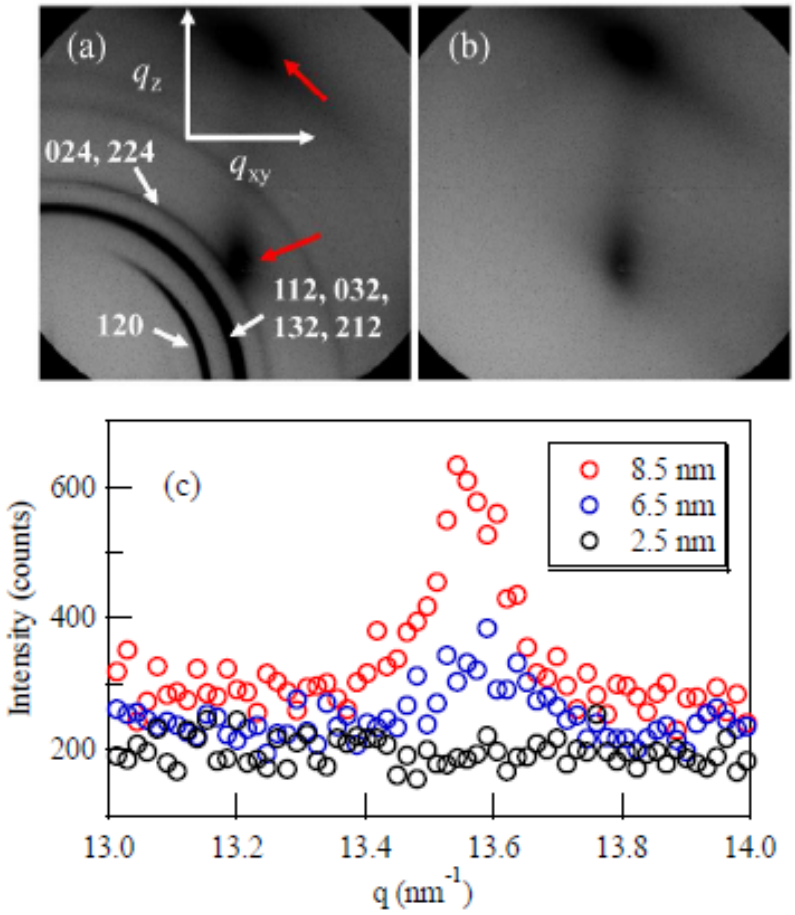

Fig. 4-9 Two-dimensional GID results for (a) the 50 nm thick PEO thin film (as-spun) and (b) the 2.5 nm flattened layer. The dark spots in both images (indicated by the red arrows) correspond to the scattering contributions from the native oxide layer formed on the Si substrate. The one-dimensional GID results for the "transient" adsorbed layers (6.5nm and 8.5 nm in thickness) and the flattened layer (2.5 nm in thickness) are shown in (c). The presence of the 120 diffraction peak at around q = 13.6 nm^{-1} was used to determine the existence of the crystalline structure.

The GID experiments at the X9 beamline (NSLS) were carried out to further explore the structure

of the 2.5 nm thick adsorbed layer. As compared to the GID data for the thermally annealed PEO thin film (50 nm thick, Fig. 4-9(a)), there are no diffraction peaks from the final adsorbed layer (Fig. 4-9(b)). On the other hand, GID experiments at SPring-8 clarified the 120 diffraction peak from the other adsorbed layers (Fig. 4-9(c)). Hence, these AFM and GID results draw the conclusion that the chain architecture of the 2.5 nm thick final adsorbed layer prevents the chain folding near the solid wall. I believe that this final layer corresponds to the "flattened" layer[79] with many solid/segment contacts that is composed of the early-arriving polymer chains to the substrate during the adsorption process. On the other hand, the other thicker adsorbed layers should be composed of the two layers: the inner flattened layer and the outer loosely adsorbed layer that is formed by the late-coming chains during the adsorption process, which find less free surface areas and hence adsorb more loosely with fewer adsorbed sites[79]. It was previously demonstrated that the loosely adsorbed PS chains can be preferentially removed by optimizing solvent leaching conditions, while the flattened layer remains on the substrate. Therefore, it is reasonable to suppose that the loosely adsorbed polymer chains in the present study are gradually washed away during the consecutive leaching, resulting in the "transient" adsorbed layers with 4~8 nm in thickness. The picture of the substrate-bound adsorbed layer is presented in Fig. 4-10.

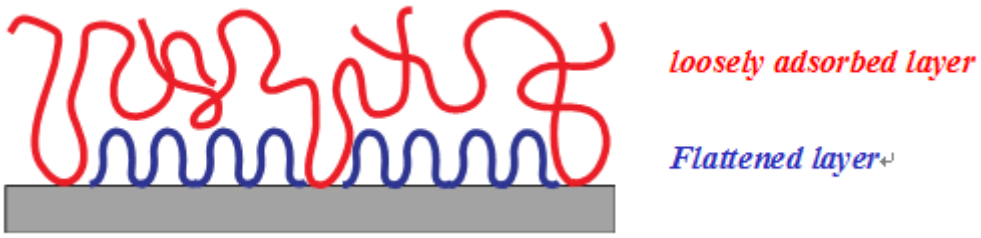

Fig. 4-10 Speculated picture of the flattened layer and the loosely adsorbed layer onto the substrate wall[79].

4-4-5. Formation of Adsorbed Layers Induced by ScCO$_2$-treatment

Next, I clarify the formation of the adsorbed layer in the CO_2 treated films before the subsequent thermal annealing at T_{cr}. With the aforementioned leaching process in conjunction with XR and AFM, it was found the presence of the final flattened layer (~2.5 nm in thickness) as well as the outer loosely adsorbed layer in all the CO_2 treated PEO films (regardless of the film thickness and CO_2 conditions). At the same time, I applied the same CO_2 treatment (i.e., the CO_2 exposure at T = 48 °C and P = 9.7 MPa and subsequent rapid depressurization) to the unexposed PEO adsorbed layers shown in Fig. 4-8(a)-(c). As shown in Fig. 4-8 (d), the AFM result showed that the finger-like seaweed pattern of the CO_2 treated adsorbed layer (the original thickness of 6 nm) is

slightly denser than that of the unexposed one (Fig. 4-8 (b)). It was also found that the magnitude of the swelling (obtained by the ellipsometer and XR measurements) of the CO_2 treated adsorbed layer is much less (S_f = 0.03) than that of the spin cast PEO films after the complete depressurization to air (S_f = 0.15, Fig. 4-2). Hence, it is expected that the plasticization effect of CO_2 at the interface is achieved to only a limited extent at the polymer-substrate interface, as compared to the rest of the spin-cast film. Consequently, I postulate that this limited plasticization effect plays a role in accelerating the polymer adsorption and chain folding rather than melting of the crystalline structures near the interface. According to a previous report by Jia and McCarthy,[81] CO_2 interacts with a hydroxyl group on a Si substrate, screening the polymer-substrate interaction. This would be the case for a polycarbonate/CO_2 system reported by Lan and co-workers[21]. However, as Jia and McCarthy also demonstrated, the screening effect is not fully achieved when a strong interaction between a polymer and Si substrate (e.g., our present system, PEO/H-Si) is present. It is therefore suggested that systematic studies on various polymers with different segment/solid interactions is necessary to provide a better understanding of the adsorption mechanism in the presence of CO_2.

4-4-6. Mechanism of scCO_2-assisted Melt Crystallization of PEO Thin Films

Based on the above results, I propose the scCO_2-assisted melt crystallization process of the PEO thin films associated with the adsorbed layer. The key is the interaction between the adsorbed layer and unadsorbed chains near the substrate interface. It has been indicated the presence of the so-called reduced mobility interface (RMI) layer[82, 83] (or the transition zone) to ensure continuity in the mobility profile from the adsorbed layer to the bulk through chain entanglements[24]. Napolitano et al. reported that the RMI layer of poly (ethylene terephthalate) thin films prepared on aluminum substrates is about 20 nm in thickness[20]. While the formation/extent of the RMI layer may depend on the strength of the substrate interaction, the flexibility of polymer chains, or thermal annealing conditions,[15, 82-84] it is reasonable to suppose that the part or whole of the interior region of the 20 nm thick PEO films corresponds to the transition zone. For the PEO/H-Si system, the interaction is strong (“sticky”) so that the adsorbed chains are predicted to form flat-on lamellar formation at the substrate,[85] which is in good agreement with the present AFM results. If the melt crystallization from the amorphous state would be initiated from the adsorbed lamellar layer (that remains unmelted even at $T >> T$m as seen in PE thin films[22]) as seeds, the free polymer chains in the transition zone might then form the flat-on lamellae with the same orientation as for the adsorbed lamellar layer in order to maximize the contacts, thereby stabilizing the interface[86]. This would be the reason why the flat-on lamellar orientation in the presence of the adsorbed layer is favorable for the 20 nm thick films regardless of a choice of T_{cr} and the use of the CO_2 annealing. It should also be noted that the melt crystallization process along with the adsorbed layer is analogous to the “self-seeding” process for replicating polymer single crystals on Si substrates[87]. The question is then why the flat-on lamellar orientation persists up to the topmost surface of the 100 nm thick CO_2 treated film, in contrast to the thermally annealed films where the edge-on lamellar formation is

dominant at the topmost surface of more than 50 nm thick films at the lower T_{cr} (see, Table 4-1). This may be attributed to great reductions of both T_m and T_g of the swollen PEO thin films with the CO_2 annealing. As summarized in Table 4-1, the plasticization effect of CO_2 shifts the film stability (i.e., dewetting) to a lower temperature side. Hence, with the aforementioned three-layer model,[12] it may conclude that the T_{cr} values used in the present study (as low as 10 °C) may not be low enough to induce the edge-on orientation at the topmost surface. As a consequence, the flat-on lamellar formation would be proceeded from the surface-bound flat-on lamellar layer and propagate into the film interior without emerging the independent nucleation at the top surface. Further experiments at lower T_{cr} deserve future work.

4-4-7. Thermal Stability Associated with Adsorbed Layer

Finally, I look into the role of the adsorbed layer in the dewetting process. As previously reported, the loosely adsorbed polymer layer has nearly zero thermal expansion[79] and is immobile[63] in air (or under vacuum) even at $T >> T_g$. While the adsorbed layer swells in CO_2, the degree is extremely small. Hence, the strong hindrance of the mobility of the adsorbed chains still sustains even in the CO_2 treated PEO films. As a result, the effect of the adsorbed layer propagates into the film interior via the chain entanglements, resulting in the strongly hindered dewetting dynamics of the 20 nm thick CO_2 treated film (the same mechanism should be applicable to the 20 nm thick thermally annealed film). It is important to mention that, the propagation distance of the substrate effect of the CO_2 treated films is limited to the region within 50 nm from the substrate interface, based on the dewetting kinetics at the topmost surfaces of the 50 nm thick and 100 nm thick films.

4-5. Conclusion

In this Chapter, the CO_2-induced crystallization and dewetting of PEO thin films (20, 50, and 100 nm in thickness) were investigated by a suite of the surface-sensitive experimental techniques. Spin-cast PEO films (without further high temperature annealing) prepared on Si substrates were exposed to CO_2 at T = 48 °C and P =9.7 MPa for 1 h to melt the polymer and then depressurized quickly to atmospheric pressure, allowing melt crystallization (and/or dewetting) from the non-equilibrium melting state at the given crystallization temperatures (T_{cr}). As a result, it was found that all the CO_2 treated films show the flat-on lamellar structures regardless of the thickness and T_{cr}. This contrasts the experimental results from the PEO thin films crystallized via the conventional thermal annealing process where the edge-on lamellar orientation occurs at the film surface. In addition, typical hole-shaped breakup dewetting structures were found at the film surface of the CO_2 treated PEO films at and above T_{cr} = 40 °C, while the thermally annealed PEO film dewetted at $T_{cr} \geq 60$ °C. Interestingly, it was found that the dewetting kinetics is severely hindered for the 20 nm thick CO_2 treated films compared to that for the 50 nm and 100 nm-thick CO_2 treated films, while the dewetting kinetics is expected to be independent of film thickness for the present attractively interacting system[69].

It is conclusive that the formation of the very thin adsorbed layer during the CO_2 annealing plays vital roles in the observed melt crystallization and dewetting processes. After the CO_2 annealing, I used the solvent leaching process with chlorobenzene to extract the adsorbed layer that cannot be dissolved even in a good solvent. The systematic leaching experiments revealed the formation of the non-crystallized adsorbed layer of about 2.5 nm in thickness as well as the transient crystallized adsorbed layers (with up to 8.5 nm in thickness) on the Si substrates. It was also found that the plasticization effect of CO_2 on the adsorbed chains is achieved to only a limited extent, as compared to the rest of the spin-cast films. Hence, this limited plasticization effect results in accelerating the polymer adsorption and chain folding rather than the melting of the crystalline structures near the interface. I therefore propose that the “bound” lamellar layer, which does not melt in CO_2, initiates the melt crystallization from the non-equilibrium melting state as seeds$_2$ during the subsequent annealing process. In addition, the limited plasticization effect does not improve the inherent hindrance of the mobility of the adsorbed chains either, persisting the long-range perturbations associated with the adsorbed layer into the film interior through chain entanglements. Since the formation of the adsorbed layer would be a general phenomenon regardless of monomer-substrate interactions, the present insight brings new attention to the effects of the adsorbed layer on the crystallization and dewetting processed under nanoconfined geometries. Also, the present research demonstrates that the CO_2 solvent annealing can be used as a low-temperature, environmentally green, and more effective process to produce controlled crystalline morphologies with long-range-order in place of conventional high-temperature thermal annealing.

4-6. References

1. Wilkinson, A. N.; Ryan, A. J., *Polymer Processing and Structre Development*. Springer: 1998.
2. Nelson, J. *Mater. Today* **2011,** 14, 462-470.
3. Klauk, H., *Organic Electronics: Materials, Manufactring and Applications*. Wiley-VCH: 2006.
4. Friend, R. H.; Gymer, R. W.; Holmes, A. B.; Burroughes, J. H.; Marks, R. N.; Taliani, C.; Bradley, D. D. C.; Santos, D. A. D.; Bredas, J. L.; Logdlund, M.; Slaneck, W. R. *Nature* **1999,** 397, 121-128.
5. Despotopoulou, M. M.; Frank, C. W.; Miller, R. D.; Rabolt, J. F. *Macromolecules* **1996,** 29, 5797-5804.
6. Frank, C. W.; Rao, V.; Despotopoulou, M. M.; Pease, R. F. W.; Hinsberg, W. D.; Miller, R. D.; Rabolt, J. F. *Sicence* **1996,** 273, 912-915.
7. Reiter, G.; Sommer, J. U. *J. Chem. Phys.* **2000,** 112, 4376.
8. Cho, K.; Kim, D.; Yoon, S. *Macromolecules* **2003,** 36, 7652-7660.
9. Schonherr, H.; Frank, C. W. *Macromolecules* **2003,** 36, 1188-1198.
10. Wang, Y.; Ge, S.; Rafailovich, M. H.; Sokolov, J. C.; Zou, Y.; Ade, H.; Ning, J. L.; Lustiger, A.; Maron, G. *Macromolecules* **2004,** 37, 3319.
11. Wang, Y.; Rafailovich, M.; Sokolov, J.; Gersappe, D.; Araki, T.; Zou, Y.; Kilcoyne, A. D. L.; Ade, H.; Marom, G.; Lustiger, A. *Phys. Rev. Lett.* **2006,** 96, 028303.
12. Wang, Y.; Chan, C.-M.; Ng, K.-M.; Li, L. *Macromolecules* **2008,** 41, 2548-2553.
13. Priestley, R. D.; Ellison, C.; Broadbelt, L. J.; Torkelson, J. M. *Science* **2005,** 309, 456.
14. Jukes, P. C.; Das, A.; Durell, M.; Trolley, D.; Higgins, A. M.; Geoghegan, M.; Macdonald, J. E.; Jones, R. A. L.; Brown, S.; Thompson, P. *Macromolecules* **2005,** 38, 2315-2320.
15. Ellison, C. J.; Torkelson, J. M. *Nature Mater.* **2003,** 2, 695.
16. Fakhraai, Z.; Forrest, J. A. *Science* **2008,** 319, 600.
17. Yang, Z.; Fujii, Y.; Lee, F. K.; Lam, C.-H.; Tsui, O. *Science* **2010,** 328, 1676.
18. Bodiguel, H.; Fretigny, C. *Phys. Rev. Lett.* **2006,** 97, 266105.
19. Koga, T.; Li, C.; Endoh, M. K.; Koo, L.; Rafailovich, M. H.; Narayanan, S.; Lee, D. R.; Lurio, L.; Sinha, S. K. *Phys. Rev. Lett.* **2010,** 104, 066101.
20. Napolitano, S.; Prevosto, D.; Lucchesi, M.; Pingue, P.; D'Acunto, M.; Rolla, P. *Langmuir* **2007,** 23, 2103-2109.
21. Lan, Q.; Yu, J.; Zhang, J.; He, J. *Macromolecules* **2011,** 44, 5743.
22. Asada, M.; Jiang, N.; Sendogdular, L.; Gin, P.; Wang, Y.; Endoh, M. K.; Koga, T.; Fukuto, M.; Schultz, D.; Lee, M.; Li, X.; Wang, J.; Kikuchi, M.; Takahara, A. *Macromolecules* **2012,** 45, 7098-7106.
23. Vanroy, B.; Wubbenhorst, M.; Napolitano, S. *ACS Macro Lett.* **2013,** 2, 168-172.
24. Wu, W. L.; Wallace, W. E.; Zanten, J. H. v.; Bauer, B. J.; Liu, D. W.; Wong, A. *Polymer* **1997,** 38, 2583.

25. Wissinger, R. G.; Paulaitis, M. E. *J. Poly. Sci. Polym. Phys. Ed.* **1987,** 25, 2497-2510.
26. Goel, S. K.; Beckman, E. J. *Polymer* **1993,** 34, 1410-1417.
27. Condo, P. D.; Paul, D. R.; Johnston, K. P. *Macromolecules* **1994,** 27, 365-371.
28. McHugh, M. A.; Krukonis, V., *Supercritical Fluids Extraction Principles and Practice*. Woburn: 1994.
29. Koga, T.; Seo, Y. S.; Hu, X.; Kwanwoo, S.; Zhang, Y.; Rafailovich, M. H.; Sokolov, J. C.; Chu, B.; Satija, S. K. *Europhys. Lett.* **2002,** 60, 559.
30. Koga, T.; Seo, Y. S.; Zhang, Y.; Sin, K.; Kusano, K.; Nishikawa, K.; Rafailovich, M. H.; Sokolov, J. C.; Chu, B.; Peiffer, D.; Occhiogrosso, R.; Satija, S. K. *Phys. Rev. Lett.* **2002,** 89, 125506.
31. Sirard, S. M.; J., Z. K.; Sanchez, L. C.; Green, P. F.; Johnston, K. P. *Macromolecules* **2002,** 35, 1928.
32. Koga, T.; Seo, Y. S.; Shin, K.; Zhang, Y.; Rafailovich, M. H.; Sokolov, J. C.; Chu, B.; Peiffeer, D.; Satija, S. K. *Macromolecules* **2003,** 36, 5236.
33. Koga, T.; Ji, Y.; Seo, Y. S.; Rafailovich, M. H.; Sokolov, J. C.; Satija, S. K. *J. Polym. Sci., Part B:Polym. Phys.* **2004,** 42, 3282.
34. Li, Y.; park, E.; Lim, K.; Johnston, K. P.; Green, P. F. *J. Polym. Sci., Part B:Polym. Phys.* **2007,** 45, 1313.
35. Li, X. X.; Vogt, B. D. *Polymer* **2009,** 50, 4182-4188.
36. Koga, T.; P. Gin, H.; Yamaguchi; Endoh, M.; Asada, M.; Sendogdular, L.; Kobayashi, M.; Takahara, A.; Akgun, B.; Satija, S. K.; Sumi, T. *Polymer* **2011,** 52, 4331-4336.
37. Mendoza-Galvan, A.; Trejo-Cruz, C.; Solis-Canto, O.; LunaBarcenas, G. *J. Supercrit. Fluids* **2012,** 64, 25-31.
38. Weidner, E.; Wiesmet, V. *J. Supercritical Fluids* **1997,** 10, 139.
39. Madsen, L. A. *Macromolecules* **2006,** 39, 1483.
40. Shin, K.; Hu, X.; Zheng, X.; Rafailovich, M. H.; Sokolov, J.; Zaitsev, V.; Schwarz, S. A. *Macromolecules* **2001,** 34, 4993-4998.
41. Kwok, D. Y.; Neumann, A. W. *Colloids Surfaces A: Physicochem. Eng. Aspects* **1999,** 161, (1), 31-48.
42. Sirard, S. M.; Gupta, P. R.; Russell, T. P.; Watkins, J. J.; Green, P. F.; Johnson, K. P. *Macromolecules* **2003,** 36, 3365-3373.
43. Huang, F. H.; Li, M. H.; Lee, L. L.; Starling, K. E.; Chung, F. T. H. *J. Chem. Eng. Jpn.* **1985,** 18, 490-496.
44. Russell, T. P. *Mater. Sci. Rep.* **1990,** 5, (4), 171-271.
45. Fleming, G. K.; Koros, W. J. *Macromolecules* **1986,** 19, 2285-2291.
46. O'Neill, M. L.; Cao, Q.; Fang, R.; Johnston, K. P.; Wilkinson, S. P.; Smith, C. D.; Kerschner, J. L.; S. H. Jureller. *Ind. Eng. Chem. Res.* **1998,** 37, 3067-3079.
47. Goel, S. K.; Beckman, E. J. *J. Polym. Eng. Sci.* **1994,** 34, 1148.
48. Goel, S. K.; Beckman, E. J. *J. Polym. Eng. Sci.* **1994,** 34, 1137.

49. Gin, P.; Asad, M.; Endo, M. K.; Gedelian, C.; Lu, T.-M.; Koga, T. *Appl. Phys. Lett.* **2009,** 94, 121908.
50. Siripurapu, S.; DeSimone, J. M.; Khan, S. A.; Spontak, R. J. *Macromolecules* **2005,** 38, 2271-2280.
51. Yamaguchi, H.; Gin, P.; Arita, H.; Kobayashi, M.; Bennett, S.; Satija, S. K.; Asada, M.; Koga, T.; Takahara, A. *RSC Adv.* **2013,** 3, 4778-4785.
52. Seeck, O. H.; Kaendler, I. D.; Tolan, M.; Shin, K.; Rafailovich, M. H.; Sokolov, J. C.; Kolb, R. *Appl. Phys. Lett.* **2000,** 76, 2713.
53. Koga, T.; Seo, Y. S.; Jerome, J.; Ge, S.; Rafailovich, M. H.; Sokolov, J. C.; Chu, B.; Seeck, O. H.; Tolan, M.; Kolb, R. *Appl. Phys. Lett.* **2003,** 83, 4309.
54. Li, X. X.; Vogt, B. D. *J. Supercrit. Fluids* **2009,** 51, 256-263.
55. Nishikawa, K.; Tanaka, I.; Amemiya, Y. *J. Phys. Chem.* **1996,** 100, 418-421.
56. Reiter, G.; Sommer, J. U. *Phys. Rev. Lett.* **1998,** 80, 3771.
57. Sommer, J. U.; Reiter, G. *J. Chem. Phys.* **2000,** 112, 4384.
58. Desper, C. R.; Stein, R. S. *J. Appl. Phys.* **1966,** 37, 3990.
59. Massa, M. V.; Dalnoki-Veress, K.; Forrest, J. A. *Eur. Phys. J. E* **2003,** 11, 191–198.
60. Schonherr, H.; Frank, C. W. *Macromolecules* **2003,** 36, (1199-1208).
61. Keddie, J. L.; Jones, R. A. L.; Cory, R. A. *Europhys. Lett.* **1994,** 27, 59-64.
62. Forrest, J. A. *Eur. Phys. J. E* **2002,** 8, 261-266.
63. Koga, T.; Jiang, N.; Gin, P.; Endoh, M. K.; Narayanan, S.; Lurio, L. B.; Sinha, S. K. *Phys. Rev. Letts.* **2011,** 107, 225901.
64. Reither, G., Visualizing properties of polymers at interfaces. In *Soft Matter Characterization*, Borsali, R.; R.Pecora, Eds. Springer: NY, 2007; pp 1244-1292.
65. Reiter, G. *Phys. Rev. Letts.* **1992,** 68, (1), 75-78.
66. Reiter, G. *Langmuir* **1993,** 9, 1344-1351.
67. Sharma, A.; Reiter, G. *LJ. Collid & Int. Sci.* **1996,** 178, 383-399.
68. Okerberg, B. C.; Berry, B. C.; Garvey, T. R.; Douglas, J. F.; Karim, A.; Soles, C. L. *Soft Matter* **2009,** 5, 562-567.
69. Redon, C.; Brochardwyart, F.; Rondelez, F. *Physical Review Letters* **1991,** 66, (6), 715-718.
70. Reiter, G.; Auroy, P.; Auvray, L. *Macromolecules* **1996,** 29, (6), 2150-2157.
71. Jacobs, K.; Seemann, R.; Schatz, G.; Herminghaus, S. *Langmuir* **1998,** 14, (18), 4961-4963.
72. Reiter, G.; Khanna, R. *Langmuir* **2000,** 16, (15), 6351-6357.
73. Durning, C. J.; O'Shaughnessy, B.; Sawhney, U. *Macromolecules* **1999,** 32, 6772-6781.
74. Napolitano, S.; Wübbenhorst, M. *J. Phys. Chem. B* **2007,** 111, 9197-9199.
75. Napolitano, S.; Lupascu, V.; Wubbenhorst, M. *Macromolecules* **2008,** 41, 1061-1063.
76. Fujii, Y.; Yang, Z. H.; Leach, J.; Atarashi, H.; Tanaka, K.; Tsui, O. K. C. *Macromolecules* **2009,** 42, 7418.
77. Napolitano, S.; Pilleri, A.; Rolla, P.; Wübbenhorst, M. *ACS Nano* **2010,** 4, (2), 841-848.
78. Napolitano, S.; Wübbenhorst, M. *Nature Communications* **2011,** 2, 260.

79. Gin, P.; Jiang, N.; Liang, C.; Taniguchi, T.; Akgun, B.; Satija, S. K.; Endoh, M. K.; Koga, T. *Phys. Rev. Letts.* **2012,** 109, 265501.
80. Guiselin, O. *Europhys. Lett.* **1992,** 17, 225-230.
81. Jia, X. Q.; McCarthy, T. J. *Langmuir* **2002,** 18, 683-687.
82. Wallace, W. E.; Zanten, J. H. c.; Wu, W. L. *Phys. Rev. E* **1995,** 52, R3329.
83. Zanten, J. H. v.; Wallace, E. E.; Wu, W. L. *Phys. Rev. E* **1996,** 53, R2053.
84. Paeng, K.; Richert, R.; Ediger, M. D. *Soft Matte* **2012,** 8, 819-826.
85. Ma, Y.; Hu, W.; Reiter, G. *Macromolecules* **2006,** 39, 5159-5164.
86. Zhang, F.; Baralia, G. G.; Nysten, B.; Jonas, A. M. *Macromolecules* **2011,** 44, 7752-7757.
87. Xu, J. J.; Ma, Y.; Hu, W. B.; Rehahn, M.; Reiter, G. *Nat. Mater.* **2009,** 8, 348-353.

Chapter 5 Summary and Future Work

5-1. Summary of Thesis

In the final part of my doctorial thesis I summarize the three research objectives for the overall goal and what I found in each research. The overall goal of my thesis is to develop a $scCO_2$-based green processing for effectively manipulating surfaces/interfaces, i.e. the air/polymer interface and the polymer/substrate interface, utilizing the highly compressible density fluctuating $scCO_2$. The density fluctuation, which is a counterbalance between intermolecular interaction and thermal mobility, is one of unique features of SCFs. In general CO_2 interacts poorly with the most of polymers at $T < 100$ ºC and $P < 50$ MPa, it is however reported that the polymer thin films present the anomalous excess swelling, depending on the elasticity of chains.

The unique features in the combination of polymer thin films and density fluctuating $scCO_2$ focused in this thesis are again as follows: i) Linear dilation (S_f) of polymer thin films, which occurs regardless of a choice of polymers, shows a strong dependence on the magnitude of the density fluctuations of $scCO_2$. ii) At the ridge that is the locus of maxima of density fluctuations of CO_2 at each isothermal condition, the excess swelling ratio is much more increased than the bulk swelling ratios of about 0.1. iii) The excess penetration of CO_2 molecules into polymers occurs within several tens of nanometers from the topmost polymer/$scCO_2$ interface, resulting in a concentration gradient of CO_2, while the excess adsorption of CO_2 molecules is also reported at the polymer/substrate interface. iv) Vitrification of glassy polymers via rapid pressure quench to atmospheric pressure allows one to preserve the swollen structures of polymer thin films in $scCO_2$. Since the excess penetration of $scCO_2$ takes place only at the topmost surface of polymers with tens of nm length scale, it was suggested that this unique phenomenon can be effectively used for modification of surfaces/interfaces of polymer thin films as an environmentally friendly nanoprocessing. In my doctorial thesis the following three objectives were therefore addressed to achieve the overall goal:

1. Development of a new route for manipulating the nanoparticle dispersions within polymer thin films.
2. Better understanding of the interplay between the free surface and substrate interface to create heterogeneous crystalline structures within polymer thin films.
3. Investigation of the mechanism of the $scCO_2$-assisted melt crystallization and the role of the substrate-bound adsorbed polymer layer.

In Chapter 2, I summarized the experimental results to present that the successful development of a new route for manipulating the nanoparticle dispersions within polymer thin films. In particular, the novel route for switching the phase transition was established; the surface segregated/nano-aggregation state of the nanoparticles and the uniform dispersion of the

nanoparticles. The shown phenomena can be widely applied for varieties of polymer/nanoparticle systems. Interestingly, there is a critical thickness (about $4R_g$ thick) for the phase behavior below which the uniform dispersion of the nanoparticles is favorable instead. The keys for the switching are the concentration gradient of the fluid molecules at the polymer/CO_2 interface and the density fluctuations of CO_2 which induce both the polymer chain extension and the critical wetting of CO_2 to the nanoparticles. The CO_2-coated nanoparticles are preferentially migrated to surface through the concentration gradient as the driving force, as predicted in a previous simulation study. A delicate counterbalance among three relevant surface tensions (polymer/CO_2, polymer/nano-aggregates, and nano-aggregates/CO_2) plays a crucial role in controlling the shapes and thermodynamic stability of the surface segregated structures in scCO_2.

In Chapter 3, the as-spun linear low density polyethylene (LLDPE) thin films on Si were subject to characterize as a mode system, in order to investigate the heterogeneous structures of semi-crystalline polymer thin films normal to film surface and understand the interplay between air/polymer surface and polymer/substrate interface. The melting behavior of the films was successfully observed by the *in-situ* x-ray scattering techniques with two incident x-ray angles, so that the structures at surface are separated from ones in film interior. I also evaluated the substrate-bound adsorbed polymer layer, which does not dissolve even in a good solvent, to explain the structures in the interior of the 25 nm thick film.

The findings obtained by the comprehensive analyses using AFM, GISAXS and GID techniques were summarized below; i) The degree of the crystallinity for the 25 nm thick film is almost half of those for the 50 and 100 nm thick films, although the melting behavior was followed by the sequential melting process as well as the 50 and 100 nm thick films. ii) It was indicated the presence of the substrate-bound edge-on lamellar layer which persists at least up to T = 150 °C $>> T_m$ (= 117 °C), regardless of the film thickness. iii) Repeated washing of the films with toluene (good solvent for LLDPE) revealed the presence of the very thin (about 10 nm in thickness) residual edge-on lamellar layer, which is likely the origin of the substrate-bound lamellar layer. iv) The loss of the long periods at the topmost surface of the 25 nm thick film at $T << T_m$.

The heterogeneous structures normal to film surface in the 25 nm thick film can be rationalized as a consequence of the nucleation initiated from the substrate-bound lamellar surface, while the crystallization from both the interfaces (the substrate-bound lamellar surface and the air/polymer surface) compete in the 50 and 100 nm thick films. It is suggested that the influence on the substrate-bound lamellar layer and the subsequent transition zone on the interior structure is within 50 nm in thickness from the substrate interface. Note that the LLDPE/Si in the study is categorized to a weakly attractive interacting system. Since the formation of both the adsorbed layer and the transition zone near the substrate interface would occur irrespective of polymer/substrate interactions, the heterogeneous structures discovered in the present study would be likely general in semi-crystalline polymer thin films.

In the final part of my doctorial thesis, the mechanism of the $scCO_2$-assisted melt crystallization associated with the substrate-bound adsorbed polymer layer has been investigated. I applied the $scCO_2$ treatment to poly (ethylene oxide) thin films, as a model case, since the melting/crystallization behavior in CO_2 has been well characterized in both bulk and thin film. It is known that sorption of CO_2 molecules into a polymer plays a role as a diluent or plasticizer for many glassy/semi-crystalline polymers, lowering the glass transition temperature and melting temperature significantly and hence enhancing the chain mobility within the entire film. At the same time, my experimental results revealed the induced formation of an irreversibly substrate-bound adsorbed layer onto the Si substrate during the $scCO_2$ annealing, due to limited plasticization effect at the polymer/substrate interface. It was thus anticipated that the scO_2 annealing illuminates the effects of the adsorbed layer on the crystallization and dewetting processed under nanoconfined geometries.

The PEO thin films once melted at lower T than the bulk T_m in $scCO_2$ were subsequently quenched to atmospheric pressure. The films were transferred to the temperature-controlled chamber and the melt crystallization from the non-equilibrium amorphous/CO_2 melt was initiated at a given crystallization temperature (T_{cr}). By the combination of the GID and AFM analyses, it was revealed that the all the CO_2 treated films show the flat-on lamellar structures regardless of the thickness and T_{cr}. This contrasts the experimental results from the PEO thin films crystallized via the conventional thermal annealing process where the edge-on lamellar orientation occurs at the film surface. It also was found that the dewetting kinetics is severely hindered for the 20 nm thick CO_2 treated films compared to that for the 50 nm and 100 nm-thick CO_2 treated films. I therefore propose that the "bound" lamellar layer, which does not melt in CO_2, initiates the melt crystallization from the non-equilibrium melting state as seeds during the subsequent annealing process. In addition, the limited plasticization effect does not improve the inherent hindrance of the mobility of the adsorbed chains either, resulting in the persistence of the long-range perturbations associated with the adsorbed layer into the film interior through chain entanglements. The research thus demonstrates that the $scCO_2$-assisted melt crystallization can be used as a low-temperature, environmentally green, and more effective process to produce controlled crystalline morphologies with long-range-order in place of conventional high-temperature thermal annealing.

In summary, I showed that the density-fluctuating $scCO_2$ can be successfully utilized to develop a $scCO_2$-based green processing for effectively manipulating surfaces/interfaces, i.e. the air/polymer interface and the polymer/substrate substrate interface, which is the overall goal in my doctorial thesis. The $scCO_2$ annealing can switch a dispersion state of embedded nanoparticles in a polymer matrix. The $scCO_2$-assisted melt crystallization enables one to achieve precisely controlled morphologies of semi-crystalline polymer thin films, by altering the surfaces/interfaces. I therefore propose that the use of the density fluctuating $scCO_2$ can be one of candidates for a novel polymer processing. Since there still remain unanswered questions, such as the adsorbed polymer layer, the continuous future work deserves for understanding polymer science and applications in industry.

5-2. Future Work

Finally, I would like to mention the related matters which deserve future work. In this thesis I attempted to modify surfaces and/or interfaces of polymer materials with the aid of the plasticization effect by highly compressible CO_2. The high plasticization effect originates from the anomalous excess swelling of polymer thin films in $scCO_2$ at the density fluctuation ridge condition. It is deduced that the local solvent density around the polymer is enhanced/reduced depending on the polymer-fluid interactions and the polymer chain in such solvation structures is expanded, accordingly, to minimize the total free energy of the entire SCF/polymer system. The anomalous expansion of polymer chain would cause additional large solvent-density fluctuations around the chain. However, the considered picture of the perturbed local solvent density fluctuation upon the solvation to polymer chains is experimentally not evident. Furthermore, the deviations of the coherent length of the density fluctuation and its dynamic aspect such as lifetime from the neat SCF are unsolved issues. Since the anomalous excess absorption of SCFs into polymer has a large potential for applications in the polymer industry, the detailed view of the phenomenon should be clarified. For this challenging goal the versatile researches using x-ray/neutron scattering experiments, mass spectroscopy and simulation techniques are necessary.

In this thesis the comprehensive structure analyses for the semi-crystalline polymer thin films have been conducted to understand the crystallization mechanism and the resultant heterogeneous morphologies of the thin films. In particular the substrate-bound adsorbed polymer layer was highlighted and the vital role of the adsorbed layer was presented. I proposed the heterogeneous crystal growth from the surface of the adsorbed polymer layer, and the observed heterogeneities in structures normal to film surface were partially explained. However, it still remains a lot of unsolved tasks; i) What is the minimum lamellar thickness in the adsorbed layer which can thermodynamically and/or kinetically form?; ii) How much the T_m confinement influences the crystallization behavior in addition to the T_g confinement; iii) Not only the nanoconfinement normal to film surface but also the lateral confinement should be taken into account for better understanding crystalline structures; iv) What are the other factors which affect the formation of the adsorbed polymer layer and the related crystallization behavior? At the present study only the T_g confinement (i.e. T_g at surface and interface is lower and higher, respectively) was considered to explain the structures normal to film surface, it is however speculated that T_m also change crystallization rate both at surface and polymer/substrate interface. Therefore a quantitative view for a crystallization model is needed, considering both the T_g and T_m confinement in the direction normal to film surface. In addition, ideas of the crystalline structures which grow laterally in the two dimensionally confined space have to be combined with the present insights. Because I observed the enhanced crystallinity of PEO which was exposed $scCO_2$, the lateral effect on the crystallization is a key to understand the observed deviations. This matter may be crucial for determining the crystal orientation in thin films, as well as film normal direction. I also would like to point out that there are a couple of factors which should be systematically studied, as well as the polymer-substrate interaction. Effects of a molecular length, a distribution, a chain stiffness of a

polymer is worth being clarified. For these objectives to conduct a precise *in situ* observation of melt crystallization of polymer thin film, using the x-ray scattering techniques combined with the hand-made temperature controlled apparatus, is one of feasible approaches in order to obtain a direct evidence of the proposed pictures and answer the above mentioned questions.

I believe that the continuous related researches are very important in polymer science and able to contribute to a progress in polymer industry.

List of Publications

Papers

Chapter 2:

M. Asada, P. Gin, M. K. Endoh, S. Satija, T. Taniguchi and T. Koga, Directed Self-assembly of Nanoparticles at the Polymer Surface by Highly Compressible Supercritical Carbon Dioxide, Soft Matter, 7, 9231-9238, 2011.

M. Asada, P. Gin, M. K. Endoh, S. K. Satija and T. Koga, Surface Segregation of Nanoparticles Driven by Supercritical Carbon Dioxide, Jornal of Physics Conference Series, 272 (1), 012013, 2011.

Chapter 3:

M. Asada, N. Jiang, L. Sendogdular, P. Gin, Y. Wang, M. K. Endoh, T. Koga, M. Fukuto, D. Schultz, M. Lee, X. Li, J. Wang, M. Kikuchi and A. Takahara, Heterogeneous Lamellar Structures Near the Polymer/Substrate Interface, Macromolecules, 45 (17), 7098-7106, 2012.

Chapter 4:

M. Asada, N. Jiang, L. Sendogdular, J. Sokolov, M. K. Endoh, T. Koga, M. Fukuto, L. Yang, B. Akgun, M. Dimitrioug and S. Satija, Melt crystallization/dewetting of ultrathin PEO films via carbon dioxide annealing: The effects of polymer adsorbed layers, Soft Matter, Advance Article DOI: 10.1039/C4SM00683F.

Other Related Papers

Y. Umebayashi, B. Mroz, **M. Asada**, K. Fujii, K. Matsumoto, Y. Mune, M. Probst and S. Ishiguro, Conformation of solvent *N*,*N*-dimethylpropionamide in the coordination sphere of the zinc(II) ion studied by Raman spectroscopy and DFT calculations, The Journal of Physical Chemistry A, 109 (21), 4862-4868, 2005.

Y. Umebayashi, T. Fujimori, T. Sukizaki, **M. Asada**, K. Fujii, R. Kanzaki and S. Ishiguro, Evidence of conformational equilibrium of 1-ethyl-3-methylimidazolium in its ionic liquid salts: Raman spectroscopic study and quantum chemical calculations, The Journal of Physical Chemistry A, 109 (40), 8976-8982, 2005.

R. Kanzaki, Y. Umebayashi, **M. Asada**, S. Ishiguro, T. Matsumoto and A. Wakisaka, Binuclear μ-Perchlorato Complexes of Alkaline Earth Metal Ions Studied by Electrospray Ionization Mass Spectrometry and DFT Calculations, Chemistry Letters, 35 (10), 1118-1119, 2006.

M. Asada, T. Fujimori, K. Fujii, R. Kanzaki, Y. Umebayashi and S. Ishiguro, Solvation structure of magnesium, zinc, and alkaline earth metal ions in *N*,*N*-dimethylformamide, *N*,*N*-dimethylacetamide, and their mixtures studied by means of Raman spectroscopy and DFT calculations-Ionic size and electronic effects on steric congestion, Journal of Raman Spectroscopy, 38 (4), 417-426, 2006.

M. Asada, T. Mitsugi, K. Fujii, R. Kanzaki, Y. Umebayashi and S. Ishiguro, Vibrational spectroscopy and molecular orbital calculations of *N*,*N*-dimethylacrylamide and *N*,*N*-dimethylpropionamide - Conformational equilibrium in the liquid state -, Journal of Molecular Liquids, 136 (1-2), 138-146, 2007.

M. Asada, T. Mitsugi, T. Ogura, K. Fujii, Y. Umebayashi and S. Ishiguro, Solvation number and conformation of *N*,*N*-dimethylacrylamide and *N*,*N*-dimethylpropionamide in the coordination sphere of the cobalt(II) ion in solution studied by FT-IR and FT-Raman spectroscopy, Analytical Sciences, 23 (7), 835-840, 2007.

P. Gin, **M. Asada**, M. K. Endoh, C. Gedelian, T.-M. Lu and T. Koga, Introduction of molecular scale porosity into semicrystalline polymer thin films using supercritical carbon dioxide, Applied Physics Letters, 94, 121908, 2009.

H. Kishi, Y. Kunimitsu, J. Imade, S. Oshita, Y. Morishita and **M. Asada**, Nano-phase structures and mechanical properties of epoxy/acryl triblock copolymer alloys, Polymer, 52 (3), 760-768, 2011.

T. Koga, P. Gin, H. Yamaguchi, M. K. Endoh, **M. Asada**, L. Sendogdular, M. Kobayashi, A. Takahara, B. Akgun, S. K. Satija and T. Sumi, Generality of anomalous expansion of polymer chains in supercritical fluids, Polymer, 52 (19), 4331-4336, 2011.

H. Yamaguchi, P. Gin, H. Arita, M. Kobayashi, S. Bennett, S. K. Satija, **M. Asada**, T. Koga and A. Takahara, Effect of supercritical carbon dioxide on molecular aggregation states of side chains of semicrystalline poly{2-(perfluorooctyl) ethyl acrylate} brush thin films, RSC Advances, 3, 4778-4785, 2013.

Acknowledgements

This doctorial thesis contains the studies which I have carried out from 2008 to 2009 at Department of Materials Science and Engineering of Stony Brook University (New York, USA) under the direction of Associate Professor Tadanori Koga.

I would like to express my deepest appreciation to Associate Professor Tadanori Koga and Professor Atsushi Takahara for their continuous guidance and encouragement throughout the course of my work. I also would like to express my gratitude to Dr. Maya K. Endoh, Dr. Peter Gin and Mr. Naisheng Jiang for their helpful and convincing support. I am deeply grateful to Professor Jonathan Sokolov and Associate Professor Takashi Taniguchi for technical support and useful suggestions.

I express my gratitude to my colleagues in Kuraray, Dr. Yukiatsu Komiya, Mr. Katsunori Takamoto, Mr. Naoki Fujiwara, Mr. Takahiro Ishii, Mr. Shigeru Sasaki and Mr. Tetsuya Hara for their continuous encouragement and helpful support.

I acknowledge the financial support from Kuraray Co., Ltd. and the NSF Grant no. CMMI-0846267. I also thank the Garcia Center at Stony Brook University for the AFM experiments, Dr. Dongcui Li and the Bio-Imaging Center at the Delaware Biotechnology Institute for partial AFM experiments, Mr. Steve Bennett for the x-ray reflectivity experiments, Dr. Masafumi Fukuto for the use of National Synchrotron Light Source (contract no. DE-AC02-98CH10886 and DEAC02- 98CH10886), Dr. Sushil Satija and Dr. Bulent Akgun for the neutron reflectivity measurements, the Advanced Photon Source and the BL03XU frontier soft-material beamline in SPring-8 with the proposal No. 2011B7256 and No. 2013A7206 for the x-ray scattering measurements.

July, 2014

Mitsunori Asada